

# **Improving Ceramic Additive Manufacturing via Machine Learning-Enabled Closed-Loop Control**

**By  
Zhaolong Zhang**

A Dissertation  
Submitted to the Faculty  
of the  
WORCESTER POLYTECHNIC INSTITUTE  
in Partial Fulfillment of the Requirements for the  
Degree of Doctor of Philosophy

in  
Manufacturing Engineering  
by

---

December 2020

APPROVED:

---

Dr. Jianyu Liang

---

Dr. Walter Thomas Towner

---

Dr. Christopher A. Brown

---

Dr. Mingjiang Tao  
Civil Engineering  
External Committee Member

---

Dr. Richard D. Sisson

## **1. Abstract**

Advanced ceramics are widely used in aerospace, automotive, electronic, laboratory equipment, and other industries. To achieve the geometric complexity and desirable properties that are difficult to obtain by conventional manufacturing methods, ceramic additive manufacturing (AM) methods have been studied intensively in recent years. However, in-process control with feedback is not currently implemented in any commercially available ceramic three-dimensional (3D) printer. Robocasting is one of the most widely utilized AM processes for various ceramic materials at a low cost. This study employed robocasting as an example of implementing an in-process control with a feedback loop in a ceramic AM process. In this research, the material parameters, process parameters, machine parameters, and their influences on quality parameters were investigated. The key parameters of the ceramic robocasting process were identified. The relationships among the functional requirements, design parameters, and process variables in the robocasting process were analyzed using Axiomatic Design (AD) theory. A database of the relationships among pressure, extrusion, and the quality of the printed green part was established. An artificial neural network (ANN) model was created based on the established database. Machine learning-enabled closed-loop control was integrated into the current robocasting process to improve the quality of the printed green parts. Finally, the improvement was validated by comparing the quality of the prints in both controlled operations and uncontrolled operations.

## **2. Acknowledgments**

First and foremost, I would like to express my sincere gratitude to my advisors, Prof. Richard Sisson and Prof. Jianyu Liang, for their encouragement and guidance. Their outstanding and kind support made this dissertation possible. I would also like to thank Prof. Yiming Rong, who brought me to WPI and accepted me as a Ph.D. student first. Without him, there would have been no way for me to start my Ph.D. work and research career. I would also like to express my gratitude to the committee members, Prof. Brown, Prof. Towner, and Prof. Tao. Their suggestions, feedback, assessments, and insights were so important and became part of the cornerstone of this dissertation.

I would also like to express my thanks to all crew members of the manufacturing laboratory. Toby, Ian, and James, thank you so much for your help and support. I have learned so many things from you about not only hands-on manufacturing skills but also American lifestyles. Rita, GloreAnn, Shelly and Maureen, thank you so much for your support during my study in the Manufacturing Engineering Program. With your help, everything became so smooth and well organized.

Whenever I encountered difficulties, my colleagues and friends were always so nice and supportive. I can never forget the stimulating discussions I had with my colleagues in the Nanomaterials & Nanomanufacturing Laboratory. I would also like to express my appreciation for Zhaotong, Yutao and all of the people who helped me with my research, laboratory activities, and academic works.

I am thankful for my parents, parents-in-law, and other family members for their priceless words of motivation and encouragement. No words can express the gratitude I feel in my heart for them. Most importantly, I would like to thank my wife, Yarong. Without her support and love, it would have been impossible for me to have finished my Ph.D.. I am grateful for our cats, North and South, for their naughty behavior, which is often troublesome but bring tons of happiness and joy to my life.

## Contents

1.	Abstract .....	2
2.	Acknowledgments .....	3
3.	Introduction .....	9
3.1	Motivation .....	9
4	Literature Review .....	15
4.1	Ceramic Additive Manufacturing Methods: Mechanical and Control Systems.....	15
4.1.1	Selective Deposition Methods.....	15
4.1.2	Selective Binding Methods .....	16
4.2	Ceramic Robocasting .....	21
4.3	Axiomatic Design Theory .....	24
4.4	Control System Engineering and Control Systems in Ceramic Additive Manufacturing . .....	28
4.4.1	Proportional–Integral–Derivative Controller .....	29
4.4.2	Artificial Neural Network .....	31
5	Methodology .....	35
6	Results .....	37
6.1	Model of the Extruder Unit of Robocasting.....	37
6.2	Model of Design Patterns for This Research.....	39
6.3	Defining the Parameters in Robocasting Technology and Characterizing Their Relationships.....	41
6.4	Material Parameters.....	43
6.4.1	Density of the Slurry .....	43
6.4.2	Viscosity of the Slurry .....	43
6.5	Printer Parameters .....	49
6.6	Process Parameters .....	50
6.6.1	Extrusion Speed and Travel Speed.....	50
6.7	Intermediate Parameters .....	54
6.7.1	Deformation and Deflection of the Printed Part.....	54
6.7.2	Dynamic Model of Extrusion Process.....	56
6.8	Ceramic Robocasting Process Analyzed by the Axiomatic Design Theory.....	58
6.8.1	Current Decomposition .....	58
6.8.2	Relations Among FRs, DPs, and PVs.....	58
6.8.3	Design Matrix.....	62
6.8.4	Coupling .....	62
6.8.4.1	FR-DP Coupling Produced by Material Properties.....	63
6.8.4.2	FR-DP Coupling for Redundant Control of the Different Directions of Print.....	63
6.8.4.3	Discussion on DP-PV Coupling.....	63
6.8.5	Axiom II: Minimize the Information Content of the Design .....	64
6.8.6	Physical Integration.....	64
6.8.7	Discussion .....	65
6.8.8	Concluding Remarks .....	66
6.9	Improving Ceramic Additive Manufacturing by Machine Learning Enabled Closed- Loop Control.....	67
6.9.1	Design of the Control Loop.....	67
6.9.2	Profile of Printed Patterns for the Uncontrolled Group .....	70
6.9.3	Pressure Control by ANN.....	72
6.9.4	Characterization of Printed Patterns.....	78
6.9.4.1	Characterization of the Whole Pattern.....	78
6.9.4.2	Characterization of the Single Model .....	81

6.9.5	Concluding Remarks .....	84
7	Summary .....	85
7.1	Conclusion and Impact.....	85
7.2	Recommendations for Future Works.....	86
8	Publication and Presentations.....	88
8.1	Accepted Journal Publications .....	88
8.2	Conferences .....	88
9	References .....	89
	Appendix A .....	95
	Appendix B.....	96
	Appendix C .....	105
	Appendix D.....	106
	Appendix E .....	110

## List of Tables

Table 1 Accuracies of different ceramic manufacturing technologies. ....	12
Table 2 Slurries with different aluminum oxide and PEO concentrations.....	44
Table 3 Recipe for the slurry used in this study. ....	46
Table 4 Rheological properties of the ceramic slurry: shear rate, measured shear stress, viscosity, and fitted shear stress. ....	47
Table 5 Coefficient for calibrating the extruder. ....	49
Table 6 Average height, width, length, cross-sectional area, and calculated volume of the printed filament.....	52
Table 7 Mean and standard deviation of height difference for different layover times.....	55
Table 8 Current decomposition.....	58
Table 9 Assigned metrics for FR1, DP1, PV1 and their children.....	59
Table 10 Relationship between <i>MExtrude</i> and <i>LE</i> in this study.....	68
Table 11 Example of data collected for training and testing the extruding length prediction ANN model.....	68
Table 12 Statistics of the error distribution of these four activation functions.....	74
Table 13 Statistics of relevant errors for the ANN model.....	75
Table 14 Statistics of the accumulated frequency of relevant error range.....	75
Table 15 Abbreviation name of experiment groups.....	76
Table 16 Statistical results of the sensor histories for variance processes.....	78
Table 17 Statistical results of the profile information for the mean of each model in the uncontrolled 28 mm, 32 mm, and 36 mm groups and controlled REF 5500, RFE 6500, and REF 7000 groups.....	80
Table 18 Statistical results of width information for the 7 <sup>th</sup> model for the uncontrolled 28 mm group, and the typical model in controlled RFE 5500 group, RFE 6500, and RFE 7000 group. ....	83

## List of Figures

Figure 1 Examples of 3D printed products[2-4].	9
Figure 2 Number of research papers on ceramic AM from 1993 to 2020.	10
Figure 3 Ceramic AM market forecast from 2017 to 2028 [6].	10
Figure 4 AM methods.	11
Figure 5 Number of publications between 1970 and 2020 in the ceramic additive manufacturing field.	12
Figure 6 Current robocasting process flow.	13
Figure 7 Novel robocasting process.	14
Figure 8 LOM process [19].	15
Figure 9 View of a cut-off-the stack LOM [20].	16
Figure 10 Mechanism of a SLA printer [20].	17
Figure 11 Illustration of an SLA [22].	17
Figure 12 Mechanism of a selective laser sintering printer [20].	18
Figure 13 Exploded view diagram of the dual piston powder delivery system of a selective laser melting print [30].	19
Figure 14 Mechanism of 3 Dimension printing [12].	19
Figure 15 Process of ceramic laser fusion [33].	20
Figure 16 Products of 3D printing technology [36].	20
Figure 17 Part fabricated by robocasting [35].	21
Figure 18 Cylinder and solid cone fabricated using the Hilmas method [36].	22
Figure 19 Scheithauer et al.'s thermoplastic extrusion method [37].	22
Figure 20 Top-down structure and relationships among domains [59].	24
Figure 21 Block diagrams of control systems: (a) open-loop system and (b) closed-loop system [69].	29
Figure 22 Block diagrams of control systems: (a) open-loop system and (b) closed-loop system [69].	29
Figure 23 Schematic of the artificial neural network.	31
Figure 24 Equation and graphs of commonly used activation functions.	32
Figure 25 Summary of first-order optimization methods [75].	34
Figure 26 Flow diagram of the research plan.	35
Figure 27 Schematic of the ceramic robocasting machine with a customized extruding unit [76].	37
Figure 28 Model of the extruder unit of the robocasting system.	38
Figure 29 Schematic of design pattern #1 for testing the influence of different speed combinations. Units in mm.	39
Figure 30 Schematic of the experiment for testing the height between the upper layer and the lower layer.	40
Figure 31 Schematic of the pattern designed for closed-loop control construction and verification. Units in mm.	40
Figure 32 Relationships among machines, materials, and process parameters with quality parameters.	41
Figure 33 Schematic of the overall approach proposed in the current project to establish the relationships among processes, intermediate values, and quality parameters.	42
Figure 34 Particle diameter distribution.	45
Figure 35 Demonstration of the test process: a) Anton-Paar MCR 302 Rheometer, b) PP-25 test plate, and c) ceramic slurry used in the test.	45
Figure 36. Rheological properties of slurries with different concentrations.	45

Figure 37 Appearance viscosity curve for slurries with 20 % solute volume fraction and 5 % thickening agent weight fraction.....	47
Figure 38 Tested and fitted shear stress–shear rate curve.....	48
Figure 39 Samples printed at different extrusion speeds with a travel speed of 1200 mm/min ..	51
Figure 40 Printed filament measured by noncontact, 3D, surface metrology confocal microscopy.....	52
Figure 41 Schematic for the deflection (z) of the upper layer. ....	55
Figure 42 Sample measured by noncontact, 3D, surface metrology confocal microscopy.....	55
Figure 43 Height difference (um) vs. different layover times (s).....	56
Figure 44 Schematic of the dynamic model of the extrusion process.....	57
Figure 45 FR-DP design matrix.....	62
Figure 46 DP-DP interactions for the current robocasting process.....	65
Figure 47 Flow diagram of ANN closed-control loop.....	67
Figure 48 Profiles for the printed pattern with <i>MExtrude</i> ranging from 1.0 to 1.9.....	70
Figure 49 a) Loadcell reading history for extrusion length of 20 mm, 28 mm, and 36 mm groups and b) 6th model on the extrusion length of 28 mm group.....	71
Figure 50 Summary of the ANN model for extrusion length prediction.....	72
Figure 51 Absolute error (mm) of the training set by using different activation functions: a) ReLU, b) Tanh, c) Sigmoid, and d) Softplus.....	73
Figure 52 Count of error (mm) of the training set and test set: a) test set and b) training set.....	74
Figure 53 Sensor histories of the 6 <sup>th</sup> to 9 <sup>th</sup> models in variance printing condition: a) extrusion length of 20 mm, b) extrusion length of 28 mm, c) extrusion length of 36 mm, d) controlled group with target sensor reading of 5500 g, e) controlled group with target sensor reading of 6500 g, and f) controlled group with target sensor reading of 7000 g.....	76
Figure 54 Profiles for the printed pattern in various conditions. Uncontrolled groups: extrusion 28 mm, extrusion 32 mm, and extrusion 36 mm; controlled groups: RFE 5000, 6500, and 7000.....	78
Figure 55 Example of a printed model to be analyzed. a) Overview of a model in REF 6500 group acquired by the confocal microscope, b) cross-sectional profile of measurement points #1, 4, 5, 8, 9, 12, 13, 16, 17, 20, and 21, and c) detailed profile of measurement points.....	79
Figure 56 Mean profile width statistics for each model printed by various printing conditions.....	80
Figure 57 Statistical width information of the 7th model in uncontrolled printing conditions: a) Statistical width information for the whole model and b) range and distribution of each model.....	81
Figure 58 Overview of the 7th model in the uncontrolled groups acquired by the confocal microscope: a) extrusion length of 28 mm and b) extrusion length of 36 mm.....	82
Figure 59 Information of the 7 <sup>th</sup> model for the uncontrolled 28 mm group, and the typical model in controlled RFE 5500 group, RFE 6500, and RFE 7000 group: a) statistical width information for the whole model, and b) range and distribution of each model.....	83
Figure 60 Block diagrams of closed-loop control systems: a) conventional closed-loop control and b) intelligent process of material [69].....	87



### 3. Introduction

#### 3.1 Motivation

Additive manufacturing (AM) techniques have been applied to fabricate ceramic material. Compared with conventional subtracting processes, AM techniques have the advantage of building finished parts in successive layers [1]. Ceramic AM methods have the flexibility of producing complex geometries, which are hard to replicate using conventional methods. Figure 1 shows several examples of additively manufactured ceramic parts: (a) powder-based artwork model, “The Flower” [2]; (b) freeform-shaped alumina part obtained with indirect selective laser sintering [3]; and (c) lattice structure constructed by robocasting technology [4].

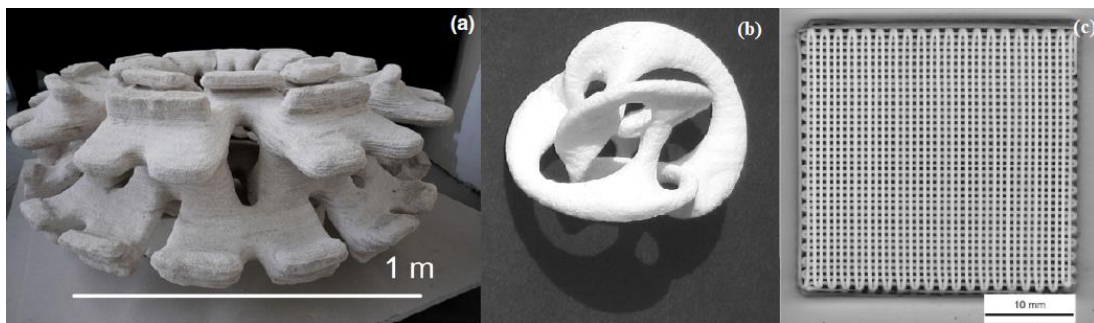


Figure 1 Examples of 3D printed products[2-4].

According to the Web of Science, there has been a notable increase in the number of studies in the ceramic AM field over the past 25 years, as shown in Figure 2. Figure 3 shows the forecasted growth in the ceramic AM market size according to a study by SmarTech Markets [5]. The study predicted that the ceramic AM market would grow to 3,678 million US dollars by the end of 2028, which is approximately 12 times the current ceramic AM market of 268 million US dollars. [6].

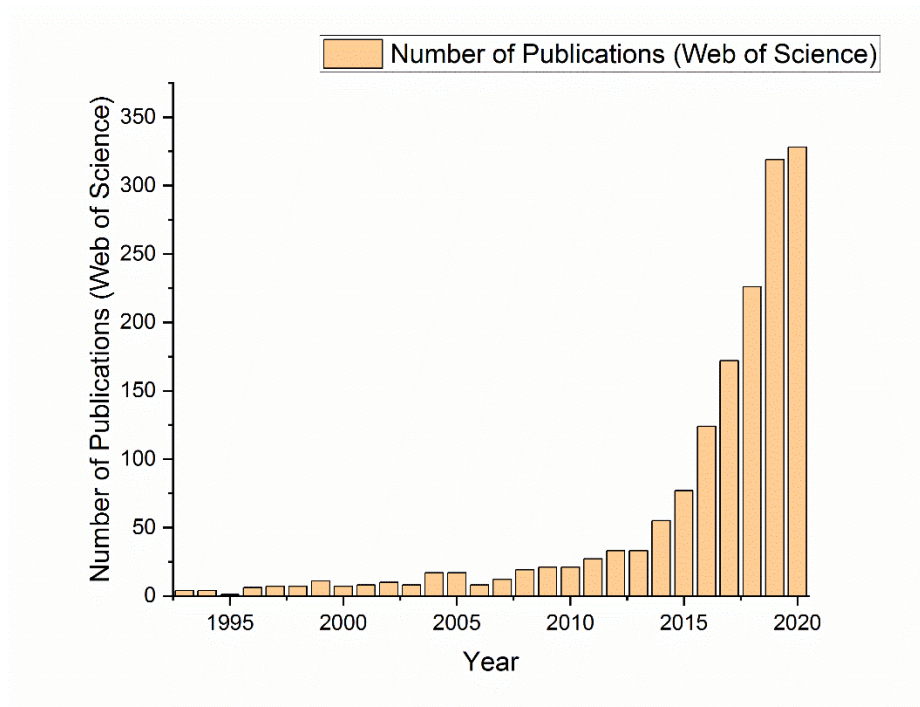


Figure 2 Number of research papers on ceramic AM from 1993 to 2020.

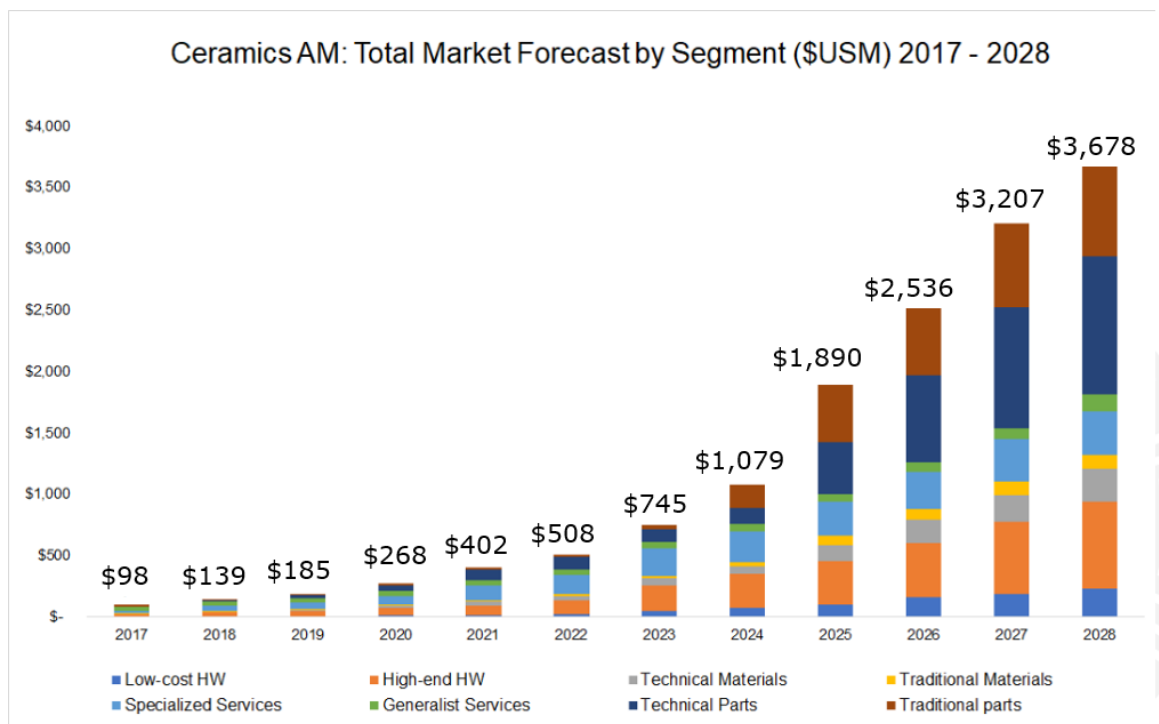


Figure 3 Ceramic AM market forecast from 2017 to 2028 [6].

The ceramic AM methods can be categorized as either selective deposition methods or selective binding methods. Figure 4 summarizes various AM methods for ceramics, including the date of invention.

- **I. Selective deposition printers**
  - Extrusion Free-forming Printer(1987)
    - Robocasting(1987)
    - Multilayer Jet Printing(1994)
    - Freeform Extrusion for Ceramics(1996)
    - Freeze Form Extrusion(2006)
    - Thermoplastic 3D Printing(2014)
  - Laminated Object Manufacturing (LOM) (1986)
    - Laminated Object Manufacturing for Paper and Polymer(1986)
    - Laminate Tape(1995)
    - High Speed Cutting(2009)
- **II. Selective binding printers**
  - Stereo Lithography(SL) (1986)
    - Stereo lithography for Polymer (1986)
    - Freeform Fabrication via Stereo lithography(1996)
  - Selective Laser Sintering (1980)
    - Selective Laser Sintering (Powder Bed, Plastic) (1980)
    - Selective Laser Sintering (Powder Bed, Ceramic) (2000)
    - Airbrush Laser Sintering (Slurry, Ceramic) (2009)
  - 3 Dimension Printing (1995)
    - 3 Dimension Printing(1995)
    - 3DP (DIP) (1995)

Figure 4 AM methods.

Aside from advantages, there remain some limitations of ceramic AM methods. Most of the ceramic AM processes listed in Figure 4 are open-loop systems [7]; thus, in-process errors are not corrected during AM operations. Since AM methods build final products layer by layer, biases produced by each individual layer accumulate and contribute to the inaccuracy of the final product. As a result, accumulated inaccuracies causes a lower dimensional quality of additively manufactured parts than conventional green machined products. Table 1 summarizes the accuracies of different ceramic manufacturing technologies. Conventional green machining processes are comparable to CNC machining processes, which are closed-loop systems[8]. An in-process control/feedback system is needed to improve the dimensional accuracy of the three-dimensional (3D) printed part by achieving accurate control of the processing parameters.

Table 1 Accuracies of different ceramic manufacturing technologies.

Techniques	Selective Laser Melting	Freeform Extrusion	Laminated Object Manufacturing	Green Machining
Accuracy	0.43–40 $\mu\text{m}$ [9, 10]	60 $\mu\text{m}$ [11]	50 $\mu\text{m}$ [12]	12 $\mu\text{m}$ [13]

Robocasting is one of the most widely used additive manufacturing techniques, as it can be applied to various ceramic-based materials at a low cost. As shown in Figure 5, according to the data from the Web of Science, robocasting attracts the most attention among all the techniques identified in Figure 4. The fused filament fabrication, gas metal arc welding-based 3D printing, and robocasting methods share similar mechanics but can be applied to different kinds of materials. Researchers conducted studies to analyze printable materials, investigated the performance of printed products, and improved the drying mechanisms of the ceramic slurry. However, there remain difficulties in improving the geometric accuracies of products that were fabricated by the current robocasting process.

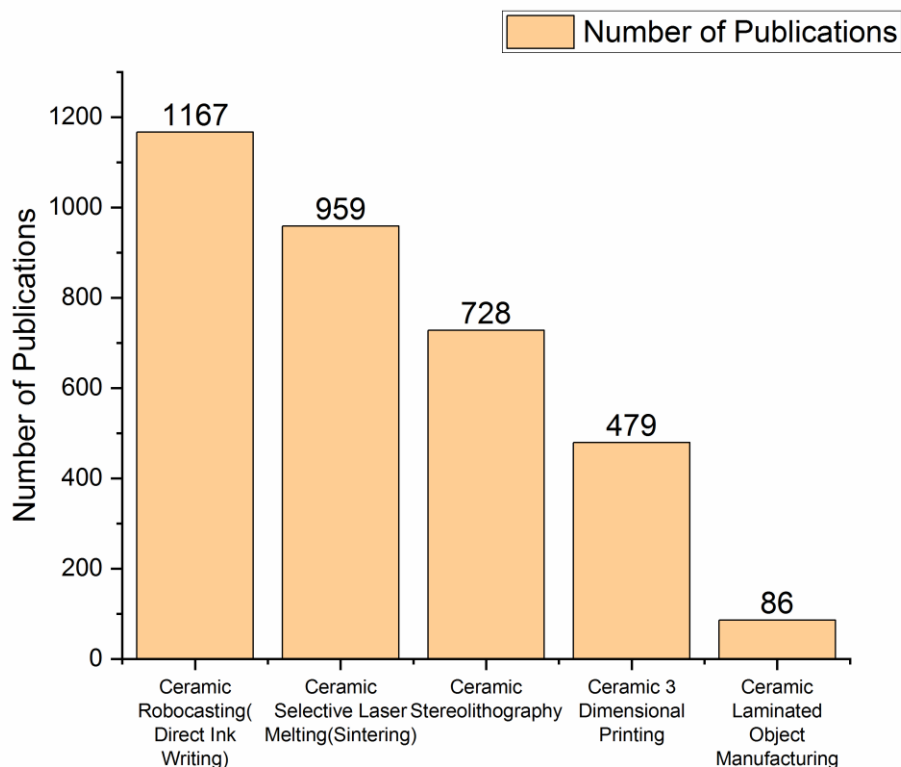


Figure 5 Number of publications between 1970 and 2020 in the ceramic additive manufacturing field.

One of the most significant difficulties is the lack of feedback and desired real-time control

to ensure print quality during the current manufacturing process flow. The current robocasting process flow is an open-loop system that does not have any sensors or feedback, as shown in Figure 6. In the current robocasting process, a designed CAD model is sent to a slicing software, which generates the printing commands in G-code (RS-274) format. Motions, extrusions, temperature control, and tool information are stored inside the G-code and passed to a control unit, such as a programmable logic controller (PLC). G-code is loaded into the memory of the controller. Each line of the G-code is decoded by the interpreter, which builds an internal representation and then changes the internal state or calls for one or more canonical machining functions [14]. The G-code is interpreted in a line-by-line manner. The PLC then accommodates these canonical machining functions via machine settings to control each stepper motor's rotary motions. These rotary motions are converted to linear movements by mechanical components, such as gears or pulleys. In an open-loop system, the process follows a linear pattern: once the G-Code is defined and sent to the printer, any disturbances generated during the process cannot be corrected or compensated. In this research, a modified closed-loop process is shown in Figure 7. A loadcell was integrated into the original system as an example to monitor the in-process status. Instead of generating G-code before the start of the print, the G-code was sorted by path. The G-code for a subsequent path was generated based on the real-time status and control algorithm.

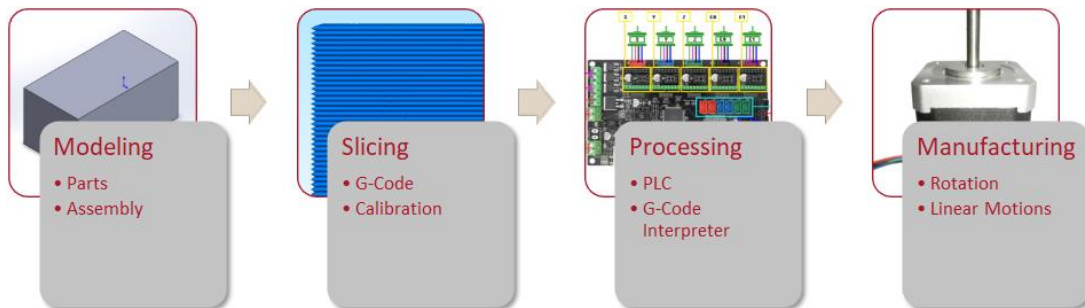


Figure 6 Current robocasting process flow.

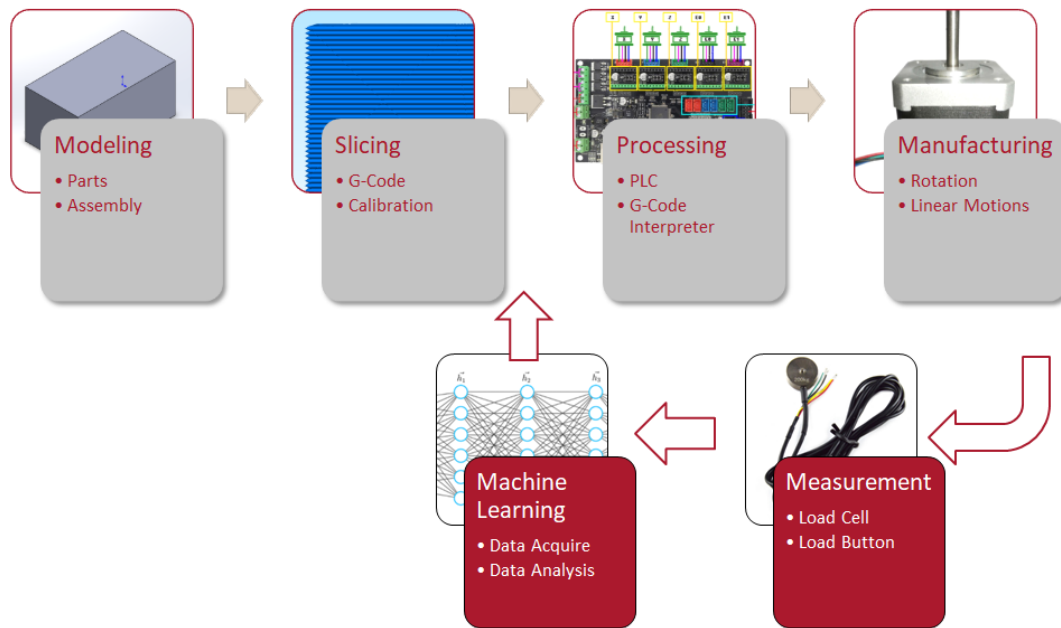


Figure 7 Novel robocasting process.

To implement the feedback loop, the process parameters need to be optimized according to shear-thinning slurry rheology. In conventional process control technology, such as the proportional–integral–derivative (PID) controller, a well-developed accurate dynamic model of the process is the key to realizing feedback control [15]. Since the extrusion process has a complex dynamic model, the transfer function is hard to formulate in the robocasting process. The development of the artificial neural network (ANN), which is a data-driven decision-making approach, provides a chance to by-pass the complex dynamic physics equations and map the real-time status into control actions by experience [16].

This study used robocasting as an example of implementing and validating the need for an in-process control/feedback loop in the ceramic additive manufacturing process. Critical parameters for ceramic robocasting were identified. The relationships among the functional requirements, design parameters, and process variables in the robocasting process were analyzed by the Axiomatic Design (AD) theory. A database of the relationships among these parameters and the quality of the printed part was established. Finally, a closed-loop robocasting process was implemented, and its effectiveness in improving the printing quality was validated experimentally. The approach to integrating the closed-loop control into the robocasting process can be generalized to other printing techniques with similar mechanics.

## 4 Literature Review

### 4.1 Ceramic Additive Manufacturing Methods: Mechanical and Control Systems

#### 4.1.1 Selective Deposition Methods

Selective deposition methods stack materials in the order of either lines or planes, and a heat source or binder is employed during the printing process. Robocasting is one of the selective deposition methods; it is reviewed separately in chapter 4.2. Laminated object manufacturing (LOM) is another selective deposition method. The materials that are utilized in these processes are commonly in filament, sheet, or paste form.

Newman et al. and Mathewson et al. carried out research on the LOM method and concluded that the accuracy of this method was  $50\ \mu\text{m}$  [17, 18]. Figure 8 expresses the fabrication process of the LOM methods, in which raw material is transformed into a thin sheet and then stacked, bound, and cut layer by layer.

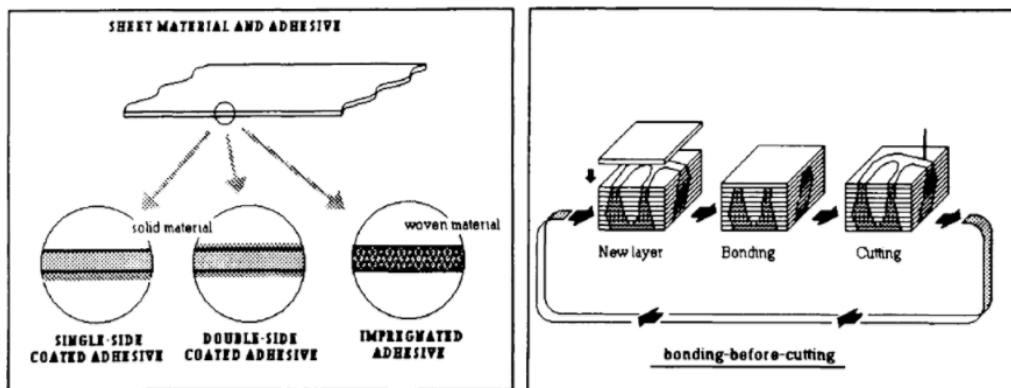


Figure 8 LOM process [19].

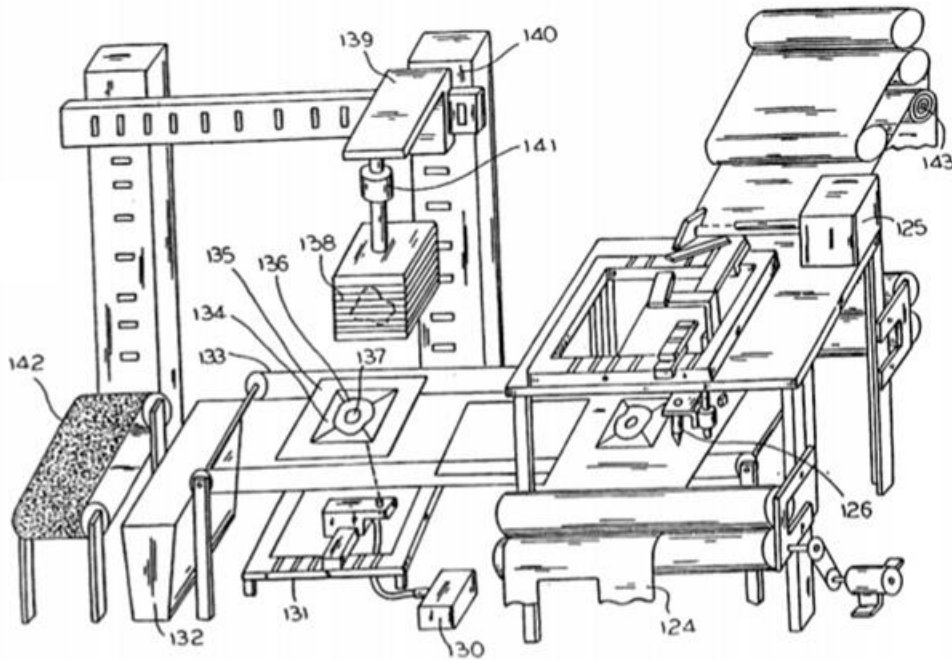


Figure 9 View of a cut-off-the stack LOM [20].

Although the effects of pressure, layers, and dwell time on lamination have been well investigated, almost all of the control systems of the selective deposition printers are still open-loop systems. Feygin et al. discovered that the load signal produced by the load cell is the only feedback in the LOM method [20]. The loadcell is unit 141 in Figure 9. The layer height, dwell time, and deflection were not measured during the process to control the accuracy of the print.

#### 4.1.2 Selective Binding Methods

Selective binding methods usually use a powder bed or a tank of liquefied light-curable polymers without the need for stacking. There is always some type of external energy, such as heat or ultraviolet (UV) light from a laser beam, which is involved in the fabrication process. Stereolithography (SLA), laser sintering, and 3 Dimension printing are examples of selective binding printers.

Figure 10 shows a diagram of a SLA printer. SLA printers consist of a z-level adjustable platform, which can be dipped into a tank of liquid photopolymerizable material with a light source that is movable in the XY plane. The workspace for the SLA method is the contact surface of the liquid and platform. After the bottom surface is cured, the platform moves one step toward the z-positive direction. Paul et al. discovered that 70% of the printed dimension deviations are within the range of  $\pm 5$  mils, which is approximately  $\pm 100 \mu\text{m}$  [21]. The current



control loop of the SLA printer is a linear loop, as shown in Figure 11. There is no feedback control or control signal in the current SLA printers, as noted by Leyden et al. [22].

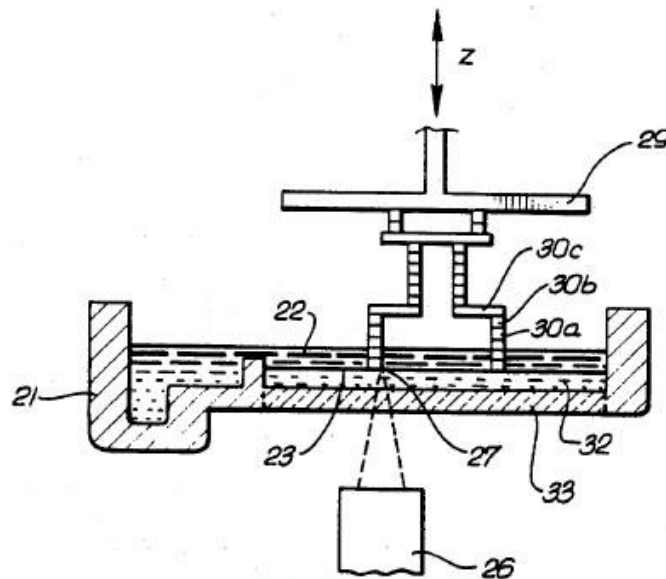


Figure 10 Mechanism of a SLA printer [20].

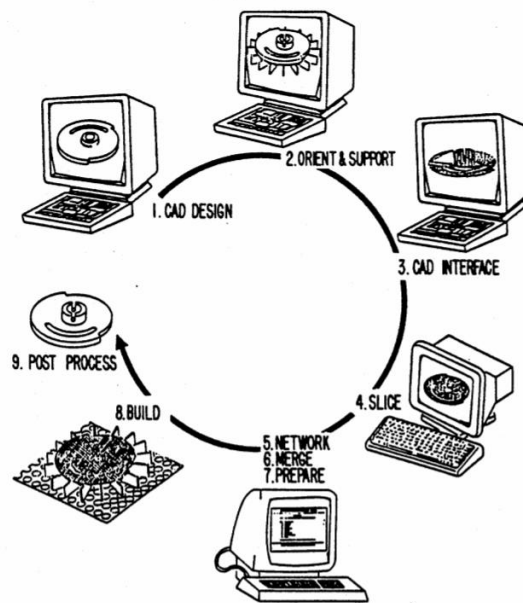


Figure 11 Illustration of an SLA [22].

Figure 12 shows the mechanism of a selective laser sintering printer. During the manufacturing process, external energy, such as the heat from the laser, is applied to powders to melt and join them together [23]. The early approach of selective laser sintering printers

contains two z-level adjustable platforms. One of the platforms is raised in the z-positive direction to provide powders for printing (the vendor), while the other is lowered in the z-negative direction to act as the printing space. A roller is used to transfer powders between the platforms.

There are two kinds of control loops for selective laser sintering printers. The first control loop follows an open-loop path with no feedback control signal. Lakshminarayan et al. successfully sintered alumina powders with a diameter of 44  $\mu\text{m}$  in 1992. The focus of the laser beam diameter was 500  $\mu\text{m}$  [24, 25]. Ullmann et al. used a micro selective laser sintering (micro SLS) process with a fine laser lens that had a focus with a minimum radius of 7  $\mu\text{m}$  to produce alumina-feldspar, alumina-silica, feldspar, and silicon/silicon carbide/carbon (Si-SiC-C) products [5, 26-29]. Maruo et al. discovered that the accuracy of an open-loop selective laser melting ceramic printer was approximately 40  $\mu\text{m}$  [10]. The second control loop contained position feedback [23]. Forderhase et al. suggested several ways to keep track of the printer's linear displacement, such as determining the displacement by referencing the current position compared to its starting position or monitoring the level of the powder using a capacitive or ultrasonic proximity switch. The upward and downward displacement of piston 61, as shown in Figure 13, can be measured relative to the actual surface of the powder [30]. By adopting the feedback control loop into the printer, the accuracy of the print can be considered similar to the resolution of the laser spot, which have a minimum diameter of 0.43  $\mu\text{m}$  [10].

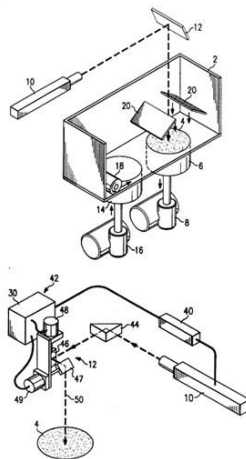


Figure 12 Mechanism of a selective laser sintering printer [20].

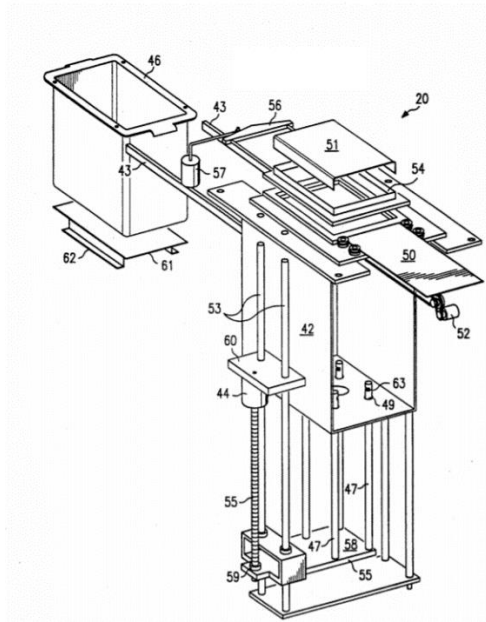


Figure 13 Exploded view diagram of the dual piston powder delivery system of a selective laser melting print [30].

The mechanism of the 3 Dimension printing method is similar to the mechanism of the selective laser sintering method, as shown in Figure 14. It also has two z-level adjustable platforms: one serves as the printing platform, and the other platform stores the powder. A roller is used to transfer the powders between the platforms. The binding mechanism between these two methods is different. The laser sintering method uses heat from a laser beam to melt powders and bind them together, while 3 Dimension printing methods use liquid binders as ink to combine powders into a solid body.

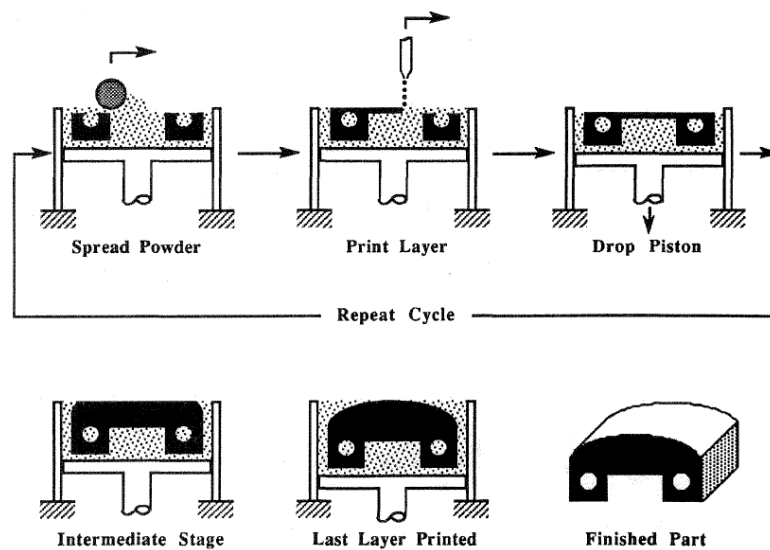


Figure 14 Mechanism of 3 Dimension printing [12].

3 Dimension printing methods have demonstrated high capability in fabricating ceramic material [12, 31-34] and flexibility when combined with other methods. Tang et al. combined the 3 Dimension printing method with SLA technology. They developed a new method, laser fusion, to produce ultrathin layers in 2006 [35]. Figure 15 shows the process of ceramic laser fusion, which is a 3 Dimension printing method. The ceramic powder in the conventional 3 Dimension printing method was replaced by a slurry, which contains ceramic powder and light-curable resin. The designed shape was cured by exposing the slurry under UV light.

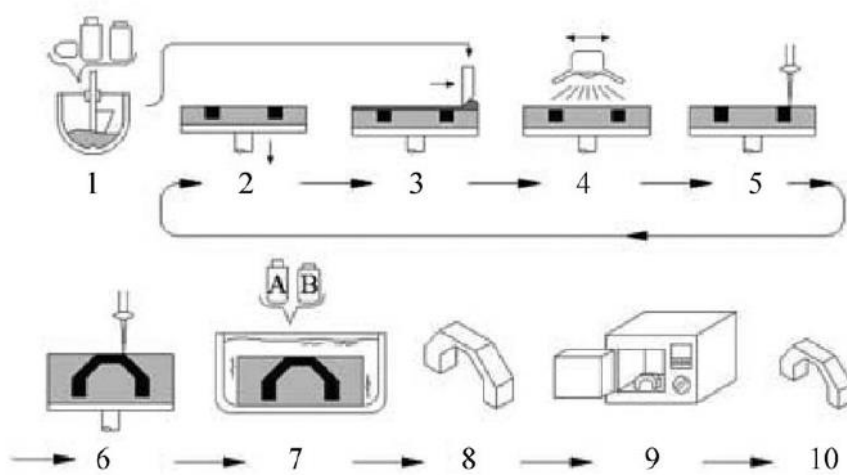


Figure 15 Process of ceramic laser fusion [33].

Figure 16 shows that it is difficult for 3 Dimension printing methods to produce complex geometries; extra material was observed on the fabricated parts. Figure 16 shows some turbines, with a 400  $\mu\text{m}$  blade, that are produced by different inkjet 3D printers: a) Solidscape T76, with an in-plane resolution of 5  $\mu\text{m}$  and a layer thickness of 12.7  $\mu\text{m}$ ; b) 3D System ProJet HD 3000 plus, with an in-plane resolution of 34  $\mu\text{m}$  and a layer thickness of 16  $\mu\text{m}$ ; and c) Objet Eden 260 V 3D printer, with an in-plane resolution of 42  $\mu\text{m}$  and a layer thickness of 16  $\mu\text{m}$  [37].

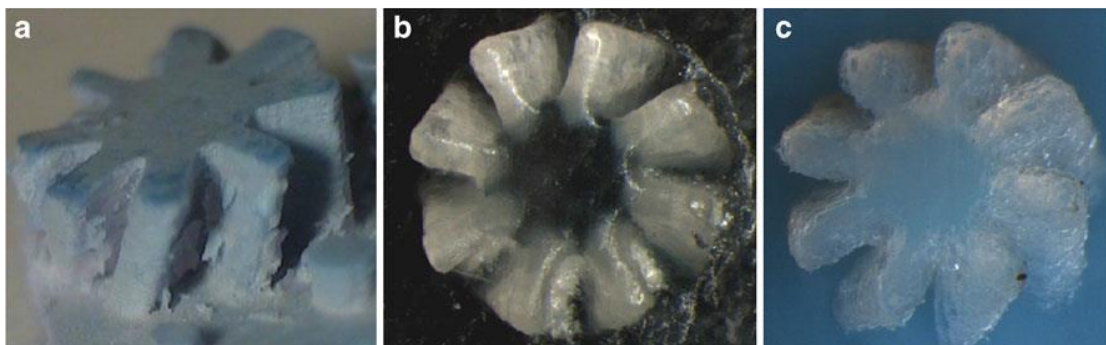


Figure 16 Products of 3D printing technology [36].

## 4.2 Ceramic Robocasting

The robocasting method was the first-generation extrusion ceramic 3D printing technology that was applied to various kinds of ceramic-based material [38]. Cesarano et al. developed this technique in Sandia National Laboratories in 1988. In this process, a ceramic slurry was extruded onto a platform, which contained a heat source to dry the deposited slurry and maintain the shape of the printed part. The slurry used in Cesarano's experiment contained 50 % to 65 % volume fraction of ceramic powder and 1 % organic additives; the remainder comprised volatile solvent. The nozzle of the printer ranged from 30 nm to 2000 nm, and the printer had a maximum speed of 150 mm/s. As the raw material was in slurry form, the part produced by this technique might have experienced deformation during the drying process. Figure 17 shows examples of the final product produced by the robocasting method [39].

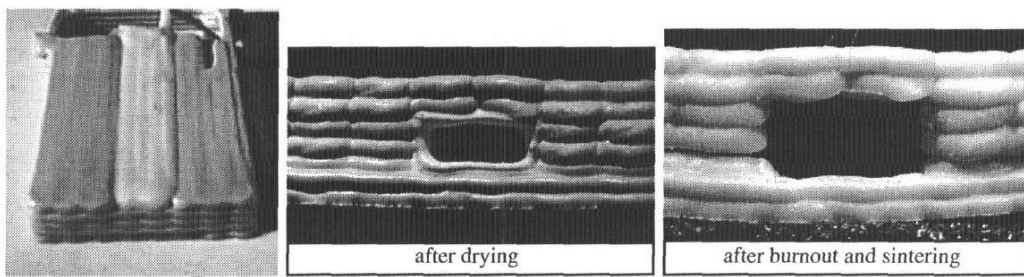


Figure 17 Part fabricated by robocasting [35].

Hilmas et al. from Missouri University of Science and Technology modified the robocasting technique in 2006 by developing a new method: freeze freeform extrusion. Instead of using a heated platform to dry the printed part, they freeze-dried the printed part at  $-16\text{ }^{\circ}\text{C}$  to avoid the deformation caused by the drying process [40]. Figure 18 shows the final product printed by the Hilmas method. This method ensured a fast forming rate of the extruded part to avoid collapse during the conventional drying process.

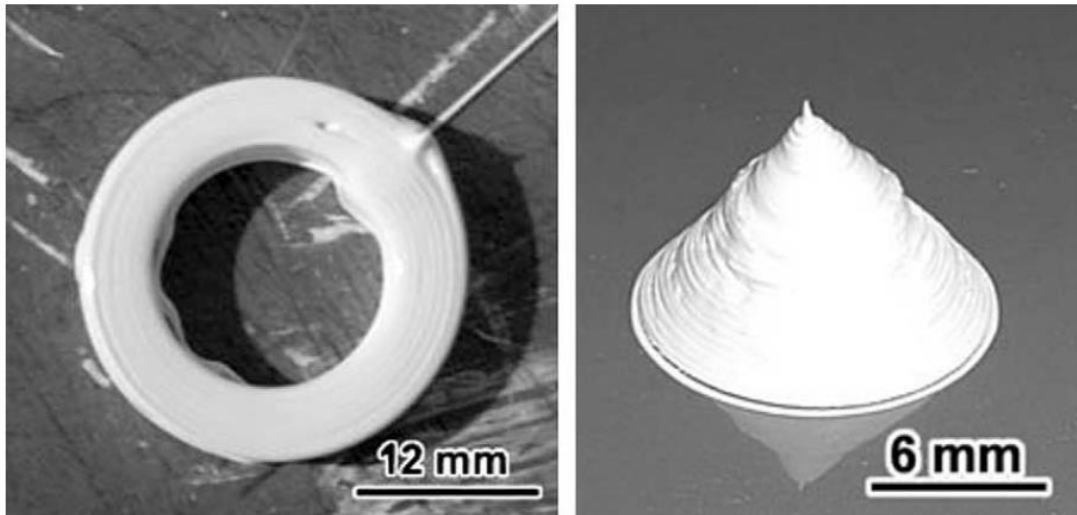


Figure 18 Cylinder and solid cone fabricated using the Hilmas method [36].

Scheithauer et al. improved the binder for the robocasting method in 2015, as shown in Figure 19. They combined thermoplastic, which has a low melting temperature and viscosity, with ceramic powder and transformed them into a slurry. During the printing process, a steady heat source was added to the cylinder to avoid solidification of the inside slurry. In their research, Scheithauer et al. employed a process similar to the robocasting method, but their platform was air-dried without heating or freezing [41].

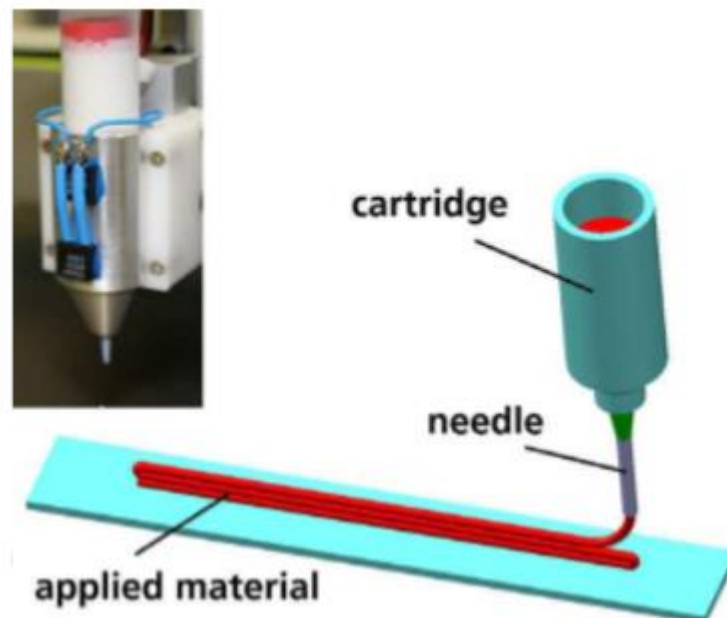


Figure 19 Scheithauer et al.'s thermoplastic extrusion method [37].

Peng et al. combined the freeform extrusion method with a laser subtractive process and successfully produced an embedded microchannel with a bulk density of 94 %. They have successfully produced thin channels with a wall thickness of 60  $\mu\text{m}$  and no obvious defect after sintering [11].

A variety of ceramic materials can be utilized in the robocasting method. As of 2018, researchers had successfully produced  $\text{ZrO}_2$ ,  $\text{ZrB}_2$ ,  $\text{Al}_2\text{O}_3$ ,  $\text{SiC}$ ,  $\text{Si}_3\text{N}_4$ ,  $\text{BaTiO}_3$ , PMN,  $\text{Si}_3\text{N}_4 - \text{W}$ , HA, TCP, and 6P53B glass [39, 42-57].

Although the influence of ink parameters (solid content, particle size, and viscosity) and extrusion parameters (extrusion rate, nozzle travel speed, and the distance between the nozzle and the previously deposited layers) have been well examined by researchers, there is no evidence of the integration of feedback signals into these processes.

### 4.3 Axiomatic Design Theory

The relationships among the functional requirements, design parameters, and process variables in the ceramic robocasting process can be analyzed using the Axiomatic Design(AD) theory. AD is a theory and method that was developed by Suh [58]. It hypothesizes that good designs comply with two axioms: independence, which refers to “Axiom 1: Maintain[ing] the independence of functional requirements (FRs)””; and information, which refers to “Axiom 2: Minimize[s] the information content” [59]. AD can be applied to design products, as well as manufacturing processes and systems [58]. AD can be employed as a systematic tool to demonstrate and analyze the current ceramic robocasting process. The materials, process parameters, machine parameters, and their influence on quality parameters can be identified by analyzing the relationships among the functional requirements, design parameters, and process variables. Four design domains can be involved: customer (knowing what is valued and containing customer and stakeholder needs, known as CNs), functional (knowing what it does and containing functional requirements, known as FRs), physical (knowing what it looks like and containing design parameters, known as DPs), and process (knowing how it is made and containing process variables, known as PVs). FRs, DPs, and PVs are to be developed in top-down, parallel hierarchies of abstraction, from high levels that define more abstract concepts as major branches to detailed (“leaf”) levels by zigzagging. These hierarchies are shown in Figure 20 [59].

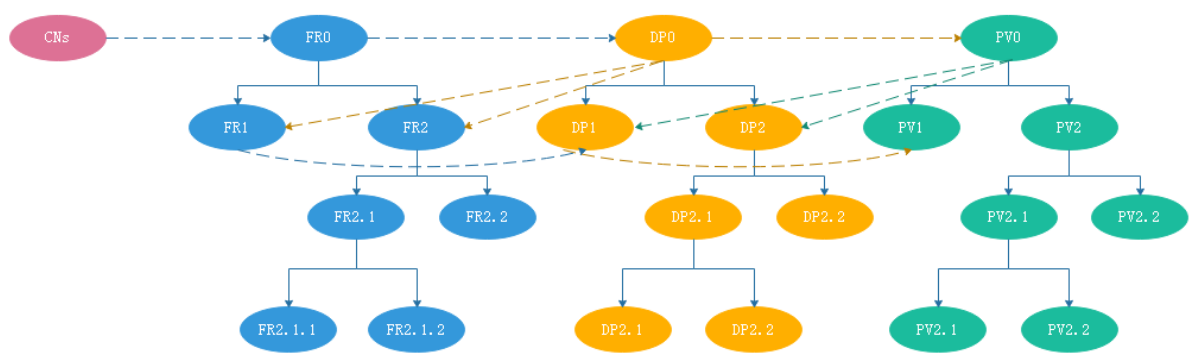


Figure 20 Top-down structure and relationships among domains [59].

CNs initiate value chains that link through FRs, DPs, and PVs. FRs are developed from CNs to define the objectives of design problems in technical terms. They are desired functions that satisfy CNs. Design solutions can be no better than their FRs [58]. At each level in their hierarchies of abstraction, FRs should be developed in solution neutral environments, i.e.,



before solutions are sought, DPs for FRs, and PVs for DPs. If it is difficult to find several candidate DPs to fulfill an FR, then that FR might not be sufficiently solution neutral, perhaps because it has too much physical content and is too close to the DPs. In these cases, solution spaces could be unnecessarily restrictive, impeding creativity. Such FRs should be moved away from the physical domain and closer to the customer domain [60]. Constraints can eliminate some candidate DPs. Suh's first axiom can eliminate others candidate DPs. The remaining DPs are ranked for information content using Suh's second axiom.

Most literature on AD focuses on just FRs and DPs as well as their accompanying functional-physical relations for new products. These relations can be expressed in design matrices to check their compliance with Axiom 1 [61]. Few authors apply AD to manufacturing processes.

Sometimes new manufacturing processes must be created; for example, photolithography was created for processing integrated circuits in the 1950s and 60s. Manufacturing processes can also be considered products and be developed with FRs and DPs. As with additive manufacturing, these products function to enable the production of many new components for consumer products and manufacturing tools [30]. Concepts for new manufacturing processes can arise during product development or possibly from re-engineering existing processes. To realize these new concepts, new knowledge is required. This acquisition of knowledge is relevant to aspects of concept-knowledge (C-K) theory [62], which is an aspect of design that is not directly addressed in AD; it is less about generating details of new concepts for creative design solutions and more about selecting design solutions. AD does, however, produce novel integrated designs and can reveal the need for novel-detailed elements to comply with the axioms.

New processes can be developed with new products by zigzagging from FRs to DPs, then from DPs to new PVs. In this way, "value [additions for CNs] should be satisfied by FRs and fulfilled by DPs, then produced by PVs" [63]. Design and process matrices are developed sequentially in each branch and at each level of the hierarchies of abstraction. Alternatively, new CNs can be defined for new processes, which can be developed independently of specific consumer products.

During zigzagging decompositions, candidate DPs should be checked against any constraints, such as cost. In addition, constraints may arise from the first canon of engineering ethics: "hold paramount the safety, health, and welfare of the public." Logically, sustainability is implied by this statement.

The imposition of new constraints, such as sustainability, can be one motivation for re-

engineering. Constraints and Axiom 1 can eliminate some candidate design solutions. Suh's second Axiom (minimizing information) can be used to find the best of the remaining candidate solutions.

Compliance with Suh's first Axiom (independence) can be checked next. Axiom 1 is also applied to FR development in decompositions. Child FRs must be collectively exhaustive (CE) with parent FRs and mutually exclusive (ME) with each other [64]. The lack of mutual exclusivity among FRs could result in coupled solutions no matter which DPs are selected.

Information content can be related to the probability of fulfilling FRs, optimization criteria (OCs) and selection criteria (SCs), as well as avoiding constraints [65].

For many existing design solutions, CNs and FRs may never have been adequately articulated. The FRs for an existing design can be developed by a process of surmising or interpolation between existing DPs and CNs. This supposes that DPs are known, as they could be determined by dissecting existing artifacts. CNs can be imagined by considering the needs of users and stakeholders. Articulating CNs can also suggest new FRs for re-engineering.

Some coupled designs can be decoupled, which eliminates imaginary complexity, by manipulating the design matrix of newly developed FRs and existing DPs. Imaginary complexity occurs when design solutions appear to be coupled, although they can be decoupled by rearranging their design matrices to be triangular [66]. In these decoupled designs, there would be specific orders of adjustment of DPs whereby all FRs can be brought into tolerance without iterating. There can be more than one such order of adjustment if a design or process matrix is not fully triangular. To apply this process to existing design solutions, FRs must be developed if they are not already stated. Relations with DPs should be established via design equations, as in  $FR_i = f(DP_i, DP_j, DP_k \dots)$ , including all FRs in each level in each branch of the design decomposition. Design matrices show the relations between FRs and DPs, including unwanted coupling. Design matrices indicate whether the adjustment of DPs is needed to satisfy FRs, without unproductive, unnecessary iterations. This same procedure can be applied to DPs, PVs, and process matrices, although when designing a process, DPs are inputs for the design process. Unlike FRs, these are generally specified in the product designs.

Sometimes a specific FR will be influenced by multiple DPs; however, the design can still be considered uncoupled. Additional judgment should be considered. Tolerances on the FRs impact the independence and the degree to which Suh's Axiom 1 can be satisfied [67]. For any given FR, its chosen DP should be treated as its principal design parameter. Other DPs could influence that FR in a minor way. If an FR is influenced by its principle DP and multiple minor DPs, tolerances on FRs can determine whether this design is coupled. If the tolerances are

greater than the influences produced by minor DPs, designs are uncoupled; otherwise, they are coupled. FR tolerances might be assigned by designers; they might be within three standard deviations of the FR in the current production. The regularity (R) and semangularity (S) of the FRs, which quantify the degree of coupling, can also be used to determine the independence (Suh's Axiom 1) [67]. When R and S are unity (1), designs are uncoupled; when R and S are 0, designs are fully coupled.

## 4.4 Control System Engineering and Control Systems in Ceramic Additive Manufacturing

Based on the research of Norbert Wiener, the control system has a more extended history than humanity, as it exists in all aspects of the world, ranging from animals to machines [68]. By definition, a control system “consists of subsystems and processes (or plants) assembled to obtain a desired output and output with desired performance, given a specified input” [69]. It is well known that, in the manufacturing process, a control system can be used to achieve power amplification, remote adjustment, and compensation for disturbance. The control system can be divided into two main categories: the open-loop system and the closed-loop system, as shown in Figure 21. In the open-loop system, the process follows a linear pattern: once the system is defined, any disturbances generated during the process cannot be canceled or taken into consideration. In the closed-loop system, disturbances can be compensated by sending the measured in-process signal back through a feedback path for comparison and adjustments [69]. With the in-process adjustments, the closed-loop system regularly demonstrates higher accuracy than the open-loop system. Figure 21 can be further developed into a block diagram, as shown in Figure 22.  $R(s)$  represents the reference target (or input) of the system,  $E(s)$  represents the error in the system,  $G(s)$  is the forward transfer function, and  $H(s)$  is the feedback transfer function. The transfer function for open-loop systems and closed-loop systems can be expressed by equations (1–4) .

$$E(s)_o = R(s)_o - C(s)_o \quad (1)$$

$$E(s)_c = R(s)_c - C(s)_c \quad (2)$$

$$C(s)_o = R(s)_o * G(s) \quad (3)$$

$$C(s)_c = (R(s)_c - H(s) * C(s)_c) * G(s) \quad (4)$$

where  $o$  represents the open-loop system, and  $c$  represents the closed-loop system. By combining these equations, the error for open-loop systems and closed-loop systems can be defined as

$$E(s)_o = R(s)_o(1 - G(s)) \quad (5)$$

$$E(s)_c = R(s)_c \left(1 - \frac{G(s)}{1 + H(s) * G(s)}\right) \quad (6)$$

By comparing equations (5–6), it can be concluded that a closed-loop system may perform better when the feedback transfer function's output is negative feedback.

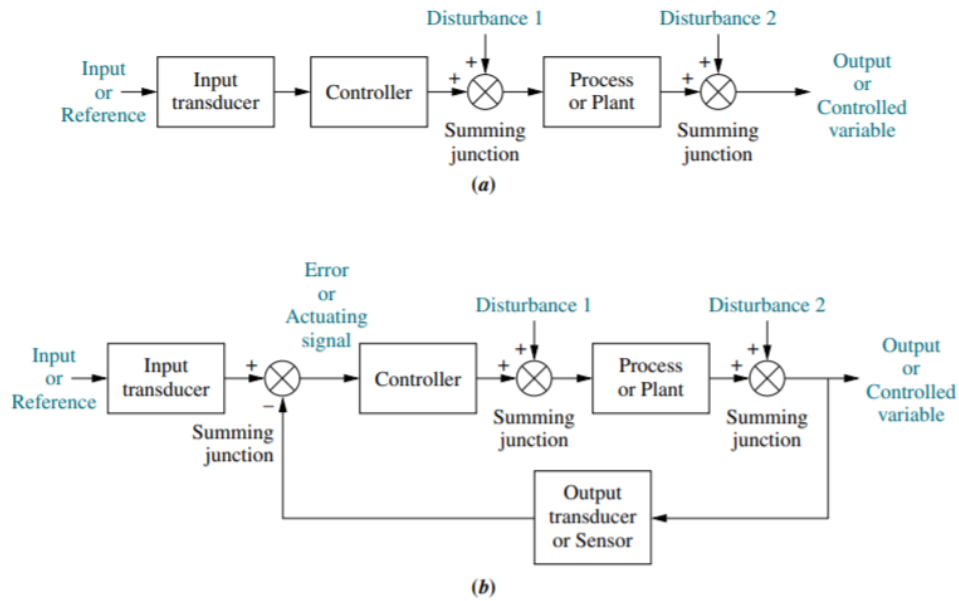


Figure 21 Block diagrams of control systems: (a) open-loop system and (b) closed-loop system [69].

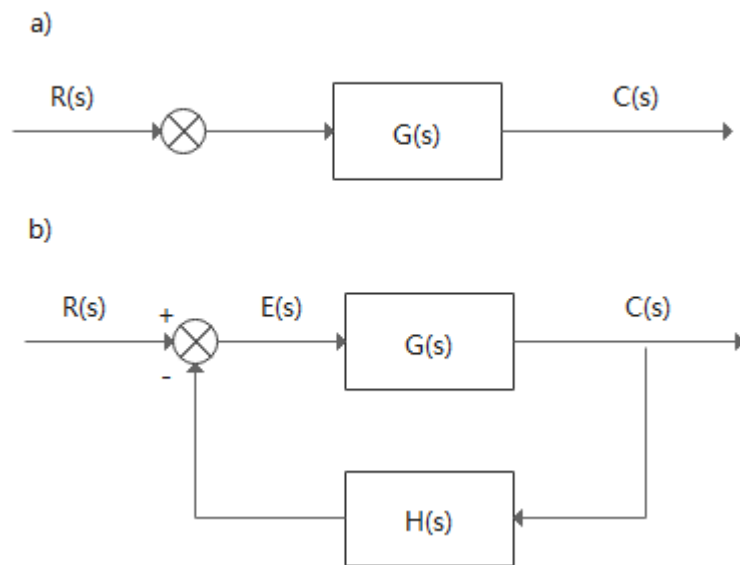


Figure 22 Block diagrams of control systems: (a) open-loop system and (b) closed-loop system [69].

#### 4.4.1 Proportional–Integral–Derivative Controller

The PID controller is a prevalent and well-developed closed-loop control strategy due to its simple architecture and easy adjustment [70]. The PID controller's engineering application history can be traced back to the 1930s [71].

PID control governs output by using proportional, integral, and derivative calculations to regulate errors between input and output, as expressed by equation (7) [72]:

$$\text{Output} = K_p * e(t) + K_i * \int_0^t e(t) + K_d * \frac{de}{dt} \quad (7)$$

where  $K_p * e(t)$  is the proportional controller term,  $K_i * \int_0^t e(t)$  is the integral controller term, and  $K_d * \frac{de}{dt}$  is the derivative term. The proportional term accelerates the response of the system. The integral term increases the system response speed but produces oscillations. The derivative reduces oscillations [72].

The conventional PID controller has been successfully applied by the industry for almost a century; however, this control method still has some disadvantages. First, this method requires a well-developed accurate dynamic model of the controlled process, which is the key to creating the feedback control loop [15]. Second, the conventional PID controller is usually only suitable for a single-input single-output system. Conventional PID and PID-like control schemes are not flexible in addressing a single-input multiple-outputs system. PID control logic is not flexible in handling systems in which uncertain factors exist, such as modeling errors and external disturbances [70].

## 4.4.2 Artificial Neural Network

The artificial neural network, which is a data-driven decision-making approach, provides the chance to bypass the complex physics equations and map the real-time status into control actions via experience [16].

A schematic drawing of the ANN model structure is shown in Figure 23. The ANN commonly contains one input layer, one output layer, and several hidden layers. Nodes, which are inspired by neurons in the brain, are significant components of an ANN. Arrows connect these nodes and also point out the direction of the data flow. The relationships among inputs, outputs, and nodes can be expressed as shown in equations (8–11):

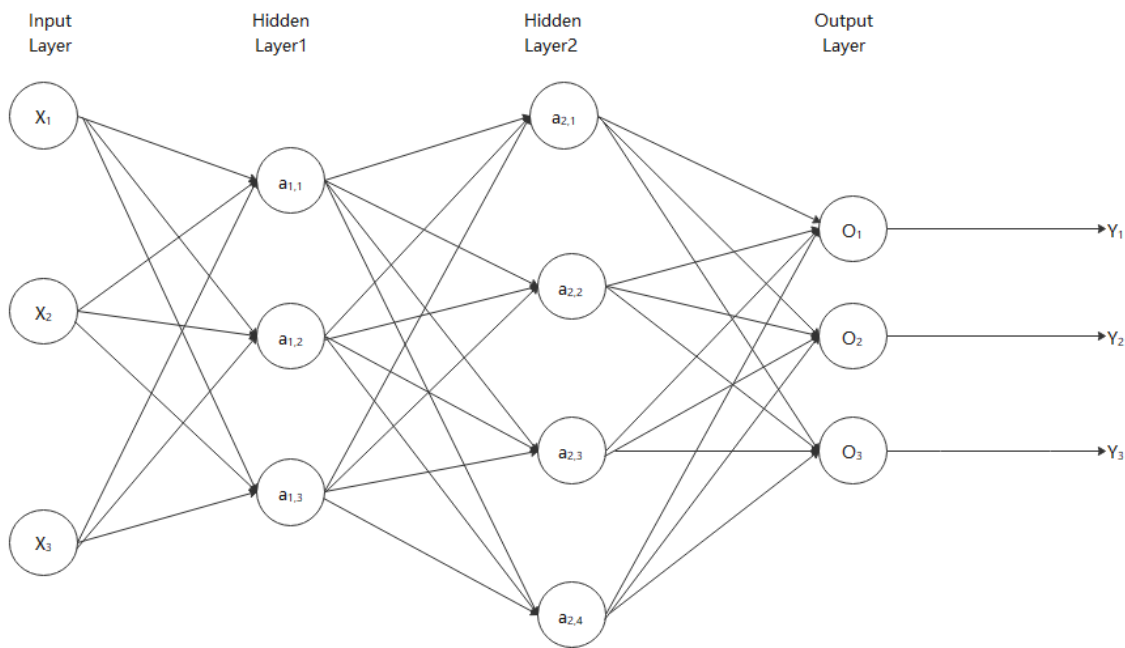


Figure 23 Schematic of the artificial neural network.

$$a_{1,j} = f\left(\sum_{i=0}^3 (w_{1,i} * x_i) + b_1\right) \quad (8)$$

$$a_{2,j} = f\left(\sum_{j=0}^3 (w_{2,j} * a_{1,j}) + b_2\right) \quad (9)$$

$$O_1 = f\left(\sum_{k=0}^4 (w_{3,k} * a_{2,k}) + b_3\right) \quad (10)$$

$$E_k = \frac{1}{2} \sum (y_i - O_i)^2 \quad (11)$$

where  $x$  and  $y$  represent the real inputs and outputs, respectively;  $O$  represents the outputs layer;  $w$  is the weight assigned to the neurons;  $b$  is the bias of the layer; and  $E_k$  is

the standard error. The function (f) is the activation function (AF), which regulates the output in given input conditions. Nwankpa et al. have reviewed the performance of 21 types of activation functions that were developed before 2018 and mentioned that each activation function has advantages and disadvantages [73]. They also stated that most of the latest activation functions had rarely been applied in practice. In contrast, current practices are more dependent on the well- developed activation functions. Thus, in this review, only the most widely used activation functions are listed and compared.

The sigmoid function is a nonlinear function that is widely used in feedforward neural networks. The Sigmoid function is a smooth function that is convenient for derivation; the output of this function is between (0, 1) to ensure an accurate data amplitude. The disadvantage of this function is that it does not have a zero-centered output, which will affect the gradient's result and efficiency [73].

The hyperbolic tangent function (Tanh) performs better in the multilayer network than the sigmoid function by producing a zero-centered output. The disadvantage is that this function may come across the vanishing gradient problem [73].

The rectifier neural networks (rectified linear unit, ReLU) method is advantageous regarding the gradient propagation property [74], which renders this function less likely to become saturated than other functions. A smooth version of ReLU is referred to as the softplus function. This function can improve deep learning network performance due to the advantage of nonzero gradient properties that provide enhancement [73].

Figure 24 summarizes the equations and graphs of the sigmoid, tanh, ReLU, and softplus functions.

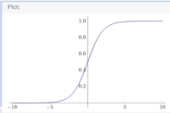
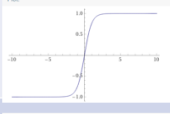
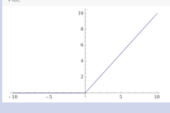
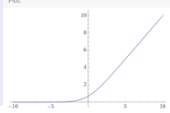
Activation function	Equation	Graph of the function
<b>Sigmoid</b>	$f(x) = \frac{1}{1 + \exp^{-x}}$	
<b>Tanh</b>	$f(x) = \frac{e^x - e^{-x}}{e^x + e^{-x}}$	
<b>ReLU</b>	$f(x) = \max(0, x)$ $= \begin{cases} 0, & x < 0 \\ x, & x \geq 0 \end{cases}$	
<b>Softplus</b>	$f(x) = \log(1 + \exp^x)$	

Figure 24 Equation and graphs of commonly used activation functions.



Aside from activation functions, the optimization model also has an essential role in the ANN. ANN algorithms aim to build an optimization model and weight each parameter in the objective function using the provided datasets. Sun et al. completed a comprehensive review of all optimization methods that were developed before 2019 [75]. Figure 25 shows a summarized comparison of different optimization methods by Sun et al. [75]. Since the focus of this research is to identify a feasibility analysis of machine learning-enabled closed-loop control in the ceramic AM method instead of distinguishing the best optimization method, only one of these optimization methods was chosen to carry out the research.

As the artificial neural network method can build empirical models based on collected historical data, the output can be predicted without a well-constructed physical model. These predicted results can also be treated as the input (replacing the conventional controller) to optimize the operation and improve the product quality.

Method	Properties	Advantages	Disadvantages
GD	Solve the optimal value along the direction of the gradient descent. The method converges at a linear rate.	The solution is global optimal when the objective function is convex.	In each parameter update, gradients of total samples need to be calculated, so the calculation cost is high.
SGD [1]	The update parameters are calculated using a randomly sampled mini-batch. The method converges at a sublinear rate.	The calculation time for each update does not depend on the total number of training samples, and a lot of calculation cost is saved.	It is difficult to choose an appropriate learning rate, and using the same learning rate for all parameters is not appropriate. The solution may be trapped at the saddle point in some cases.
NAG [105]	Accelerate the current gradient descent by accumulating the previous gradient as momentum and perform the gradient update process with momentum.	When the gradient direction changes, the momentum can slow the update speed and reduce the oscillation; when the gradient direction remains, the momentum can accelerate the parameter update. Momentum helps to jump out of locally optimal solution.	It is difficult to choose a suitable learning rate.
AdaGrad [30]	The learning rate is adaptively adjusted according to the sum of the squares of all historical gradients.	In the early stage of training, the cumulative gradient is smaller, the learning rate is larger, and learning speed is faster. The method is suitable for dealing with sparse gradient problems. The learning rate of each parameter adjusts adaptively.	As the training time increases, the accumulated gradient will become larger and larger, making the learning rate tend to zero, resulting in ineffective parameter updates. A manual learning rate is still needed. It is not suitable for dealing with non-convex problems.
AdaDelta/ RMSProp [31], [32]	Change the way of total gradient accumulation to exponential moving average.	Improve the ineffective learning problem in the late stage of AdaGrad. It is suitable for optimizing non-stationary and non-convex problems.	In the late training stage, the update process may be repeated around the local minimum.
Adam [33]	Combine the adaptive methods and the momentum method. Use the first-order moment estimation and the second-order moment estimation of the gradient to dynamically adjust the learning rate of each parameter. Add the bias correction.	The gradient descent process is relatively stable. It is suitable for most non-convex optimization problems with large data sets and high dimensional space.	The method may not converge in some cases.
SAG [36]	The old gradient of each sample and the summation of gradients over all samples are maintained in memory. For each update, one sample is randomly selected and the gradient sum is recalculated and used as the update direction.	The method is a linear convergence algorithm, which is much faster than SGD.	The method is only applicable to smooth and convex functions and needs to store the gradient of each sample. It is inconvenient to be applied in non-convex neural networks.
SVRG [37]	Instead of saving the gradient of each sample, the average gradient is saved at regular intervals. The gradient sum is updated at each iteration by calculating the gradients with respect to the old parameters and the current parameters for the randomly selected samples.	The method does not need to maintain all gradients in memory, which saves memory resources. It is a linear convergence algorithm.	To apply it to larger/deeper neural nets whose training cost is a critical issue, further investigation is still needed.
ADMM [123]	The method solves optimization problems with linear constraints by adding a penalty term to the objective and separating variables into sub-problems which can be solved iteratively.	The method uses the separable operators in the convex optimization problem to divide a large problem into multiple small problems that can be solved in a distributed manner. The framework is practical in most large-scale optimization problems.	The original residuals and dual residuals are both related to the penalty parameter whose value is difficult to determine.
Frank-Wolfe [118]	The method approximates the objective function with a linear function, solves the linear programming to find the feasible descending direction, and makes a one-dimensional search along the direction in the feasible domain.	The method can solve optimization problems with linear constraints, whose convergence speed is fast in early iterations.	The method converges slowly in later phases. When the iterative point is close to the optimal solution, the search direction and the gradient of the objective function tend to be orthogonal. Such a direction is not the best downward direction.

Figure 25 Summary of first-order optimization methods [75].



**Part 1.4:** Evaluate the influence of each material, machine, and process parameter on the intermediate parameters. Investigate the impact of the intermediate parameters on the quality parameters. Analyze the current robocasting process using Axiomatic Design theory. These relationships are specified by the literature review and designed experiments. Collect these data for the database in Part 2.

**Part 2:** Create a database for the robocasting process. Build a model that can describe the process–quality relationship of the ceramic robocasting method.

**Part 2.1:** Construct a model based on the collected data in Part 1.4 for the robocasting process. A “process parameter–intermediate parameter–quality parameter” database is generated. This database serves as a guideline to optimize the robocasting process. A machine learning software package is used as a tool for control and optimization.

**Part 3:** Integrate closed-loop control into the robocasting process based on the created database. Validate the developed closed-loop control using experimental data.

**Part 3.1:** Integrate sensors into the robocasting system. Modify the conventional open-loop process to a closed-loop process, as shown in Figure 24. Instead of generating G-code before the start of the print, the G-code is sorted into paths. The G-code for the next path is generated based on the in-process signal and real-time feedback signal.

**Part 3.2:** Record and compare the pressure history of the print of the original process and controlled process. Examine the quality of the models that are produced by the open-loop process and machine learning-enabled closed-loop control process.

## 6 Results

### 6.1 Model of the Extruder Unit of Robocasting

The robocasting printer that is used in this study is the 3D PotterBot 7 (3D Potter, Inc., Florida) with a modified extruding unit, as shown in Figure 27. The printer is controlled by a Smoothieboard microprocessor that is loaded with Smoothieware firmware. The printer's original make contains a cylinder with a diameter of 3 inches and a nozzle with a diameter of 3 mm. We remodeled the printer to integrate the sensor into the system and improve the resolution of the print. The upper cylinder was applied to attach the extruder unit to the machine frame, as shown in Figure 27 and Figure 28. A commercial 10 cc syringe (10cc, Global Easy Gide, China) with a 0.84 mm (18 g, GMS, China) needle was attached to the lower cylinder. Two pistons were connected to the back of the plunger to transfer linear motions from the ball thread to the ceramic slurry. A 50-kg button loadcell (CZL204E, Phidgets, Canada) was attached between two pistons to monitor the ceramic slurry pressure change. An Arduino Uno microcontroller board (A000066, Arduino, Massachusetts) and the HX711 24-Bit Analog-to-Digital Converter (Avia, China) were programmed to collect data from the button loadcell at a sampling rate of 10 Hz. The pressure change is calculated based on the loadcell sensor reading over the plunger area. As the plunger area is a constant in this study, the reading of the loadcell was utilized as a measure of pressure.



Figure 27 Schematic of the ceramic robocasting machine with a customized extruding unit [76].

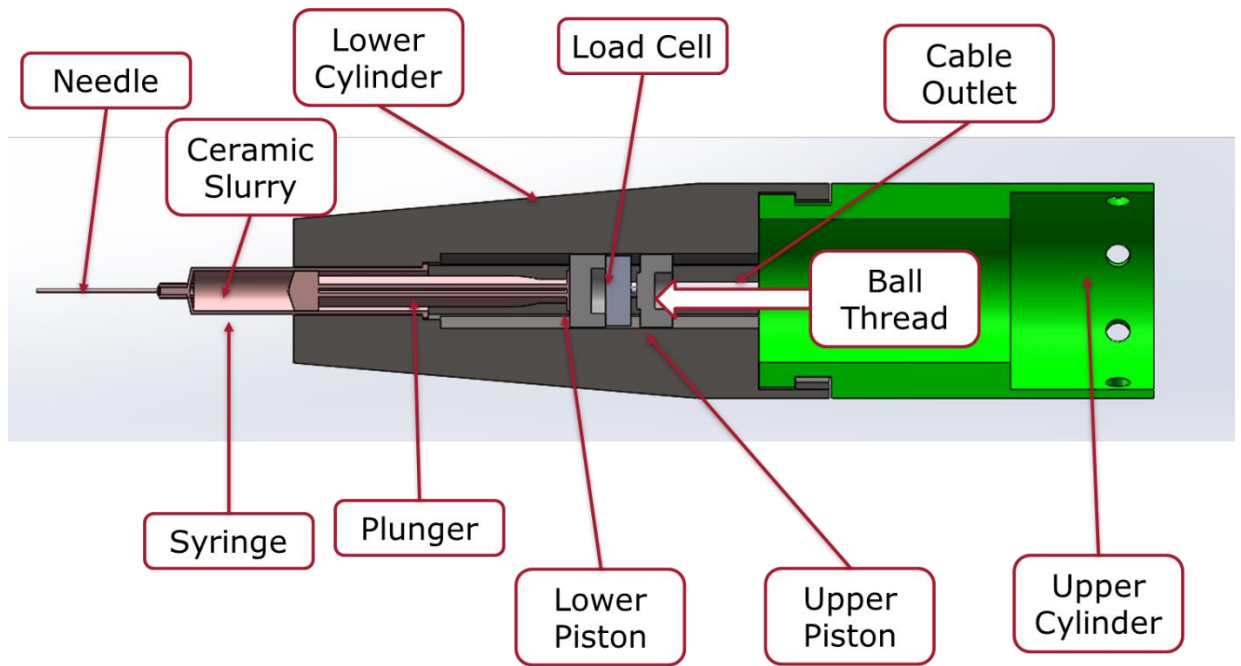


Figure 28 Model of the extruder unit of the robocasting system.

## 6.2 Model of Design Patterns for This Research

Three design patterns were employed in this research.

Design pattern #1 is shown in Figure 29. This pattern was printed at different travel speed-extrusion speed combinations, while the travel speed is fixed at 1200 mm/min. The travel speed is defined as the speed of linear motion in the X, Y, and Z directions, while the extrusion speed describes the rate of slurry extruded out of the nozzle. The pattern contains 11 paths; each path has a length of 20 mm with a 2-mm gap between nearby tracks. The model was printed starting from the green dot to the red dot, while the orange dots comprised the extruding point. The total travel distance between the starting point and the ending point was 240 mm, while the distance between two neighboring extruding points was 20 mm. The nozzle of the extruder was an industrial needle with a diameter of 0.84 mm; so the ideal cross-sectional profile of the printed filament should be a circular shape with a diameter of 0.84 mm and a cross-sectional area of  $0.54 \text{ mm}^2$ . However, since the slurry employed in this study was a fluid, the cross-sectional shape will eventually be transformed into an arched shape. This pattern was the basic component of design patterns #2 and #3; it was used to test the influence of the travel-extrusion speed combinations.

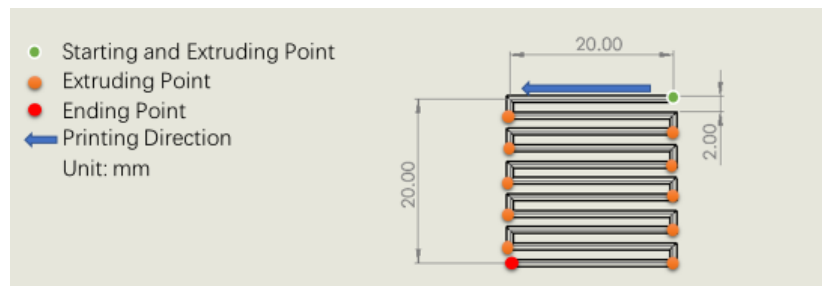


Figure 29 Schematic of design pattern #1 for testing the influence of different speed combinations. Units in mm.

Design pictures and specified geometries of design pattern #2 are shown in Figure 30. The pattern is a stack-up of two design pattern #1 layers. Each layer was printed in the length direction first, followed by the width direction. As shown in Figure 30, image b), eight two-layer lattice patterns were printed layer by layer. The lower layer (shown in white) was printed from the left side to the right side (from model #8 to model #1), and then the upper layer (shown in red), which is orthogonal to the lower layer, was printed from the right side to the left side (from model #1 to model #8). As these two layers were printed in the reverse direction, the interval time between two layers for a specific model increases 24 seconds from the right side to the left side (from model #1 to model #8). To ensure that the height difference between two

printed models is only a result of different layover times between layers, the extrusion speed and travel speed was kept constant at 1200 mm/min. This pattern is applied to study the deflection and deformations between layers.

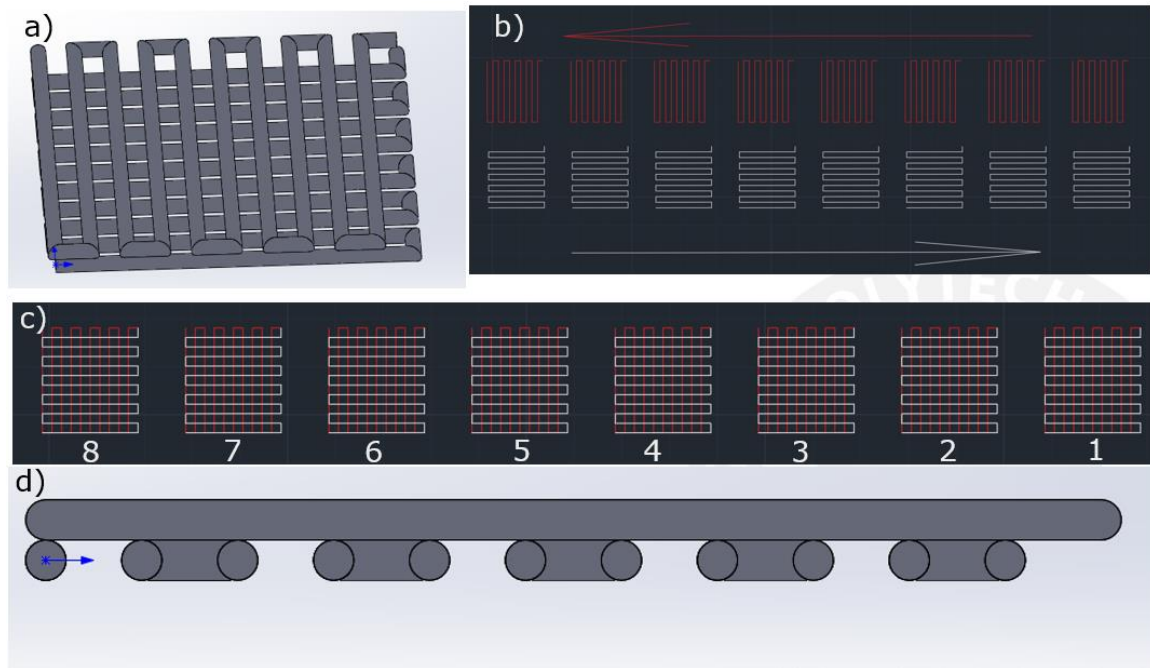


Figure 30 Schematic of the experiment for testing the height between the upper layer and the lower layer.

Design pattern #3 is shown in Figure 31. This pattern contains nine individual single-layer models, which are built up by 11 tracks. The distance between each model is 10 mm. This pattern is used to construct and verify the efficiency of the closed-loop control modification.

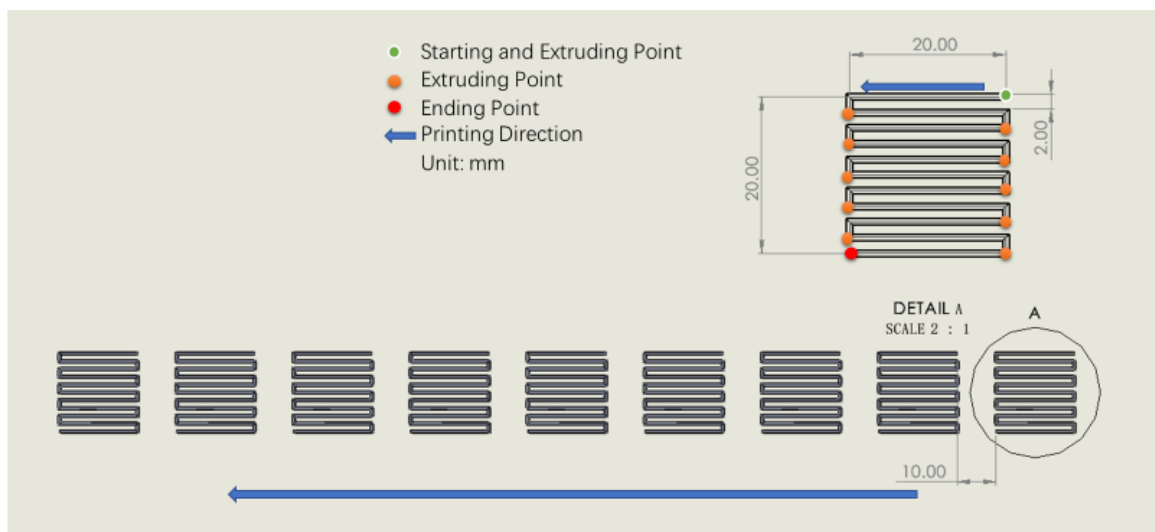


Figure 31 Schematic of the pattern designed for closed-loop control construction and verification. Units in mm.



### 6.3 Defining the Parameters in Robocasting Technology and Characterizing Their Relationships

The relationships among the machine, material, and process parameters have been carefully investigated, and the established relationship that was used to guide this project is summarized in Figure 32. The data that represents these relationships were collected in experiments that are discussed in this chapter.

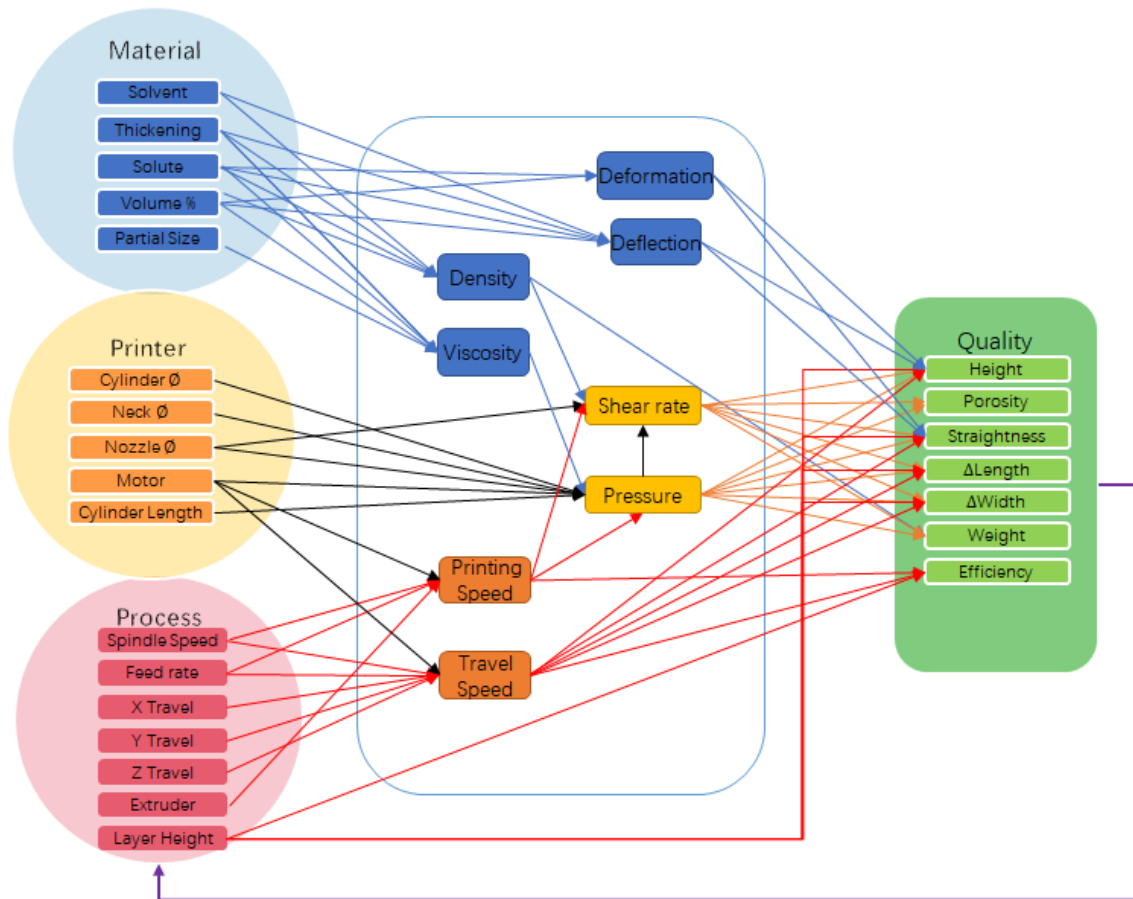


Figure 32 Relationships among machines, materials, and process parameters with quality parameters.

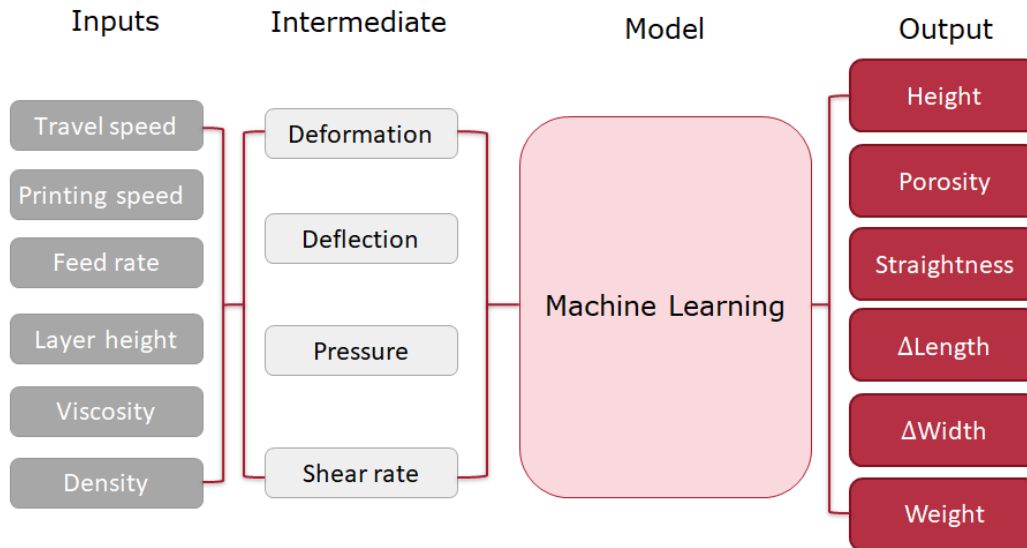


Figure 33 Schematic of the overall approach proposed in the current project to establish the relationships among processes, intermediate values, and quality parameters.

Figure 33 is a comprehensive machine learning path to determine the correlation mentioned in Chapter 5. The inputs of the machine learning include material information, such as density and viscosity, and process information, such as travel speed, printing speed, feed rate, and layer height. These parameters are actual variables that can be adjusted and are comparable to the process parameters of the conventional machining operations. The intermediate values contain the deformation (of the lower layer), deflection (of the higher layer), pressure (of the piston and nozzle), and shear rate (at the nozzle). These parameters are treated as in-process measurements for closed-loop control. The simulation output includes quality parameters, such as the height, length, width, and weight of the as-printed part, compared to the targeted dimensions. The prediction includes information such as porosity and volume fraction. Furthermore, this model can be used to optimize the robocasting process parameters by weighing and combining these predictions.

In this research, the relationships among the pressure, length of extrusion, and width of the printed green part were analyzed to prove the feasibility of machine learning-enabled closed-loop control in the robocasting process. The collected starting and ending pressure were utilized as inputs for training the machine learning model, while the length of extrusion was the output for training the model. After the machine learning model was trained, the desired length of the extrusion was predicted based on the in-process pressure and targeted pressure. The dimensional quality of the printed pattern was improved by adopting the machine-learning-enabled closed-loop control.

## 6.4 Material Parameters

Material parameters of the robocasting process include the characteristics of the solvent, dispersant, and solution, which influence the density, viscosity, and deformation of the ceramic slurry.

### 6.4.1 Density of the Slurry

The density of the slurry is determined by the density of the solvent ( $\rho_{solvent}$ ), density of the dispersant ( $\rho_{dispersant}$ ), density of the solute ( $\rho_{solute}$ ), volume fraction of the solvent ( $Vol\%_{solute}$ ), and weight fraction of the thickening agent inside the solute ( $Wt\%_{thickening\ agent\ t}$ ).  $V_{solvent}$  represents the volume of the solvent, while  $V_{solute}$  represents the volume of the solute. The following equations were used to calculate the density of the slurry [77]:

$$\rho_{slurry} = \frac{\rho_{solvent} * V_{solvent} * (1 + Wt\%_{thickening\ agent}) + \rho_{solue} * V_{solute}}{V_{solvent} + V_{solute}} \quad (12)$$

$$Vol\%_{solute} = \frac{V_{solvent}}{V_{solvent} + V_{solute}} \quad (13)$$

### 6.4.2 Viscosity of the Slurry

The viscosity of the slurry is based on the density of the solvent ( $\rho_{solvent}$ ), density of the dispersant ( $\rho_{dispersant}$ ), density of the solute ( $\rho_{solute}$ ), volume fraction of the solvent ( $Vol\%_{solute}$ ), and weight fraction of the dispersant inside the solute ( $Wt\%_{dispersant}$ ). According to the literature, the slurry for the robocasting process should be a thixotropic Herschel–Bulkley fluid, which allows the extrusion to be self-adjusted with delay [78-80]. The following experiment was designed to measure the apparent viscosity. The ceramic powder used in these experiments was aluminum oxide powder (1–2  $\mu\text{m}$ , US Research Nanomaterials, Inc., TX), the thickening agent was polyethylene glycol powder (poly(ethylene) oxide, PEO; 600,000 Mv, Sigma-Aldrich, MO), and the solvent was deionized (DI) water. The recipes for different samples are shown in Table 2.

Table 2 Slurries with different aluminum oxide and PEO concentrations.

Sample	Ceramic Powder	Ceramic Vol. %	Thickening Agent	Wt %	Solvent
A	2 $\mu\text{m}$ Al <sub>2</sub> O <sub>3</sub> powder	40	PEO (600,000 Mv)	5	DI Water
B	2 $\mu\text{m}$ Al <sub>2</sub> O <sub>3</sub> powder	20	PEO (600,000 Mv)	5	DI Water
C	2 $\mu\text{m}$ Al <sub>2</sub> O <sub>3</sub> powder	10	PEO (600,000 Mv)	5	DI Water
D	2 $\mu\text{m}$ Al <sub>2</sub> O <sub>3</sub> powder	10	PEO (600,000 Mv)	2.5	DI Water
E	2 $\mu\text{m}$ Al <sub>2</sub> O <sub>3</sub> powder	0	PEO (600,000 Mv)	2.5	DI Water

Aluminum oxide powder was characterized by scanning electron microscopy (SEM). Image-J software was used to analyze the SEM images. The size distribution is shown in Figure 34. The statistical results shows some large particles inside the powder sample; these particles may cause the nozzle to become clogged. As the nozzle diameter is 840  $\mu\text{m}$ , a 20  $\mu\text{m}$  sieve was used to ensure that the powder's size falls within an acceptable range. The thickening agent was added to DI water at room temperature (25 °C), and then this solution was stirred with a magnetic stirrer mixer (Standard Magnetic Stirrers, 120V, VWR, PA) at 1600 rpm for 12 hours. A jar mill mixer (#253TUM, Covington-Engineering, ID) was used to mix the slurry at 515 rpm for 24 hours. The apparent viscosity of the prepared slurry was tested by a rheometer (MCR 302, Anton-Paar, Graz, Austria) with a PP-25 test plate. A schematic of the test process is shown in Figure 35

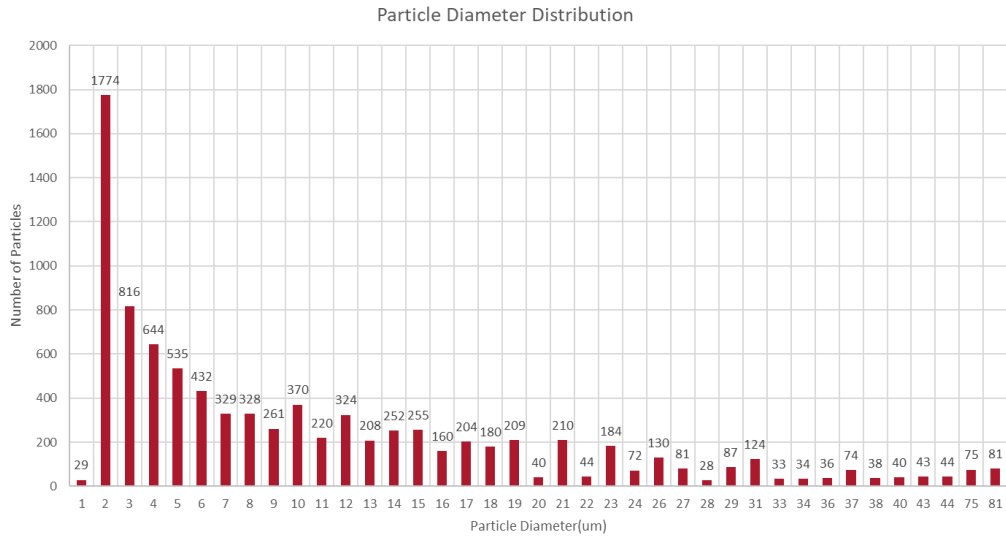


Figure 34 Particle diameter distribution.

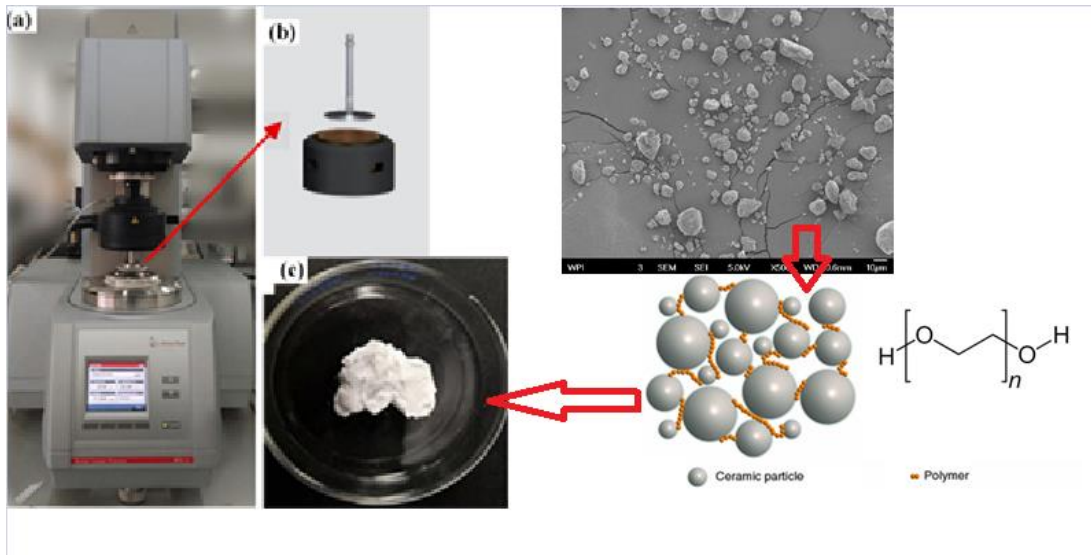


Figure 35 Demonstration of the test process: a) Anton-Paar MCR 302 Rheometer, b) PP-25 test plate, and c) ceramic slurry used in the test.

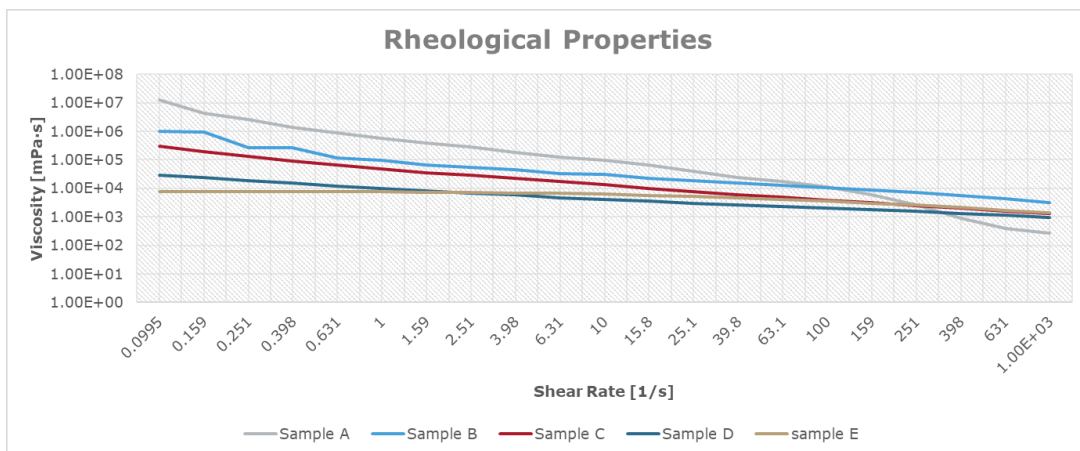


Figure 36. Rheological properties of slurries with different concentrations.

The test results show that the viscosity increases with an increase in the solute volume fraction and thickening agent weight fraction, which is similar to the conclusion in literature [81, 82].

In this study, the variable is a process parameter; so the recipe for slurry should be specified, as shown in Table 3. As the slurry used in the ceramic robocasting process commonly exhibits a shear-thinning property, its viscosity decreases with an increase in the processing pressure, which allows the extrusion to be self-adjusted with delay [78-80]. The appearance viscosity increases with the increase in the solute volume fraction and thickening agent weight fraction [81, 82]. The viscosity of the slurry is based on the density of the solvent ( $\rho_{solvent}$ ), density of the dispersant ( $\rho_{dispersant}$ ), density of the solute ( $\rho_{solute}$ ), volume fraction of the solvent ( $Vol. \%_{Solute}$ ), and weight fraction of the dispersant inside the solute ( $Wt. \%_{dispersant}$ ). The pH and ionic strength also contribute to the viscosity of the slurry [81, 82].

Table 3 Recipe for the slurry used in this study.

Ceramic Powder	Ceramic Vol. %	Thickening agent	Wt. %	Solvent
2um Alumina	20	Polyethylene oxide	5	DI Water

The relationship between the shear rate and the viscosity of the Herschel–Bulkley fluid can be described as [83]

$$\tau = \tau_y + K\dot{\gamma}^n \quad (5)$$

where  $\tau$  is the shear stress,  $\tau_y$  is the yield point,  $n$  is the shear-thinning exponent,  $K$  is the viscosity parameter, and  $\dot{\gamma}$  is the shear rate. These parameters were employed to calculate the pressure on the extruder.

Four repeated tests were carried out to test and verify the slurry's rheological properties. The acquired appearance viscosity has a similar range and trend to those described in the references [81, 84]. The data in Table 4 include a set of rheological properties for the tested ceramic slurry. The shear rate, shear stress, and viscosity were acquired by the rheometer.  $\tau_y$ ,  $K$ , and  $\dot{\gamma}$  were fitted using the measured appearance viscosity shown in Figure 38. The fitted shear stress is also included in Table 4.

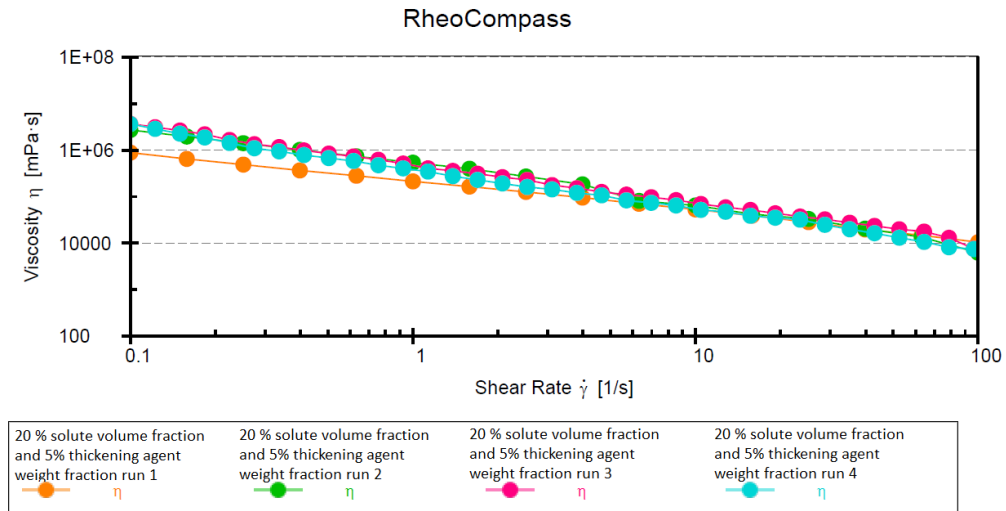


Figure 37 Appearance viscosity curve for slurries with 20 % solute volume fraction and 5 % thickening agent weight fraction.

Table 4 Rheological properties of the ceramic slurry: shear rate, measured shear stress, viscosity, and fitted shear stress.

Shear Rate	Shear Stress	Viscosity	Fitted Shear Stress
[1/s]	[Pa]	[mPa·s]	[Pa]
0.1	88.347	883000	107.02421
0.158	102.41	646000	124.74351
0.251	122.63	488000	145.66128
0.398	145.64	366000	169.98082
0.631	177.31	281000	198.3511
1	212.64	213000	231.4251
1.58	260.39	164000	269.74063
2.51	316.61	126000	314.97243
3.98	379.69	95388	367.56009
6.31	443.31	70273	428.90689
10	530.8	53093	500.42486
15.8	617.86	38996	583.2769
25.1	709.68	28259	681.08445
39.8	785.19	19727	794.798
63.1	929.57	14735	927.452
100	1047.9	10479	1082.09974

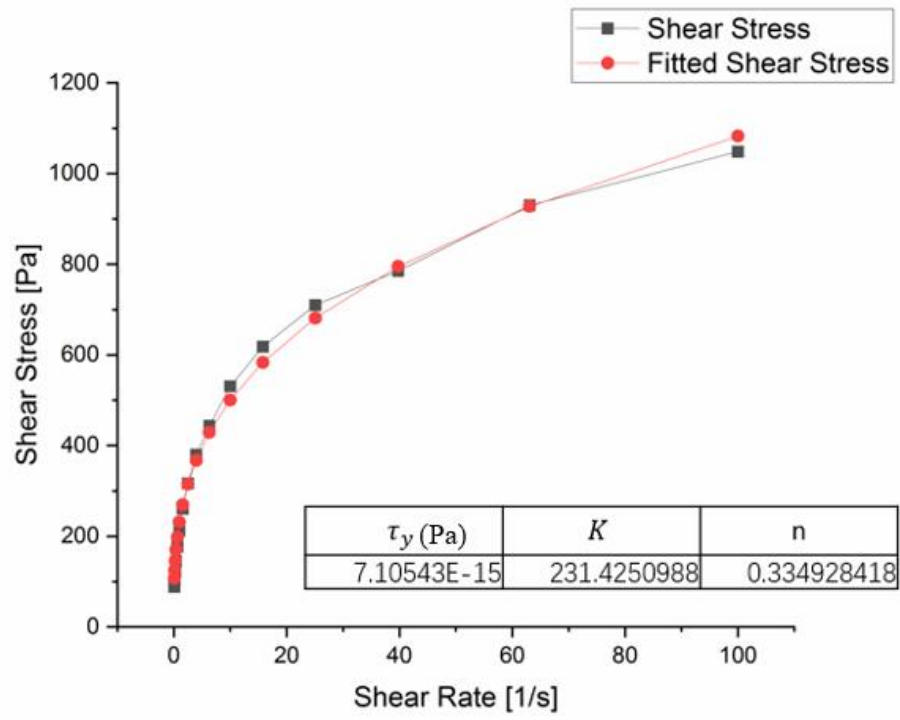


Figure 38 Tested and fitted shear stress–shear rate curve.



## 6.5 Printer Parameters

The printer parameters of the robocasting process include parameters for the extruder and parameters for the motor. The parameter for the extruder has been explained in Chapter 6.1. Motors are controlled by the G-code interpreter in the PLC unit. Ball threads, belts, and gears are used to convert rotary motions (from the motor) to linear movements (of the printing bed, nozzle, and extruder), such as travel speed and extrusion speed, by adjusting the coefficients. These coefficients are configurations in the PLC setting code. An example of these configurations are shown:

```
#define DEFAULT_AXIS_STEPS_PER_UNIT (200, 200, 3274, 300)
```

This line of code defines the axis steps per unit (steps/mm). The coefficients “200, 200, 3274, and 300” indicate the required operation of stepper motors to execute a 1 mm linear motion. The motors, which control the X-axis, Y-axis, and Z-axis, need to rotate 200 steps, 200 steps and 3274 steps, respectively, and the extruder needs to rotate 300 steps.

The coefficients for the X-axis, Y-axis, and Z-axis in this study were obtained using the factory setup. In contrast, the coefficient for the extruder was calibrated based on the model of the new extruder in section 6.1. Table 5 was generated based on the assumption that the ceramic slurry is a noncompressible viscous fluid for which the volume for a given mass is constant during the printing process. The parameters in Table 5 were applied to calibrate the coefficient for the extruder. Calibration was based on the actual print to acquire accurate coefficients.

Table 5 Coefficient for calibrating the extruder.

Original Extrusion Amount (mm)	Degree Pre-Revolution	Linear Distance at Ball Thread (mm)
950	360	2.5
Cylinder diameter (mm)		Outlet diameter(mm)
14.37		2.5
Inlet area (mm <sup>2</sup> )		Outlet area (mm <sup>2</sup> )
162.10007		4.90625
Inlet/outlet area	33.039504	
Extrusion length (mm)	Linear movement at ball thread (mm)	
1	0.0026316	
Extrusion length (mm)	Linear movement out of nozzle (mm)	Factor
1	0.0869461	0.0302668
To achieve real E 1, use this factor multiplied by the distance change		This factor is 1/(linear movement out of nozzle)
		11.501383

## 6.6 Process Parameters

Process parameters of the robocasting process include the feed rate (mm/min), travel distance (mm), spindle speed (rpm), extrusion length (mm), and layer height (mm). These parameters are defined in the G-code and are comparable to the processing variables of the conventional machining process. Once the recipe of the slurry is defined, the rheology properties of the slurry are fixed. The processing parameters are the actual parameters to be controlled and modified.

### 6.6.1 Extrusion Speed and Travel Speed

The processing variables are defined and stored as printing commands in G-code (RS-274) format. The travel speed is directly defined inside a single line of code, while the travel distance, extrusion distance, and extrusion speed can be calculated between neighboring lines. An example of the G-code is shown as follows:

```
N0001 G1 X24.496 Y-7 E26.3670 F1200  
N0002 G1 X24.496 Y7 E39.0921
```

In these two lines of G-code, a linear distance between the point (24.496, 7) and the point (24.496, -7) can be calculated by using the Pythagorean theorem, which is 14 mm in this case. F1200 specifies that the feed rate is 1200 mm/min (20 mm/s). These two parameters can be used to calculate the interval time as 0.7 s. The difference between the two E values is the length of the slurry extruded out of the nozzle between the interval time. The extrusion speed is calculated by the length of the extrusion and interval time. In this case, the extrusion speed is 1089.6 mm/min (18.16 mm/s), which is slower than the travel speed (1200 mm/min). These relations are expressed by equations (14–18):

$$D = \sqrt{(X_2 - X_1)^2 + (Y_2 - Y_1)^2} \quad (14)$$

$$L_E = (E_2 - E_1) \quad (15)$$

$$T_{Travel} = \frac{D}{Feedrate} \quad (16)$$

$$V_{Extrude} = \frac{L_E}{T_{Travel}} \quad (17)$$

$$M_{Extrude} = \frac{L_E}{D} \quad (18)$$

where  $D$  is the linear travel distance between the neighboring line of G-code;  $X_1, Y_1,$  and  $E_1$  are positions of the destination in the first line of code;  $X_2, Y_2,$  and  $E_2$  are positions of the destination in the second line of code;  $L_E$  is the length of extrusion;  $T_{Travel}$  is the interval time of travel;  $V_{Extrude}$  is the extrusion speed; and  $M_{Extrude}$  is the multiplier of the extrusion length over distance, which represents different travel and extrusion speed

combinations.

Twenty-seven copies of design pattern #1, as shown in Figure 29, were printed at different travel-extrusion speed combinations; the travel speed was fixed at 1200 mm/min based on the recommendation from the manufacturer. These 27 patterns were printed in a row, and 200 mm slurry was extruded from the nozzle at 1200 mm/min before printing the first pattern to ensure a constant flow during the print. The printed patterns were measured by noncontact, 3D, surface metrology confocal microscopy (Sensofar, Barcelona).









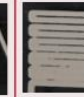
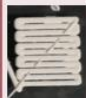


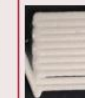







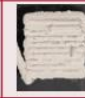






Extrusion speed(mm/min)	1200	1320	1440	1560	1680	1800	1920	2040	2160
Profile									
Extrusion speed(mm/min)	2400	2520	2640	2760	2880	3000	3120	3240	3360
Profile									
Extrusion speed(mm/min)	3600	3720	3840	3960	4080	4200	4320	4440	4560
Profile									

Figure 39 Samples printed at different extrusion speeds with a travel speed of 1200 mm/min

As shown in Figure 39, one data point for each track was collected; thus, 11 data points were collected for each pattern. The average height, width, length, and cross-sectional area of the printed filament were analyzed; the results are listed in Table 6. The volume of each path was also calculated by the average length and the cross-sectional area. With an increase in the extrusion speed, the height, width, length, and volume also increase. However, when the extrusion speed exceeded 2760 mm/min,  $M_{Extrude} = 2.3$ , and the two neighboring paths started to merge and overlap, which causes the measured width to become inaccurate. These experiments show that the optimal  $M_{Extrude}$  was between 1.2 and 1.7, which was

$$\frac{1440 \text{ mm/min}}{1200 \text{ mm/min}} \text{ and } \frac{2040 \text{ mm/min}}{1200 \text{ mm/min}}$$

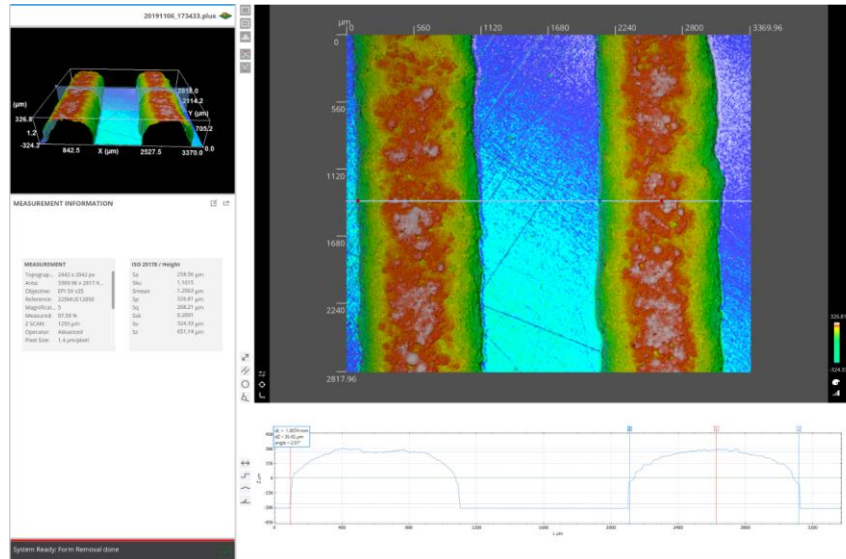


Figure 40 Printed filament measured by noncontact, 3D, surface metrology confocal microscopy

Table 6 Average height, width, length, cross-sectional area, and calculated volume of the printed filament

Travel speed (mm/min)	Extrusion speed (mm/min)	Height (mm)	Width (base) (mm)	Cross-sectional area (mm <sup>2</sup> )	Length (mm)	Volume (mm <sup>3</sup> )
1200	1200	0.6674	0.9136	0.3512	20.4409	7.1778
1200	1320	0.7023	0.8846	0.4610	20.4855	9.4442
1200	1440	0.5668	1.0074	0.5212	20.8475	10.8655
1200	1560	0.6091	1.0585	0.5512	21.1240	11.6431
1200	1680	0.5774	1.1868	0.6190	21.1222	13.0748
1200	1800	0.6058	1.2337	0.6657	20.9952	13.9756
1200	1920	0.6003	1.4035	0.7454	21.1175	15.7411
1200	2040	0.5582	1.5097	0.7861	21.5004	16.9016
1200	2160	0.5542	1.5649	0.8363	21.6249	18.0854
1200	2400	0.5973	1.6726	0.8642	21.4811	18.5641
1200	2520	0.6037	1.7140	0.8836	21.6954	19.1694
1200	2640	0.6484	1.7140	0.8247	21.9175	18.0750
1200	2760	0.6638	1.8906	1.0077	22.8479	23.0247
1200	2880	0.8084	1.4932	0.7228	21.7737	15.7381
1200	3000	0.7135	1.8409	0.9117	21.6647	19.7519
1200	3120	0.7117	1.6118	0.8272	21.8654	18.0869
1200	3240	0.7400	1.8920	1.0069	21.8875	22.0385
1200	3360	0.6951	1.8244	1.1220	22.2073	24.9176
1200	3600	1.1257	1.8078	0.9073	22.2267	20.1657
1200	3720	0.6555	1.9237	1.0540	23.2124	24.4663
1200	3840	0.7258	-	-	23.4535	
1200	3960	1.6885	-	-	23.8739	

1200	4080	0.8466	-	-	22.0064	
1200	4200	0.9101	-	-	22.3968	
1200	4320	1.4101	-	-	22.8509	
1200	4440	1.2723	-	-	24.8811	
1200	4560		-	-	25.8299	

## 6.7 Intermediate Parameters

The intermediate values contain the deformation (of the lower layer), deflection (of the higher layer), pressure (of the piston and nozzle), and shear rate (at the nozzle). These parameters can be treated as in-process measurements and feedback signals for the closed-loop control system.

### 6.7.1 Deformation and Deflection of the Printed Part

The deformation and deflection of the printed part are influenced by the deflection of the upper layer and deformation of the lower layer.

The upper layer's deflection has been investigated by the research team from the University of Illinois at Urbana-Champaign and Sandia National Laboratories. Lewis et al. discovered that the upper layer's deflection can be modeled as a simply supported beam with a distributed load, as shown in Figure 41 [79]. The maximum deflection ( $Z_{max}$ ) can be calculated based on the deflection formulas for the simply supported beam with a uniformly distributed load by equations (19–21):

$$Z_{max} = \frac{-5wl^4}{384EI} \quad (19)$$

$$w = \frac{1}{4} * \pi * D_{slurry}^2 * \rho_{slurry} * g \quad (20)$$

$$I = \frac{\pi * D_{slurry}^4}{64} \quad (21)$$

where  $w$  is the distributed load,  $E$  is Young's modulus,  $D_{slurry}$  is the diameter of the printed slurry,  $I$  is the moment of inertia, and  $g$  is the gravitational constant.

However, there are some limitations when using equations (19–21). The slurry must exhibit a well-controlled viscoelastic response, and the volume fraction must be high enough (greater than 50%) to resist compressive stresses that arise from capillary tension [79]. If the slurry has a low volume fraction or exhibits an elastic response, the surface tension will appear to influence the deflection and cannot be disregarded [85]. The slurry used in the robocasting process is a soft material; thus, the printed tracks cannot be merely treated as a beam. However, these equations can still be employed for approximation. More factors could be adopted to improve the accuracy of the deflection model.

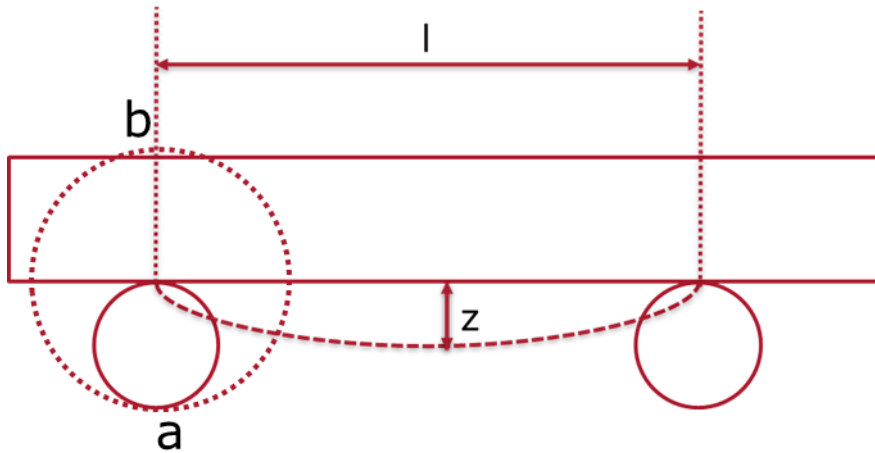


Figure 41 Schematic for the deflection ( $z$ ) of the upper layer.

The lower layer's deformation is influenced by viscosity, types of solution, load added to the lower layer, and Young's modulus. The following experiment was designed to test the height between point a and point b in Figure 41.

The printed design pattern #2 was measured by noncontact, 3D, surface metrology confocal microscopy (Sensofar, Barcelona). As shown in Figure 42, 11 data points were collected for each pattern. The mean and standard deviation for each pattern were analyzed and shown in Figure 43. The results show that with the increase in the layover time between the layers, the height from the top of the upper layer to the bottom of the lower layer will decrease.

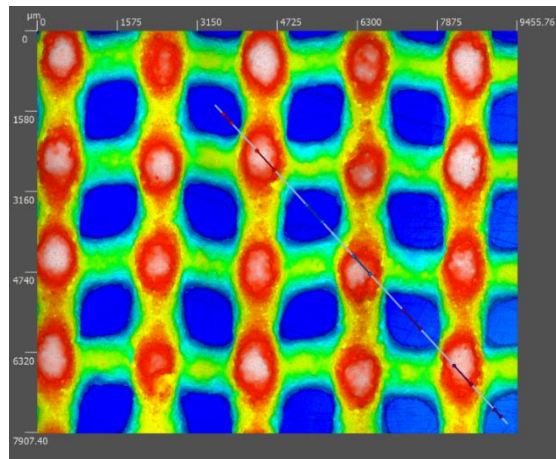


Figure 42 Sample measured by noncontact, 3D, surface metrology confocal microscopy

Table 7 Mean and standard deviation of height difference for different layover times

Time between layers (s)	Average height ( $\mu\text{m}$ )	Standard deviation ( $\mu\text{m}$ )
0	998.2827273	48.47541131
24	1057.918182	25.86293944
48	1066.309091	29.88690197

72	1065.809091	28.37500501
96	1082.063636	33.04252632
120	1099.672727	28.35814137
144	1121.081818	24.86020186
168	1107.7	26.64695105

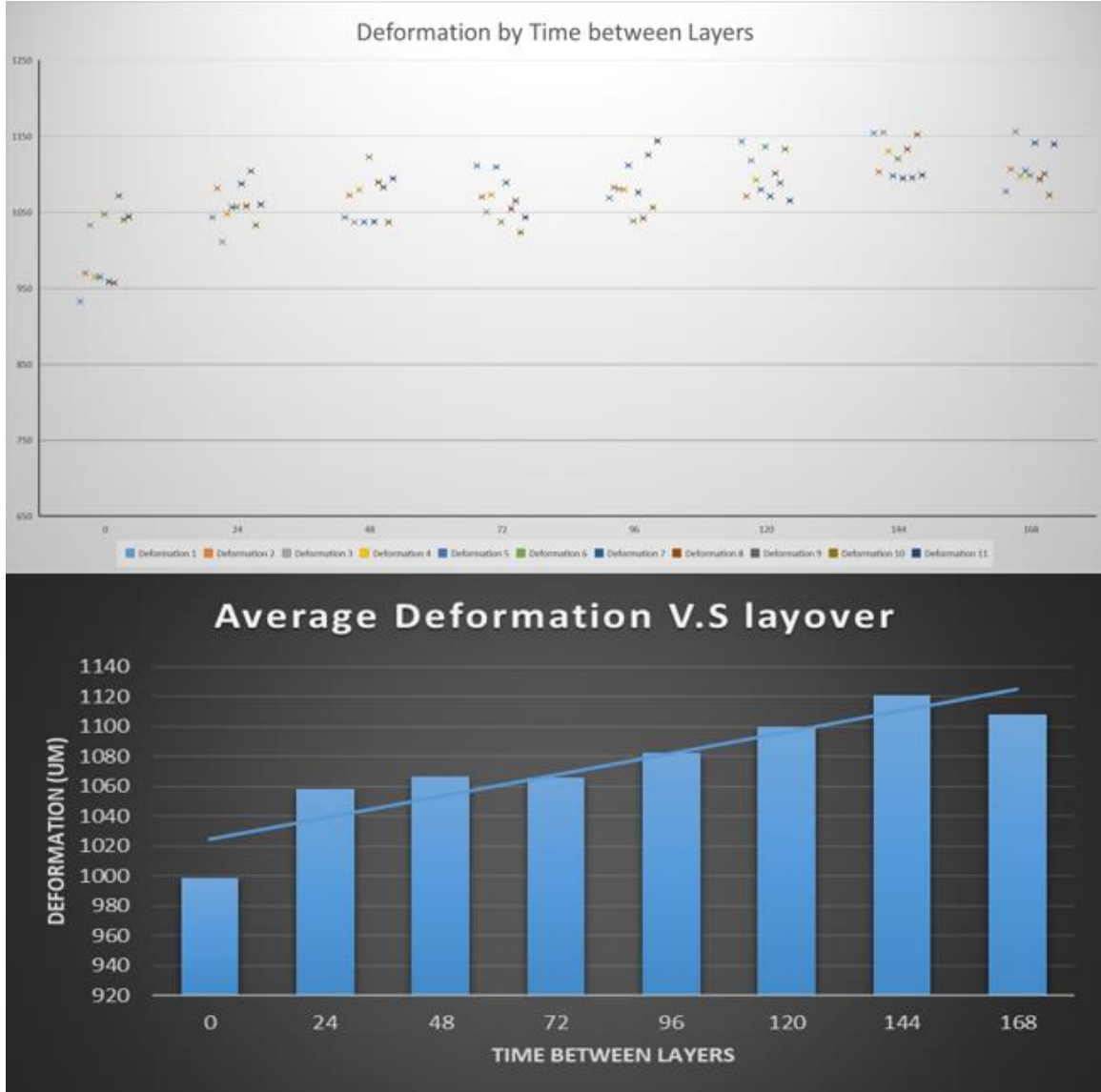


Figure 43 Height difference (um) vs. different layover times (s)

### 6.7.2 Dynamic Model of Extrusion Process

As shown in Figure 44, the pressure and shear rate during the printing process was described as a capillary extrusion model. The shear stress ( $\tau_w$ ), shear rate ( $\dot{\gamma}_w$ ), volumetric flow rate (Q), and pressure drop ( $\Delta P$ ) between the plunger and the nozzle can be calculated based on equations (22-28) [86-88]:

$$Q = \Delta V = \frac{V_s}{\beta} * \frac{dP_p}{dt} = V_{in} - V_{out} \quad (22)$$



$$P_p = \frac{\text{measured force}}{\pi * R_s^2} \quad (23)$$

$$V_{in} = d_s * \pi * R_s^2 \quad (24)$$

$$V_{out} = \pi * R_n^3 * n \left( \frac{-\tau_w}{m} \right)^{\frac{1}{n}} * (1 - \phi)^{\frac{n+1}{n}} * \left[ \frac{1-\phi^2}{3n+1} + \frac{2\phi*(1-\phi)}{2n+1} + \frac{\phi^2}{n+1} \right] \text{ for } \phi \leq 1$$

$$V_{out} = 0 \text{ for } \phi > 1 \quad (25)$$

$$\phi = \frac{\tau_y}{\tau_w} \quad (26)$$

$$\tau_w = \left( -\frac{P_o}{l_n} \right) * \frac{R_n}{2} \quad (27)$$

$$\Delta P = P_p - P_o = \left[ \frac{\Delta V}{\pi * R_s^3} * \left( \frac{3n+1}{n} \right)^n * \left( \frac{2(l_s) * K}{R_s} \right) \right] + \left[ \frac{\Delta V}{\pi * R_n^3} * \left( \frac{3n+1}{n} \right)^n * \left( \frac{2l_n * K}{R_n} \right) \right] \quad (28)$$

where  $l_s$  is the length of the syringe,  $l_n$  is the length of the nozzle,  $P_p$  is the pressure on the plunger,  $d_s$  is the plunger displacement,  $R_s$  is the radius of the plunger,  $R_n$  is the radius of the nozzle,  $n$  is the shear-thinning exponent,  $\tau_y$  is the yield stress in the Herschel–Bulkley fluid,  $K$  is the viscosity parameter in the Herschel–Bulkley fluid, and  $\beta$  is the bulk modulus of the slurry.

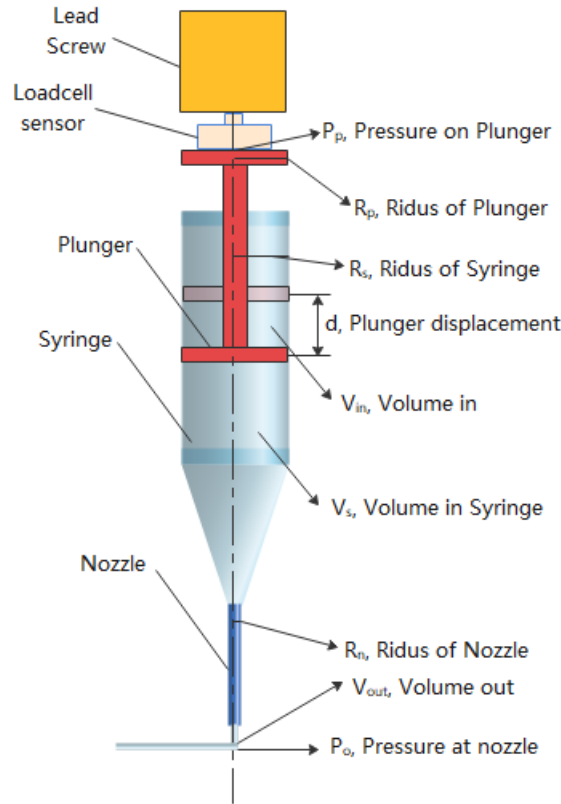


Figure 44 Schematic of the dynamic model of the extrusion process

## 6.8 Ceramic Robocasting Process Analyzed by the Axiomatic Design Theory

### 6.8.1 Current Decomposition

The current ceramic robocasting process was decomposed following a Cartesian theme into X, Y, and Z directions in the first level of the decomposition, as shown in the green background in Table 8. This decomposition theme is collectively exhaustive, covers all three Cartesian directions, and mutually exclusive (CEME) because they are orthogonal. The zeroth-level process variable (PV0) includes motions in the X, Y, and Z directions, and child process variables in the ceramic robocasting process were governed by the controller, such as a computer or a microcontroller.

Table 8 Current decomposition

Number	Functional Requirements	Number	Design Parameters	Number	Process Variables
<b>FR0</b>	<b>Print a ceramic part with small geometric bias comparing to the design</b>	<b>DP0</b>	<b>Parameters to produce a ceramic part with small geometric bias comparing to the design</b>	<b>PV0</b>	<b>Print on robocasting printer</b>
<b>FR1</b>	<b>Maintain the correct height of the product</b>	<b>DP1</b>	<b>Bias in the Z direction between the printed part and designed model</b>	<b>PV1</b>	<b>Extrude the slurry, Feed in the Z direction, Chose material</b>
FR1.1	Manage the change of height caused by dring mechanism of the printed signal layer	DP1.1	Evaporation shrinkage fraction/Extrusion and Table speed pair	PV1.1	Adjust the extrude speed, table speed, and viscosity
FR1.2	Manage the accumulated height of two neighbor layers	DP1.2	Influence of contact between layers	PV1.2	Print in the Z direction
FR1.2.1	Control the change of height caused by deflection of the upper layer due to gravity	DP1.2.1	Density of the slurry/gap between neighbor tracks/Inertia	PV1.2.1	Adjust the solvent volume percentage, gaping distance, and cross-section
FR1.2.2	Control the change of height caused by deformation of the lower layer	DP1.2.2	Mass of deposited upper track/Contact area, Viscosity of the slurry	PV1.2.2	Adjust the extrude speed, table speed/ nozzle geometry/ Chose the appropriate material recipe
FR1.2.3	Maintain the correct number of layers	DP1.2.3	Number of layers	PV1.2.3	Feed in Z direction
<b>FR2</b>	<b>Ensure the length of print is the same as the targeted model</b>	<b>DP2</b>	<b>Bias in the Y direction between the printed part and designed model</b>	<b>PV2</b>	<b>Extrude, Feed in Y direction, Chose material</b>
FR2.1	Control the change of length caused by plastic deformation for a printed single track	DP2.1	Extruded Volume/Cross-section are of the printed layer/Evaporation rate	PV2.1	Adjust the extrude speed, table speed, and viscosity
FR2.1.1	Control the change of length caused by dring for a printed single track	DP2.1.1	Evaporation fraction	PV2.1.1	Chose the appropriate material recipe (Volume percentage of Solvent)
FR2.1.2	Control the change of length caused by extrusion for a printed single track	DP2.1.2	Extruded Volume/Cross-section are of the printed layer	PV2.1.2	Move the printing platform in the Y direction
FR2.2	Control the change of length between layers	DP2.2	Shrinkage fraction	PV2.2	Control the density of slurry
FR2.2.1	Control the change of length caused by deflection of the upper layer due to gravity	DP2.2.1	Density of the slurry/gap between neighbor tracks/Inertia	PV2.2.1	Adjust the solvent volume percentage, gaping distance, and cross-section
FR2.2.2	Control the change of length caused by deformation of the lower layer	DP2.2.2	Mass of deposited upper track/Contact area, Viscosity of the slurry	PV2.2.2	Adjust the extrude speed, table speed/ nozzle geometry/ Chose the appropriate
FR2.3	Manage the influence of the necking and deflection	DP2.3	Gaping distance between tracks	PV2.3	Control the Infill percentage
<b>FR3</b>	<b>Ensure the width of print is the same as the targeted model</b>	<b>DP3</b>	<b>Bias in the X direction between printed part and designed model</b>	<b>PV3</b>	<b>Extrude the slurry, Feed in the X direction, Chose material</b>
FR3.1	Control the change of width caused by plastic deformation for a printed single track	DP3.1	Extruded Volume/Cross-section are of the printed layer/Evaporation fraction	PV3.1	Adjust the extrude speed, table speed, and viscosity
FR3.1.1	Control the change of width caused by dring for a printed single track	DP3.1.1	Evaporation fraction	PV3.1.1	Chose the appropriate material recipe (Volume percentage of Solvent)
FR3.1.2	Control the change of width caused by extrusion for a printed single track	DP3.1.2	Extruded Volume/Cross-section are of the printed layer	PV3.1.2	Move the printing platform in the Y direction
FR3.2	Control the change of width between layers	DP3.2	Shrinkage fraction	PV3.2	Control the density of slurry
FR3.2.1	Control the change of width caused by deflection of the upper layer due to gravity	DP3.2.1	Density of the slurry/gap between neighbor tracks/Inertia	PV3.2.1	Adjust the solvent volume percentage, gaping distance, and cross-section
FR3.2.2	Control the change of width caused by deformation of the lower layer	DP3.2.2	Mass of deposited upper track/Contact area, Viscosity of the slurry	PV3.2.2	Adjust the extrude speed, table speed/ nozzle geometry/ Chose the appropriate
FR3.3	Manage the influence of the necking and deflection	DP3.3	Gaping distance between tracks	PV3.3	Control the Infill percentage

### 6.8.2 Relations Among FRs, DPs, and PVs

In this study, functional requirements explain the functions to be accomplished, the design parameters represent the factors to fulfill the requirements, and the process variables are actual actions to modify the design parameters. As FR1, FR2, and FR3 require dimensional

accuracy in the Z, Y, and X directions, they share a similar decomposition structure. In this section, relations among the FRs, DPs, and PVs for the height direction (Z-direction) were explained and decomposed as an example for analyzing the whole ceramic robocasting process.

FR1 Maintain the correct height of the product

DP1 Bias in the Z direction between the printed part and the designed model

PV1 Extrude the slurry/ feed in the Z direction/ choose the material

To maintain the correct height of the product, the height difference ( $\Delta Z$ ) between the printed parts and the designed model should be measured and minimized. The governing equation for  $\Delta Z$  height difference was expressed by Equation (29):

$$\Delta Z = \Delta Z_{Layer} + \Delta Z_{Interaction} \quad (29)$$

where  $\Delta Z_{Layer}$  is the bias of each printed layer, and  $\Delta Z_{Interaction}$  is the bias caused by the interaction between the layers. Both the property of the material and the motions in the Z direction contribute to the height difference. The overall decomposition for this FR is based on this principle. The assigned metrics for FR1, DP1, PV1, and their children are shown in Table 9.

Table 9 Assigned metrics for FR1, DP1, PV1 and their children

Number	Functional Requirements	Measurement	Number	Design Parameters	Measurement	Number	Process Variables	Measurement
FR0	Print a ceramic part with small geometric bias comparing to the design	Tolerance in X,Y, Z direction	DP0	Parameters to produce a ceramic part with small geometric bias comparing to the design	measure bias in X,Y,Z direction of the as printed part	PV0	Print on robocasting printer	Material(solvent, solution), processes(feed, speed, extrusion)
FR1	Maintain the correct height of the product	Tolerance in Z direction	DP1	Bias in the Z direction between the printed part and designed model	Min(Printed height-Designed height)	PV1	Extrude the slurry, Feed in the Z direction, Chose material	Material(solvent, solution), processes(feed, speed, extrusion)
FR1.1	Manage the change of height caused by dring mechanism of the printed signal layer	Printed Layer height-Designed Layer height	DP1.1	Evaporation shrinkage fraction/Extrusion and Table speed pair	Mass before the evaporation- Mass after the evaporation	PV1.1	Adjust the extrude speed, table speed, and viscosity	Solvent type, volume percentage, print volume table speed
FR1.2	Manage the accumulated height of two neighbor layers	Accumulate of the printed two neighbor layers- Accumulate height of the designed two neighbor layers	DP1.2	Influence of contact between layers	Accumulate of the printed two neighbor layers	PV1.2	Print in the Z direction	Motions in Z direction
FR1.2.1	Control the change of height caused by deflection of the upper layer due to gravity	Height of the upper layer	DP1.2.1	Density of the slurry/gap between neighbor tracks/Inertia	Density/gap between nerbor tracks/Inertia	PV1.2.1	Adjust the solvent volume percentage, gaping distance, and cross-section	Solvent type, solution type,volume percentage, distance between tracks, cross-section geometry
FR1.2.2	Control the change of height caused by deformation of the lower layer	Height of the lower layer*	DP1.2.2	Mass of deposited upper track/Contact area, Viscosity of the slurry	Mass/Contact area/Viscosity	PV1.2.2	Adjust the extrude speed, table speed/ nozzle geometry/ Chose the appropriate material	Solvent type, solution type,volume percentage, cross-section geometry
FR1.2.3	Maintain the correct number of layers	Total Height/Designed layer height	DP1.2.3	Number of layers	Total Height/(Printed two layer height)*2	PV1.2.3	Feed in Z direction	Z travel

FR1.1 Manage the change in height caused by plastic deformation of the printed signal layer

DP1.1 Evaporation shrinkage fraction/extrusion-travel speed pair

PV1.1 Adjust the extrusion speed/ table speed/ and viscosity

Ceramic robocasting is an additive manufacturing method that builds the product layer by layer. For each layer, there naturally exists a designed height and an as-printed height. The

difference between the printed layer and the design layer ( $\Delta Z_{Layer}$ ) is caused by the drying mechanism and rheological property of the prepared slurry. The solvent content (PV) for each printed track will dry out, which causes deformation of the height and shape of each printed track. The extrusion-travel speed pair also influences the deformation of the width, height, and cross-sectional shape of the printed single layer. As the extrusion speed increases, the height, width, length, and volume also increase. A detailed study was presented in chapter 6.6.1.

Aside from the extrusion speed, the material property of the slurry has an impact on the height of the printed layer. The raw material used in the ceramic robocasting process was ceramic slurry, which was produced by combining solvent, solute, and thickening agent. The viscosity of the slurry influences the shape of the printed track. To manage the change in height caused by the plastic deformation of the printed signal layer (FR), a proper evaporation percentage (DP) should be ensured. It should be noted that, currently, there are two choices for DP1.1: 1) evaporation shrinkage fraction and 2) extrusion-travel speed pair. For a good design, only one DP should be used to fulfill a certain FR, and this DP should be produced by a single PV. If there are multiple choices of DP to fulfill an FR, only one DP should be a variable, while the other DPs should be constrained or set as constants. The material properties for a specific printing operation can be treated as a constant; however, they are variables for the whole robocasting system. The current robocasting process's material properties cannot be constrained or set as constants, which leads to a single FR being fulfilled by two DPs, and consequently, produces couplings in the system. These couplings are discussed in section 6.8.4.

FR1.2      Manage the accumulated height of two neighboring layers

DP1.2      Influence of contact between layers

PV1.2      Print in the Z direction

When an upper layer was deposited onto a lower layer, two neighboring layers interacted to produce deviations in the height direction ( $\Delta Z_{Interaction}$ ). These deviations are derived from both the upper layer and the lower layers; so FR1.2 can be decomposed into two children-level functional requirements accordingly.

FR1.2.1      Control the change in height caused by the deflection of the upper layer due to gravity

DP1.2.1      Density of the slurry/gap between neighboring tracks/inertia

PV1.2.1      Adjust the solvent volume percentage/gaping distance and cross-section

The upper layer's deflection has been investigated by the research team from the University of Illinois at Urbana-Champaign and Sandia National Laboratories. Lewis et al. discovered that

the deflection of the upper layer can be modeled as a simply supported beam with a distributed load, as shown in Figure 41.

The maximum deflection ( $Z_{max}$ ) was calculated based on the deflection formulas for the simply supported beam with a uniformly distributed load, as shown in chapter 6.2.1.

In this case, the functional requirement to control the change in height caused by the deflection of the upper layer due to gravity was fulfilled by three separate design parameters, and each design parameter was produced by its process variables.

FR1.2.2 Control the change in height caused by the deformation of the lower layer

DP1.2.2 Mass of the deposited upper track/contact area/viscosity of the slurry

PV1.2.2 Adjust the extrusion speed/ travel speed/nozzle geometry/ and choose an appropriate material recipe

The lower layer's deformation has a similar mechanism as the plastic deformation of the single track without deformation, as explained in FR1.1. However, the mass added to the lower layer, which accelerates the deformation of the lower layer also needs to be considered.

FR1.2.3 Maintain the correct number of layers

DP1.2.3 Number of layers

PV1.2.3 Feed in the Z direction

The number of layers influences the overall height of the printed part. When the height of each layer and the accumulated height of the neighbor layers change, the number should be adjusted. The governing equation for the number change in layers can be expressed by Equation (30):

$$N_{new\ Layer} = N_{Designed\ Layer} + \Delta N_{Layer} + \Delta N_{Interaction} \quad (30)$$

where  $N_{new\ Layer}$  is the number of layers to maintain the correct height of the printed part,  $N_{Designed\ Layer}$  is the number of layers from the original design,  $\Delta N_{Layer}$  is the adjusted number of layers caused by the change in height of each layer, and  $\Delta N_{Interaction}$  is the adjusted number of layers caused by the change in height between layers.

FR2 Ensure that the length of print is the same as the targeted model

DP2 Bias in the Y direction between the printed part and the designed model

PV2 Extrude the slurry/ feed in the Y direction/ and choose the material

FR3 Ensure that the width of print is the same as the targeted model

DP3 Bias in the X direction between the printed part and the designed model

PV3 Extrude the slurry/ feed in the X direction/ choose the material

FR2 and FR3 were analyzed by a similar approach. The factors that influence the length

difference ( $\Delta L$ ) and the width difference ( $\Delta W$ ) are expressed by equation (31) and equation (32), respectively:

$$\Delta L = \Delta L_{Layer} + \Delta L_{Interaction} \quad (31)$$

$$\Delta W = \Delta W_{Layer} + \Delta W_{Interaction} \quad (32)$$

where  $\Delta L_{Layer}$  and  $\Delta W_{Layer}$  are the bias of each printed layer in length and width, and  $\Delta L_{Interaction}$  and  $\Delta W_{Interaction}$  are caused by the interaction between the layers. The detailed decomposition also follows a similar approach to the decomposition in the height (Z) direction.

### 6.8.3 Design Matrix

The FR-DP design matrix was generated by Acclaro DFSSV software, as shown in Figure 45. A detailed analysis of the matrices is provided in section 6.8.4.

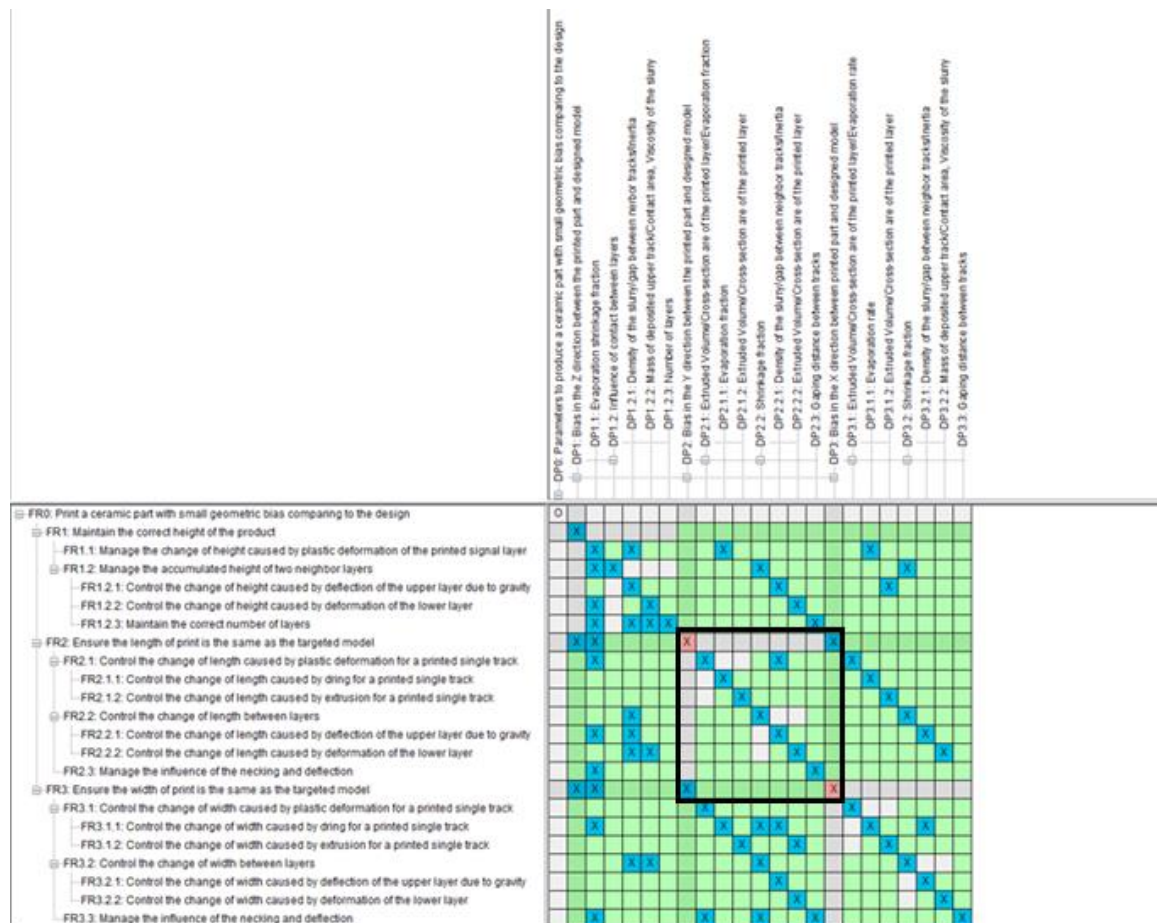


Figure 45 FR-DP design matrix

### 6.8.4 Coupling

Suh et al. mentioned that the FR-DP matrix could help researchers analyze the design. If the FR-DP matrix is diagonal, the design is uncoupled. If the matrix can be listed as or

converted to a lower triangular matrix, the design is decoupled. If the matrix does not exhibit either a diagonal shape or a lower triangular shape, the design is coupled [59]. As Axiom I requires the maintenance of independence, an uncoupled design is always more desirable than a decoupled design, while a coupled design should be avoided. The current ceramic robocasting process is a coupled design, as shown in Figure 45, which is a violation of Axiom I.

There are several off-diagonal interactions in the right upper triangle of the current FR-DP matrix, as shown in Figure 45. There are two types of interactions among these couples. An example of each type is analyzed in this chapter.

#### **6.8.4.1 FR-DP Coupling Produced by Material Properties**

FR1.1      Manage the change in height caused by the drying mechanism of the printed signal layer

DP1.2.1    Density of the slurry/gap between neighbor tracks and inertia

As explained in chapter 6.8.2, FR1.1 is influenced by both the evaporation shrinkage fraction and the extrusion-travel speed pair. DP 1.2.1, the density of the slurry, and the gap between neighboring tracks and inertia are designed to control the change in height caused by the deflection of the upper layer due to gravity. The slurry density and evaporation shrinkage fraction are both influenced by the choice of solvent and its volume percentage. Thus, they are naturally coupled with each other.

#### **6.8.4.2 FR-DP Coupling for Redundant Control of the Different Directions of Print**

FR2.1.2    Control the change in length caused by extrusion for a printed single track

DP3.1.2    Extruded volume/cross-sectional area of the printed layer/evaporation fraction

DP3.1.2 fulfills FR3.1.2, which requires maintaining the change in width caused by extrusion for a printed single track. FR2.1.2 shares the same equation as FR3.1.2, and the only difference is that FR2.1.2 is for the change in length, resulting in these two FRs sharing the same design requirement and being redundant to each other.

#### **6.8.4.3 Discussion on DP-PV Coupling**

Different from the well-studied FR-DP matrix and coupling, the DP-PV matrix and couplings have rarely been mentioned by researchers. In this study, the method for analyzing the FR-DP matrix was adopted to explain the couplings and interactions in the DP-PV matrix. If DP-PV is diagonal, then the manufacturing process is uncoupled. If the matrix can be listed

or converted into a lower triangular shape, the manufacturing process is decoupled. Any other forms of the matrix will contribute to a coupled process. In the current design of the ceramic robocasting process, the DP-PV matrix shows a heavily coupled pattern, which is because the material property of the slurry for the whole system is a variable. Simultaneously, the design parameters are fulfilled by the correct material property. Thus, these properties are correlated. An example is listed as follows:

DP1.1          Evaporation shrinkage fraction/extrusion-travel speed pair

PV2.2.1        Density of the slurry/gap between neighboring tracks and inertia

DP1.1 is used to manage the change in height caused by the drying mechanism of the printed single layer. FR1.1 can be fulfilled by adjusting the solvent type, volume percentage, print volume, and travel speed, which was expressed in PV1.1. When the solvent type and volume percentage are changed, the slurry density is also changed, resulting in the coupling of DP1.1 and PV2.2.1.

### 6.8.5 Axiom II: Minimize the Information Content of the Design

Axiom II of the Axiomatic design theory requires the minimization of the information content. Each FR-DP pair is regarded as a one-dimensional solution space. Suh mentioned that Axiom II should be applied to a system or design that satisfied Axiom I [59]. The whole system/design is a combination of multiple solution spaces, and the probability of success is calculated based on equations (33–34) [67]:

$$I = \ln \left( \frac{1}{p} \right) \quad (33)$$

$$P = \frac{1}{e^I} \quad (34)$$

where I represents the information contents; in this case, I is equal to the FR-DP pairs, while P is the probability of success. The number of FR-DP pairs, I, should be minimized to increase the probability of success. The current ceramic robocasting process does not satisfy Axiom I, however, equations (33) and (34) can still be applied to express the correct change in the probability of success by the trend.

### 6.8.6 Physical Integration

The physical integration matrixes are shown in Figure 46. The DPs were decomposed into each level to analyze their interrelationships.



		DP0	DP1	DP1.1	DP1.2	DP1.2.1	DP1.2.2	DP1.2.3	DP2	DP2.1	DP2.1.1	DP2.1.2	DP2.2	DP2.2.1	DP2.2.2	DP2.3	DP3	DP3.1	DP3.1.1	DP3.1.2	DP3.2	DP3.2.1	DP3.2.2	DP3.3	
DP0	Parameters to produce a ceramic part with small geometric bias comparing to the design	-																							
DP1	Bias in the Z direction between the printed part and designed model		-						X								X								
DP1.1	Evaporation shrinkage fraction/Extrusion and Table speed pair			-		X	X			X	X	X	X	X	X			X	X	X	X	X	X	X	
DP1.2	Influence of contact between layers				-								X	X							X	X			
DP1.2.1	Density of the slurry/gap between neighbor tracks/inertia			X		-							X		X						X	X		X	
DP1.2.2	Mass of deposited upper track/Contact area, Viscosity of the slurry			X			-																		
DP1.2.3	Number of layers							-																	
DP2	Bias in the Y direction between the printed part and designed model		X						-								X								
DP2.1	Extruded Volume/Cross-section are of the printed layer/Evaporation fraction			X						-								X							
DP2.1.1	Evaporation fraction			X							-		X	X				X	X				X	X	
DP2.1.2	Extruded Volume/Cross-section are of the printed layer			X								-	X		X			X		X	X		X	X	
DP2.2	Shrinkage fraction			X	X	X					X	X	-								X				
DP2.2.1	Density of the slurry/gap between neighbor tracks/inertia			X	X						X			-							X	X			
DP2.2.2	Mass of deposited upper track/Contact area, Viscosity of the slurry			X		X					X					-					X		X		
DP2.3	Gaping distance between tracks			X													-								
DP3	Bias in the X direction between printed part and designed model		X						X									-							
DP3.1	Extruded Volume/Cross-section are of the printed layer/Evaporation fraction			X						X	X	X							-						
DP3.1.1	Evaporation fraction			X						X										-		X	X		
DP3.1.2	Extruded Volume/Cross-section are of the printed layer			X							X										-	X		X	
DP3.2	Shrinkage fraction			X	X	X					X	X	X	X				X	X		-				
DP3.2.1	Density of the slurry/gap between neighbor tracks/inertia			X	X						X							X				-			
DP3.2.2	Mass of deposited upper track/Contact area, Viscosity of the slurry			X		X					X	X				X					X			-	
DP3.3	Gaping distance between tracks																								-

Figure 46 DP-DP interactions for the current robocasting process

The physical integration matrix is different from the FR-DP matrix in section 6.8.3. In this specific case, the lower triangle (in the yellow background) and upper triangle (in the pink background) of the DP-DP matrix are symmetrical about the diagonal. This fully coupled DP-DP relationship in the current robocasting process occurs because most of the actions to print the part are operated by the same printer, and these actions physically interact with each other.

### 6.8.7 Discussion

The material properties in the current decomposition of the ceramic robocasting process were treated as process variables, which leads to the contradiction with the AD theory and heavily coupled FR-DP and DP-PV matrices. The deflection model in this study was based on adapting the deflection equation for the simply supported beam [79]. To properly apply the beam deflection equation, the material of the beam should obey Hooke's law [89]. However, the ceramic slurry used in the robocasting process is a soft material; hence, the printed filament cannot be merely treated as a beam. The beam deflection equations can be utilized for approximation, but more factors should be adopted to accurately represent the deflection model.

The deformation of the printed pattern in the length and width shares a similar mathematic model, which leads to coupling. A new nozzle, printing mechanism, or printing strategy needs to be developed to increase the probability of success as they can separate the coupled process. Thus, Axiom I will also be fulfilled, as it requires maintaining the independence of the FRs.

Another possible approach to decoupling the current manufacturing process is to introduce

constraints to limit the material properties. This approach can be achieved by integrating closed-loop control into the current system and setting up a database that describes the relations between the material properties and the process variables. For example, when attempting to control the deflection of the upper layer of the print, the material property can be treated as a constant if introducing a deflection-extrusion closed-loop control. Current material properties are converted from variables into constants, and deflection is only a function of the shape of the nozzle. This approach can turn the current coupled design into a decoupled design as the current ceramic robocasting process is a coupled system, which leads to a complex physical model.

The conventional closed-loop strategy, such as PID control, requires careful conversion to govern operations. However, the ANN, which is a data-driven decision-making approach, provides a chance to bypass the complex dynamic physics equations and map the real-time status into control actions by experience, which is a proper control logic for governing the coupled robocasting operation.

This study decomposed the current ceramic robocasting manufacturing process based on the motions in the Cartesian coordinates. For this process, it can also be decomposed based on the deformation mechanism. A further study can be carried out to compare the possible similarities and differences between two kinds of decompositions for the same ceramic robocasting manufacturing process.

### **6.8.8 Concluding Remarks**

This study shows an approach for analyzing the current ceramic robocasting process via the application of AD theory. FR-DP and DP-PV matrices and decompositions were demonstrated. The relationships among FR-DP-PV were analyzed. Possible solutions for optimizing the current ceramic robocasting manufacturing process by integrating closed-loop control were discussed. Future work includes applying the proposed change in the robocasting printer to decouple the motion of three directions and create a material properties database.

## 6.9 Improving Ceramic Additive Manufacturing by Machine Learning Enabled Closed-Loop Control

### 6.9.1 Design of the Control Loop

An in-process machine learning enabled closed-loop control process flow is demonstrated in Figure 47. The process flow is divided into two stages. The first stage is designed to acquire data and generate control logic, in this study, an artificial neural network model. The second stage is designed for the printing process that fabricates the design pattern. A MATLAB script was developed to enable communication among a 3D printer, loadcell sensor, ANN model, and computer through RS-232 standard serial port. The operational G-code is loaded, analyzed, and sent to the printer in line-by-line form.

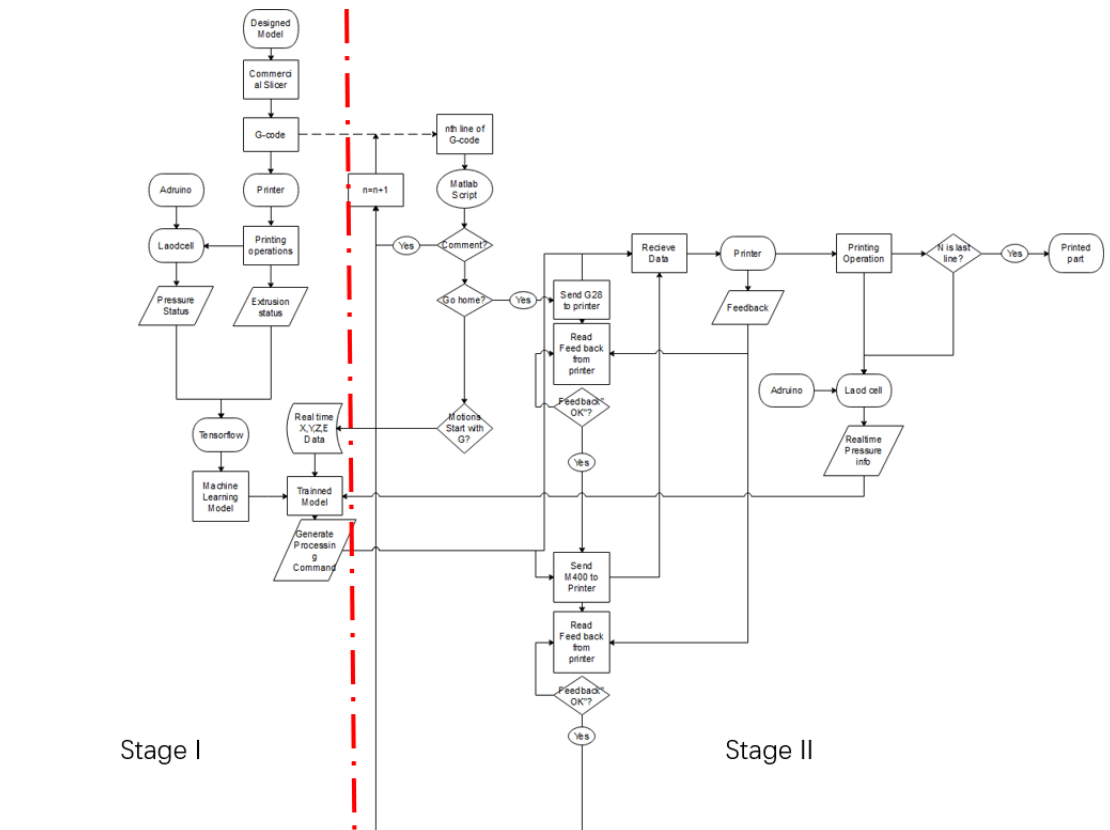


Figure 47 Flow diagram of ANN closed-control loop

In the first stage, an ANN model was created to generate the prediction-based process parameter. The ANN was developed in TensorFlow (Google Brain, CA) based on the collected location, pressure, geometric, and time-series information of each data point. The pattern used in this research is design pattern #3. Since the length of each track and travel speed had been constrained to 20 mm and 1200 mm/min, the relationship between  $L_E$  and  $M_{Extrude}$  were

calculated by Equation (18) and expressed in Table 10.

Table 10 Relationship between  $M_{Extrude}$  and  $L_E$  in this study

$M_{Extrude}$	1.0	1.1	1.2	1.3	1.4	1.5	1.6	1.7	1.8	1.9
$L_E$ (mm)	20	22	24	26	28	30	32	34	36	38

The conclusion from chapter 6.6.1 stated that the optimal  $M_{Extrude}$  was between 1.2 and 1.7. Thus, the processing pressure and dimensional information for ten sets of the designed pattern were collected for ANN model training and testing. The  $M_{Extrude}$  for these ten sets of prints ranged from 1.0 to 1.9, with an increment of 0.1. An example of the data collected for training the artificial neural network model is shown in Table 11. As shown in Figure 31, the starting loadcell reading in the table represents the real-time load that is added to the plunger at a certain extruding point, while the ending loadcell reading represents the load at the next extruding point. The difference between these two readings represents the change in pressure that corresponds to the extrusion operation. As the loadcell sensor was directly attached to the plunger of the syringe, the pressure added to the ceramic slurry was proportional to the load applied to the plunger. The relationship among the loadcell reading(g), process pressure (Pa), gravitational acceleration and area of the plunger ( $m^2$ ) is expressed in equation (35):

$$P = \frac{\text{Loadcell reading} * g}{\text{area of plunger} * 1000} \quad (35)$$

The extrusion in Table 11 represents the length of extruding  $L_E$  in equation (15) between two neighboring extrusion points. The starting loadcell reading, ending loadcell reading, and extrusion were collected to train the ANN model for predicting the desired extruding distance. In the model training stage, the starting loadcell reading and ending loadcell reading were inputs, and the extrusion was the output. Since process variables were pre-defined in the G-code in this stage, the collected in-process pressure information and dimensional information were treated as the uncontrolled group information.

Table 11 Example of data collected for training and testing the extruding length prediction ANN model

Data ID	Starting loadcell reading (g)	Ending loadcell reading (g)	Loadcell reading difference (g)	Extrusion (mm)
1	4712	4819	107	26
2	8562	8621	59	30
3	8097	8478	381	30

4	4814	4838	24	26
5	4743	4825	82	26
6	4671	4814	143	26
7	4946	4982	36	26
8	4627	4810	183	26
9	4832	4877	45	26

In the second stage, an executable real-time G-code was generated by the MATLAB script based on a given pre-defined G-code, real-time sensor reading information, targeted sensor reading, and pre-trained ANN model. Since the designed pattern's physical location and dimensions were constrained, the extrusion length for each extruding point, the E value, acted as the variable in the generated G-code and was predicted. The variable real-time G-code was generated and sent to the robocasting printer in a line-by-line order. Each line of G-code was followed by an inquiry command—in this study, “M400”—to track the robocasting printer's current movement status. As the robocasting printer used in this study is loaded with Smoothieware firmware, an “OK” echo would be replied to the “M400” command only when the printer finished its motion and attained idling status [90]. Thus, a full sequence of inquiry “M400” followed by an “OK” response was treated as a signal for generating a new line of G-code. The desired length of extrusion was predicted by inputting the in-process pressure and targeted pressure into the pre-trained artificial neural network model. Since process variables were governed by the ANN model in the second stage, the collected in-process pressure information and dimensional information were treated as controlled group information.

A pre-pressure function was also integrated into the MATLAB script before printing the first designed model in the controlled group. The pre-pressure function increases the pressure before printing the designed model to improve the closed-loop control performance and protects the robocasting system. If the difference between the two inputs of the ANN model is extremely large, such as when the current loadcell reading is 0 while the target loadcell reading is 5000 g, the predicted extrusion could also be extremely large. As specified in the introduction, the extrusion motion is converted by the rotation motion of the motor. An extremely large extrusion may cause the motor to exceed its maximum rotating speed. The current pre-pressure function was defined to extrude the ceramic slurry at 1200 mm/min until the in-process loadcell reading reaches 90% of the target loadcell reading.

### 6.9.2 Profile of Printed Patterns for the Uncontrolled Group

The geometric profile of printed patterns was measured by non-contact confocal microscopy (Sensofar, Barcelona) and analyzed by MountainsMap software (Digital Surf, France). The time interval between the finished printing and the measurement was 24 hours. Thus, the geometric information of each extruding point was obtained.

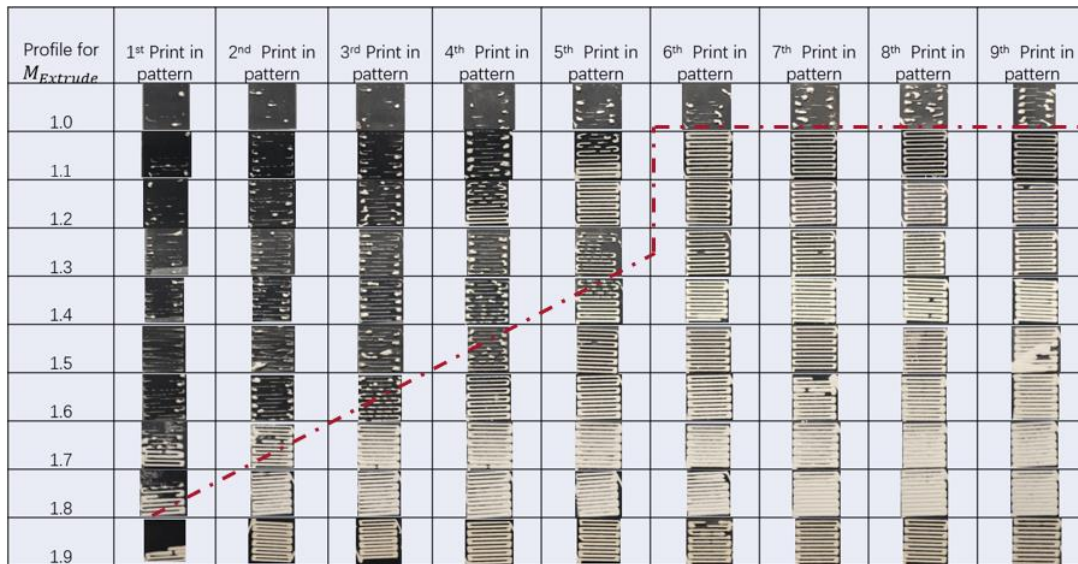


Figure 48 Profiles for the printed pattern with  $M_{Extrude}$  ranging from 1.0 to 1.9

The profiles overview for the uncontrolled groups is shown in Figure 48. Printed profiles above the red line exhibit a worse quality than those below the red line. To explain this phenomenon, the loadcell reading history for groups with  $M_{Extrude}$  equal to 1.0, 1.4, and 1.8 were analyzed, as shown in Figure 49. Based on Table 10, the  $M_{Extrude}$  1.0 group had an extrusion length of 20 mm, and the  $M_{Extrude}$  1.4 group had an extrusion length of 28 mm, while the  $M_{Extrude}$  1.8 group had an extrusion length of 36 mm. These three groups were reasonable examples of the extrusion process with low extrusion, medium extrusion, and high extrusion. The loadcell reading history in Figure 10 a) shows that the printing process can be divided into three stages. As the dimension of the printed pattern, travel speed, and sampling rate of the loadcell were pre-defined, the total interval time to print the whole pattern was 129.6 s, whereas the time interval for each model was 14.4 s. In the first stage, the sensor reading increases at a fast rate. Depending on Equation (35), when the shear stress is smaller than the slurry's yield stress, the volume flow out of the nozzle is zero. The pressure continues to accumulate until it reaches a point where the shear stress becomes greater than the yield stress. Equations (35) and (36) show that  $\frac{dP_p}{dt}$ , which is the plunger pressure change rate, is proportional to the extrusion rate. The first model in the 1.0, 1.4, and 1.8 groups belong to this

stage.

In the second stage, the sensor reading increment rate starts to decrease compared with that in the first stage. From the second stage on, the slurry starts to form a continuous flow out of the nozzle. The profile of the printed model in this stage contains a pattern transformation from dash-like to continuous. The 2<sup>nd</sup> to 9<sup>th</sup> printed models in the 1.0 group and the 2<sup>nd</sup> to 5<sup>th</sup> printed models in the 1.4 group belong to this stage.

In the third stage, the sensor reading becomes relatively stable compared with the first and second stages. As the slurry exhibits a shear-thinning property, that the increase of pressure will decrease the viscosity, further increase the slurry extrusion speed. The increase in extrusion speed will then increase the volume flow of the slurry, which further decreases the processing pressure. This process continues until a dynamic equilibrium point is reached, which can be expressed as Equations (36–37):

$$\frac{dP_p}{dt} = 0 \quad (36)$$

$$\Delta V = \frac{V_s}{\beta} * \frac{dP_p}{dt} = V_{in} - V_{out} = 0 \quad (37)$$

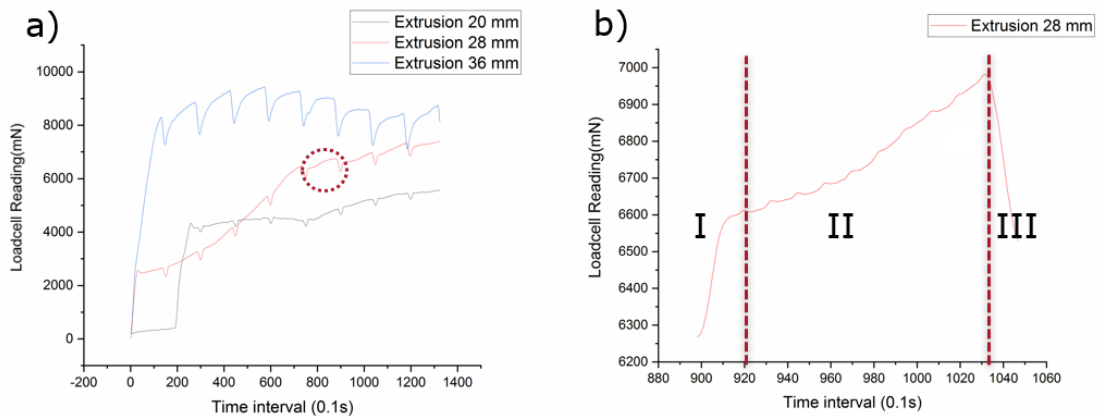


Figure 49 a) Loadcell reading history for extrusion length of 20 mm, 28 mm, and 36 mm groups and b) 6<sup>th</sup> model on the extrusion length of 28 mm group

The sensor reading history of the 6<sup>th</sup> model on the extrusion length of 28 mm group is shown in Figure 49 b). The first model in the stable stage of the 28 mm group was randomly selected as an example of the stable printing stage. The printing process for each stable printed model can be divided into three stages. As each model's interval time was 14.4 s and the loadcell had a sampling rate of 10 Hz, the loadcell history curve for each model contained 144 data points, of which 132 points were obtained from the designed model. Stages I and II represented the actual data points from the model. Stage I represented the data points of the

first two tracks of the model, and stage II contained data points from track three to track eleven of the designed model. The remaining 12 points were obtained from the rapid travel motion between the two neighboring models, which are labeled as Stage III in Figure 49 b). Since the rapid motion only moved the nozzle location but did not extrude any slurry, the loadcell reading decreased, resulting in the rapid increase rate of the sensor reading in stage I.

This study only focused on the stable stage of the print. To ensure the same number of data points derived from each uncontrolled group, the data of the 6<sup>th</sup> model to the 9<sup>th</sup> model for each printed group was collected to generate the ANN model. The  $M_{Extrude}$  1.0 group did not have any stable model that belongs to the stable stage; thus, data from this group were excluded from the ANN model.

### 6.9.3 Pressure Control by ANN

A total of 376 sets of data were collected and normalized for training the ANN prediction model; 80% of the data were categorized as training sets; and the remainder of the data were categorized as test sets to verify the accuracy of the trained model. The structure of the data set is shown in Table 11. The ANN's layer structure was set to have two hidden layers, and each layer had 64 nodes. The starting loadcell reading and ending loadcell reading were inputs for training the artificial neural network model, and the length of extrusion was the output. A detailed explanation is provided in chapter 6.9.1. A summary of the model is shown in Figure 50:

Layer (type)	Output Shape	Param #
dense (Dense)	(None, 64)	192
dense_1 (Dense)	(None, 64)	4160
dense_2 (Dense)	(None, 1)	65
Total params: 4,417		
Trainable params: 4,417		
Non-trainable params: 0		

Figure 50 Summary of the ANN model for extrusion length prediction

As stated in the literature review chapter, many different activation functions are available for training the ANN method. Figure 51 shows the absolute error of the training sets by using four most frequently used activation functions. As shown in Figure 51, a) is the training set



error for the ReLU activation function, b) is the training set error for the Tanh activation function, c) is the training set error for the Sigmoid activation function, and d) is the training set error for the Softplus activation function. An error distribution of these four activation functions is shown in Table 12. The error is the absolute error defined as the difference between the predicted length of extrusion and the actual length of extrusion. The predicted length of extrusion was generated by the trained ANN model, while the actual length of extrusion was the data collected from each group in Figure 48. The absolute error from the training sets and test sets were included in Table 12. In the current circumstance, the ReLU function exhibits the most concentrated error distribution compared with other functions, and the majority of the errors are within a range of  $\pm 2$  mm. The ReLU function was chosen to carry out the research because it had the smallest error range among the four activation functions.

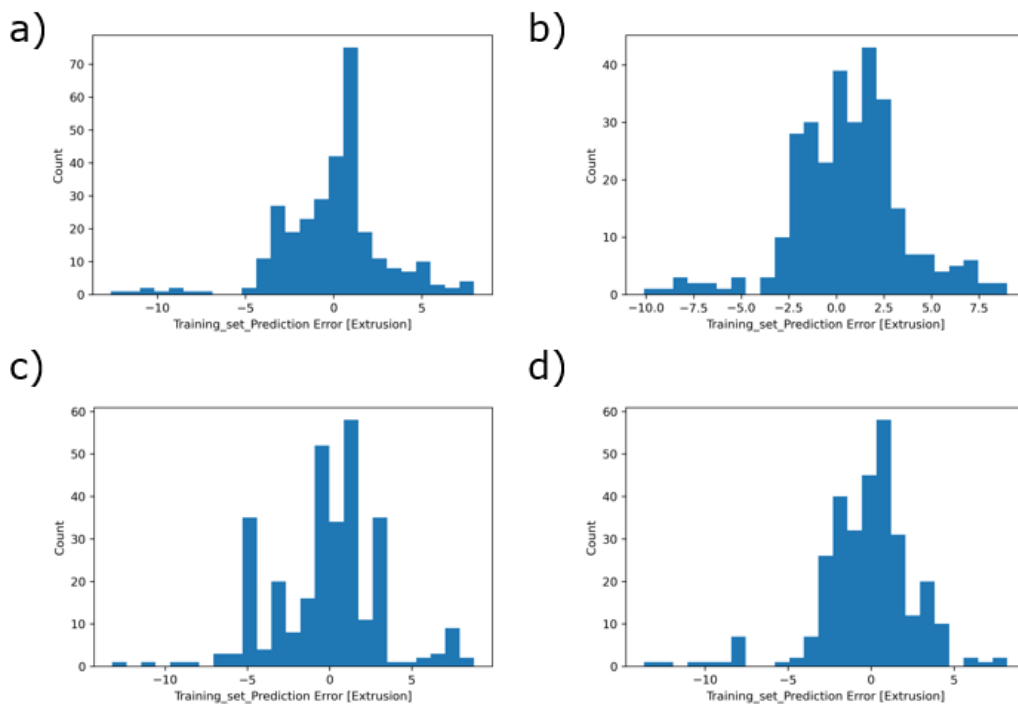


Figure 51 Absolute error (mm) of the training set by using different activation functions:  
a) ReLU, b)Tanh, c)Sigmoid, and D)Softplus

Table 12 Statistics of the error distribution of these four activation functions

Bin Center	Bin End	Relative Frequency %	Relative Frequency %	Relative Frequency %	Relative Frequency %
Frequency Counts	Frequency Counts	Frequency Counts of Extrusion Error ReLU	Frequency Counts of Extrusion Error Tanh	Frequency Counts of Extrusion Error Sigmoid	Frequency Counts of Extrusion Error Softplus
-13	-12	0.332225914	0.664451827	0.332225914	0
-11	-10	0.996677741	0.332225914	0.332225914	0.332225914
-9	-8	0.996677741	2.657807309	0.664451827	1.328903654
-7	-6	0.664451827	0.332225914	0.996677741	1.661129568
-5	-4	1.993355482	0.996677741	13.28903654	0.996677741
-3	-2	16.94352159	19.6013289	8.637873754	9.634551495
-1	0	20.93023256	25.24916944	23.92026578	22.92358804
1	2	40.86378738	34.2192691	32.22591362	34.2192691
3	4	7.973421927	14.28571429	13.95348837	19.26910299
5	6	5.980066445	0.332225914	0.996677741	4.651162791
7	8	2.325581395	0.996677741	4.318936877	3.986710963
9	10	0	0.332225914	0.332225914	0.996677741

The count of the absolute errors of the training set and test set by the ReLU activation function is shown in Figure 52. The absolute errors were calculated based on the difference between the predicted extrusion length and the actual extrusion length. The relevant error was the error divided by the actual extrusion length. The relevant error is a measure of the sample precision [91]. The statistical results of the relevant errors for both the training set and the test set are shown in Table 13 and Table 14. The results show that among the 376 sets of the predicted length of extrusion, 50% were within the 5% relevant error range, approximately 80% of the predicted length of extrusion were within the 10% relevant error range, and 92% of the predicted length of extrusion were within the 15% relevant error range. This ANN model was employed as the control function of the actual print.

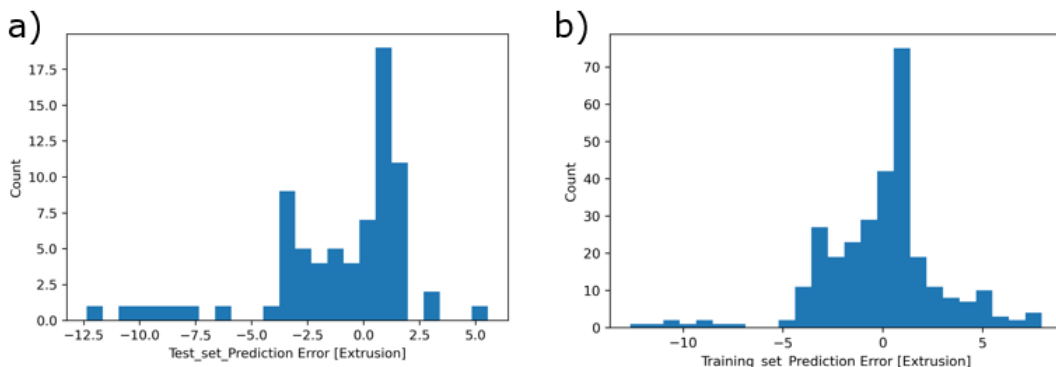


Figure 52 Count of error (mm) of the training set and test set: a) test set and b) training set

Table 13 Statistics of relevant errors for the ANN model

Relative Error Center (%)	Bin End	Count	Frequency (%)
-37.5	-35	0	0
-32.5	-30	2	0.53191
-27.5	-25	5	1.32979
-22.5	-20	7	1.8617
-17.5	-15	2	0.53191
-12.5	-10	20	5.31915
-7.5	-5	66	17.55319
-2.5	0	62	16.48936
2.5	5	129	34.30851
7.5	10	43	11.43617
12.5	15	15	3.98936
17.5	20	12	3.19149
22.5	25	6	1.59574
27.5	30	6	1.59574
32.5	35	1	0.26596
37.5	40	0	0
42.5	45	0	0
47.5	50	0	0
52.5	55	0	0
57.5	60	0	0
62.5	65	0	0
-37.5	-35	0	0
-32.5	-30	0	0

Table 14 Statistics of the accumulated frequency of relevant error range

Relevant Error Range	Accumulated Frequency (%)
Between -5% and 5%	50.79787
Between -10% and 10%	79.78723
Between -15% and 15%	89.09574
Between -20% and 20%	92.81914

The performance of the trained ANN model in the actual printing condition was verified in the second stage of the control flow, as shown in Figure 47. To successfully call the model in the MATLAB script, a starting loadcell reading and ending loadcell reading must be specified for predicting the extrusion length. The real-time sensor reading of the extrusion was acquired and defined as the starting loadcell reading. The appropriate sensor readings in Figure 53—5500 g, 6500 g, and 7000 g—were selected as the reference sensor reading. The choice of reference loadcell reading was based on the loadcell history for the extrusion length of the 28 mm group in Figure 49 a). This group exhibited the best appearance printing quality during the stable printing stage, which covered the loadcell range between approximately 5500 g and 7200

g. These reference sensor readings acted as the target loadcell readings. As each experiment group's full name was too long to easily reference, an abbreviation name was given to each group, as shown in Table 15. In this study, the focus is the stable stage of the print; as mentioned in chapter 6.9.2, the sensor histories of the 6<sup>th</sup> to 9<sup>th</sup> models belong to this stage. The sensor histories for the models in each group are plotted in Figure 53.

Table 15 Abbreviation name of experiment groups

Full name of the experiment groups	Abbreviation name
Uncontrolled group with the extrusion length of 20 mm group	Extrusion 20 mm
Uncontrolled group with the extrusion length of 28 mm group	Extrusion 28 mm
Uncontrolled group with the extrusion length of 32 mm group	Extrusion 32 mm
Uncontrolled group with the extrusion length of 36 mm group	Extrusion 36 mm
Controlled group with target loadcell reading or 5500 g	RFE 5500
Controlled group with target loadcell reading or 6500 g	RFE 6500
Controlled group with target loadcell reading or 7000 g	RFE 7000

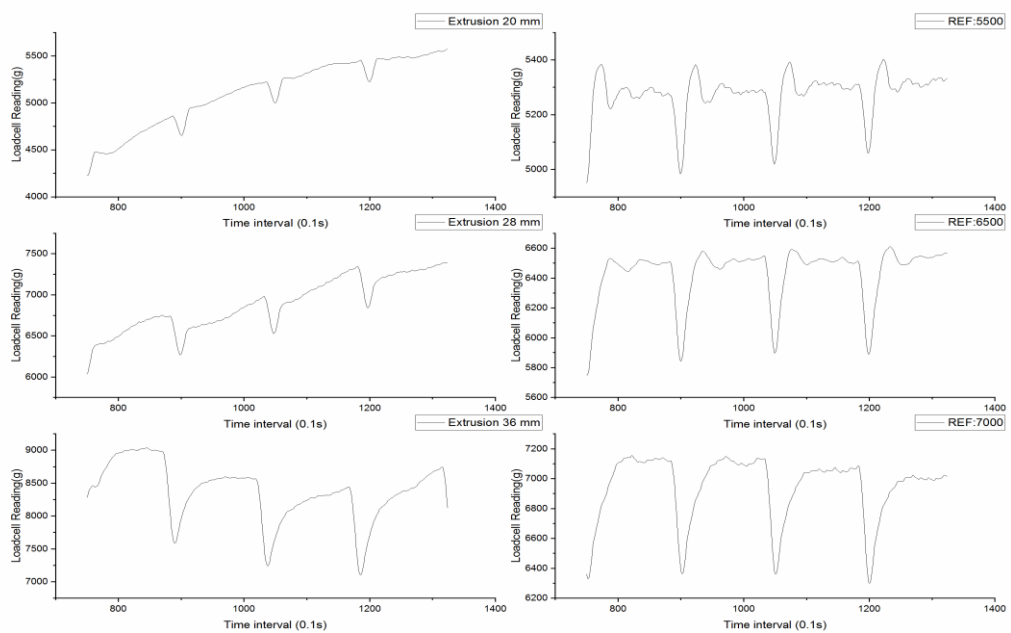


Figure 53 Sensor histories of the 6<sup>th</sup> to 9<sup>th</sup> models in variance printing condition: a) extrusion length of 20 mm, b) extrusion length of 28 mm, c) extrusion length of 36 mm, d) controlled group with target sensor reading of 5500 g, e) controlled group with target sensor reading of 6500 g, and f) controlled group with target sensor reading of 7000 g

As stated in chapter 6.9.2, each model contained 144 data points; thus, complete sensor

histories for the 6<sup>th</sup> to 9<sup>th</sup> models contained 576 data points. The statistical results of the collected 576 data points for each group in Figure 53 are shown in Table 16. Table 16 shows that the standard error, standard deviation, and variance for the controlled groups were lower than those of the uncontrolled groups. The standard error, standard deviation, and sample variance are measurements to express each data set's precision. The relevant equations were expressed as equations (38–39). The sensor reading histories of the controlled groups were more stable than that of the uncontrolled groups. The pressure was successfully controlled and stabilized by the trained ANN model.

$$SE = \frac{\sigma}{\sqrt{n}} \quad (38)$$

$$S^2 = \frac{\sum(x_i - \bar{x})^2}{n - 1} \quad (39)$$

where SE is the standard error,  $\sigma$  is the standard deviation,  $S^2$  is the sample variance,  $x_i$  is the value of a sample,  $\bar{x}$  is the mean value of all samples, and n is the sample size.

It is also notable that there was a rapid loadcell reading change between two adjacent models caused by the rapid motion between models in Stage III. Figure 53 shows that the change in amplitude among the controlled groups was more extensive than that of the uncontrolled groups. This change was because the length of extrusion in the controlled group was a predicted variable. The objective of the control loop was to ensure the in-process pressure near the targeted pressure. Thus, when the difference between the in-process loadcell reading and the targeted loadcell reading was small, the predicted extrusion would be small to maintain a stable loadcell reading. For the uncontrolled group, the process extrusion was constant regardless of the current printing status. Thus at the end of Stage II, the extrusion of the uncontrolled group was greater than that of the controlled group. Therefore, for the process in Stage III, the loadcell reading decreased more significantly in the controlled group than that of the uncontrolled group. For the process in Stage I, the large difference between the actual loadcell reading and the targeted loadcell reading in the controlled group resulted in a large predicted extrusion length, which rapidly increased the in-process loadcell reading rapidly. This phenomenon indicated that the control loop could improve the system's response toward loadcell reading changes. By optimizing the printing path, the rapid loadcell change in Stage III could be reduced and even eliminated. The printing path optimization was not discussed in this study and could be treated as independent research in the future.

Table 16 Statistical results of the sensor histories for variance processes

	Extrusion 20 mm	Extrusion 28 mm	Extrusion 36 mm	REF:5500	REF:6500	REF:7000
Mean (g)	5111.490435	6887.02087	8375.547826	5278.212174	6436.9461	6948.278261
Standard Error (g)	14.56731079	13.25551141	17.81227178	3.227323374	7.6352953	8.937909248
Standard Deviation (g)	349.3118414	317.8559974	427.1232726	77.38849588	183.08795	214.3235346
Sample Variance (g <sup>2</sup> )	122018.7625	101032.4351	182434.29	5988.979294	33521.197	45934.57749
Sample Size	576	576	576	576	576	576

## 6.9.4 Characterization of Printed Patterns

### 6.9.4.1 Characterization of the Whole Pattern

The surface metrology method was adopted to analyze the widths of the printed patterns. Figure 48 shows all visual profiles of the uncontrolled group with varying extrusion lengths. The overall visual printing quality of the uncontrolled 28 mm group, 32 mm group, and 36 mm group were better than that of other groups. These examples adequately represented the low, medium, and high extrusion range. Profiles for the printed patterns of the uncontrolled 28 mm, 32 mm, 36 mm, and controlled RFE 5500, RFE 6500, and RFE 7000 groups are shown in Figure 54. The width information of the models in Figure 54 were measured by a confocal microscope. As shown in Figure 55, each model was sliced into 22 cross-sectional profiles, which were evenly distributed in the 11 tracks. These cross-section profiles were labeled in the order of printing.


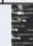

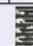

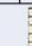

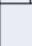








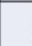






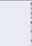

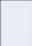


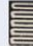
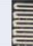
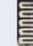



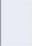



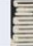

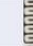






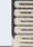



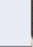
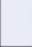

Profile for Extrusion	1 <sup>st</sup> Print in pattern	2 <sup>nd</sup> Print in pattern	3 <sup>rd</sup> Print in pattern	4 <sup>th</sup> Print in pattern	5 <sup>th</sup> Print in pattern	6 <sup>th</sup> Print in pattern	7 <sup>th</sup> Print in pattern	8 <sup>th</sup> Print in pattern	9 <sup>th</sup> Print in pattern
28 mm									
32 mm									
36 mm									
Controlled RFE 5500									
Controlled RFE 6500									
Controlled RFE 7000									

Figure 54 Profiles for the printed pattern in various conditions. Uncontrolled groups: extrusion 28 mm, extrusion 32 mm, and extrusion 36 mm; controlled groups: RFE 5000, 6500, and 7000.

The printed profiles in controlled and uncontrolled conditions are shown in Figure 54. The mean width of each model in various printing conditions was calculated based on the 22 width

data, as shown in Figure 56. The error bars in the figure were calculated as the standard error of the 22 width data for each model. The first four models in the uncontrolled 28 mm group and the first three models in the 32 mm group failed to form a continuous print; so the average width for these seven groups was zero. As discussed in chapter 6.9.2, a stable print stage is when the shear stress is greater than the slurry yield stress, and the ceramic slurry can continuously flow out of the nozzle. As shown in Figure 54, the 5<sup>th</sup> model in the uncontrolled 28 mm group, the 4<sup>th</sup> model in the uncontrolled 32 mm, and the 1<sup>st</sup> model in the uncontrolled 36 mm group contain dash-like tracks. Thus, the stable printing stage for the 28 mm group start from the 6<sup>th</sup> model, while that for the 36 mm group start from the 2<sup>nd</sup> model. As explained in chapter 6.9.1, a pre-pressure operation was integrated into the control loop to ensure that the printing operation of the controlled group reached a stable stage before the 1<sup>st</sup> model. Thus, it can be observed that the visual quality of the first model in the controlled groups is better than those of the uncontrolled groups.

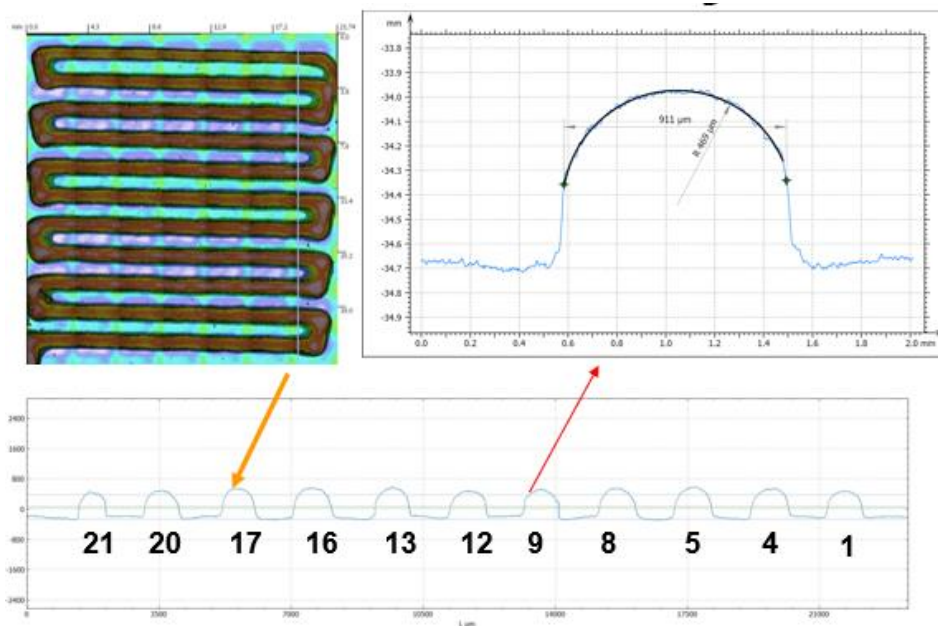


Figure 55 Example of a printed model to be analyzed. a) Overview of a model in REF 6500 group acquired by the confocal microscope, b) cross-sectional profile of measurement points #1, 4, 5, 8, 9, 12, 13, 16, 17, 20, and 21, and c) detailed profile of measurement points

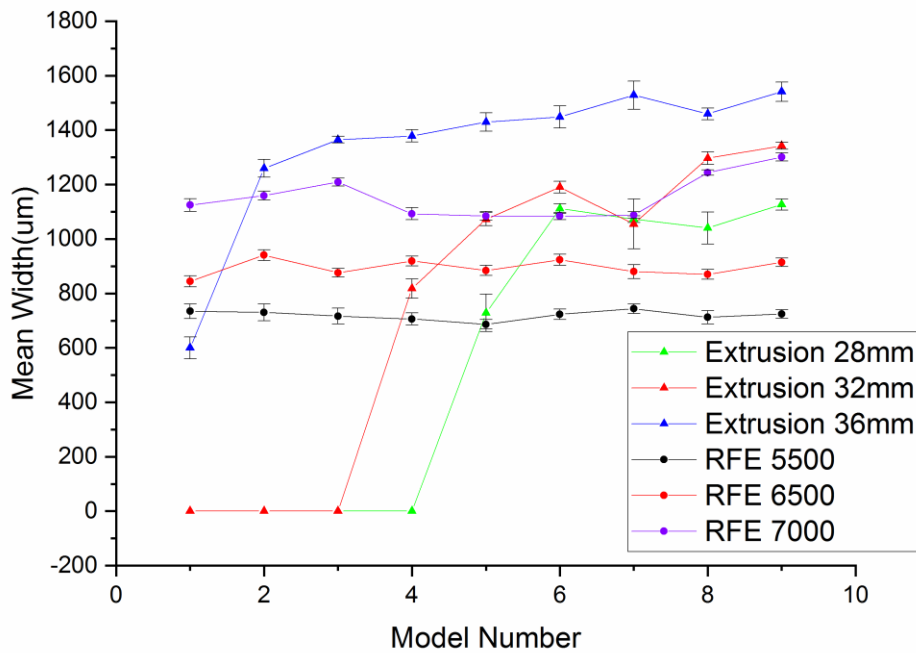


Figure 56 Mean profile width statistics for each model printed by various printing conditions.

Table 17 Statistical results of the profile information for the mean of each model in the uncontrolled 28 mm, 32 mm, and 36 mm groups and controlled REF 5500, RFE 6500, and REF 7000 groups

	Extrusion 28mm	Extrusion 32mm	Extrusion 36mm	RFE 5500	RFE 6500	RFE 7000
Mean (um)	564.4333333	752.7884	1334.332991	720.1065489	894.7757278	1154.119999
Standard Error (um)	182.6415996	194.8338325	96.14620083	5.668457563	10.394081	26.73291507
Standard Deviation (um)	547.9247987	584.5014974	288.4386025	17.00537269	31.18224301	80.19874522
Sample Variance (um <sup>2</sup> )	300221.585	341642.0004	83196.8274	289.1827003	972.332279	6431.838735
Sample Size	9	9	9	9	9	9

The statistical results of the mean width for each printed model in the uncontrolled 28 mm, 32 mm, and 36 mm groups and controlled REF 5500, RFE 6500, and REF 7000 groups are shown in Table 17. The worst mean width variations in the models for a controlled group, RFE 7000, is better than the best uncontrolled group, Extrusion 36 mm, in standard error (26.73  $\mu\text{m}$  vs. 93.14  $\mu\text{m}$ , respectively), standard deviation (81.2  $\mu\text{m}$  vs. 288.44  $\mu\text{m}$ ), and sample variance (6431.84  $\mu\text{m}^2$  vs. 83196.83  $\mu\text{m}^2$ ). As shown in Figure 56, each printed model's mean width



in the controlled group exhibits improved consistency compared with that of the uncontrolled groups. An obvious trend is that the controlled group's mean width of the printed model increases with an increase in the target loadcell reading.

#### 6.9.4.2 Characterization of the Single Model

Similar to the approach in chapter 6.9.4.2, the surface metrology method was adopted to analyze the profile of a single model that is printed in the stable printing stage with various printing conditions. The selected model was measured by a confocal microscope and sliced into 110 cross-sectional profiles, which were evenly distributed among the 11 tracks. These cross-sectional profiles were labeled in the order of printing and were analyzed by MountainsMap software. As shown in Figure 54 and Figure 56, the observed width varies drastically in the uncontrolled group, whereas the controlled group showed improved consistency in the printed width. The 7<sup>th</sup> model in the uncontrolled groups typically shows the best apparent quality for all the tested printing conditions. Thus, the 7<sup>th</sup> model had been chosen for detailed characterization. In the controlled groups, the first model was chosen as the typical model to represent the relatively consistent printing quality of each group. Figure 57 compares the results of the detailed analysis of the 7<sup>th</sup> model from the uncontrolled 28 mm and 36 mm groups.

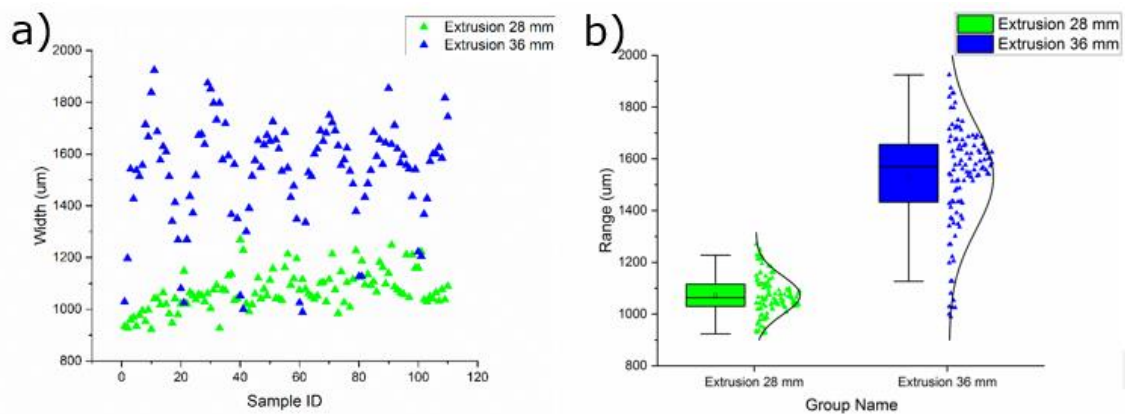


Figure 57 Statistical width information of the 7<sup>th</sup> model in uncontrolled printing conditions: a) Statistical width information for the whole model and b) range and distribution of each model

The statistical width information of the uncontrolled printing condition is shown in Figure 57. The widths of the printed model in the uncontrolled groups exhibit a considerable variation

along the printing direction. Figure 57 b) shows the boxplot and distribution of 110 measured width information for the uncontrolled 28 mm and 36 mm groups. The range of the box was determined by the 25<sup>th</sup> and 75<sup>th</sup> percentiles, while the whiskers were determined by the 5<sup>th</sup> and 95<sup>th</sup> percentiles. These results show that the measured width distribution of the 36 mm group is more discrete than that of the 28 mm group. As shown in Figure 58, the print in the 28 mm group shows a more uniform trend compared with the 36 mm group. In the 36 mm group, some of the neighboring tracks merged with each other, which contributes to the width variance. The width quality of the 7<sup>th</sup> model in the 28 mm group is better than that of the 36 mm group.

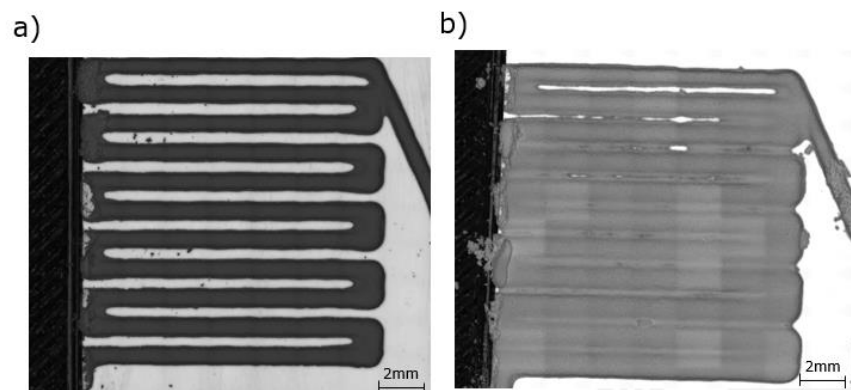


Figure 58 Overview of the 7<sup>th</sup> model in the uncontrolled groups acquired by the confocal microscope: a) extrusion length of 28 mm and b) extrusion length of 36 mm

Figure 59 a) is the scatter plot of 110 width measurement points for selected models in controlled and uncontrolled printing conditions. Figure 59 b) shows the boxplot diagram that corresponds to each printing condition. It can be observed from these two figures that the width quality of the printing in each controlled group has a relatively small width variation along the printing direction, and the width distribution is relatively uniform. Whereas the printing width of the uncontrolled group has a large variance along the printing direction, and the distribution is more scattered compared with that of the controlled groups.

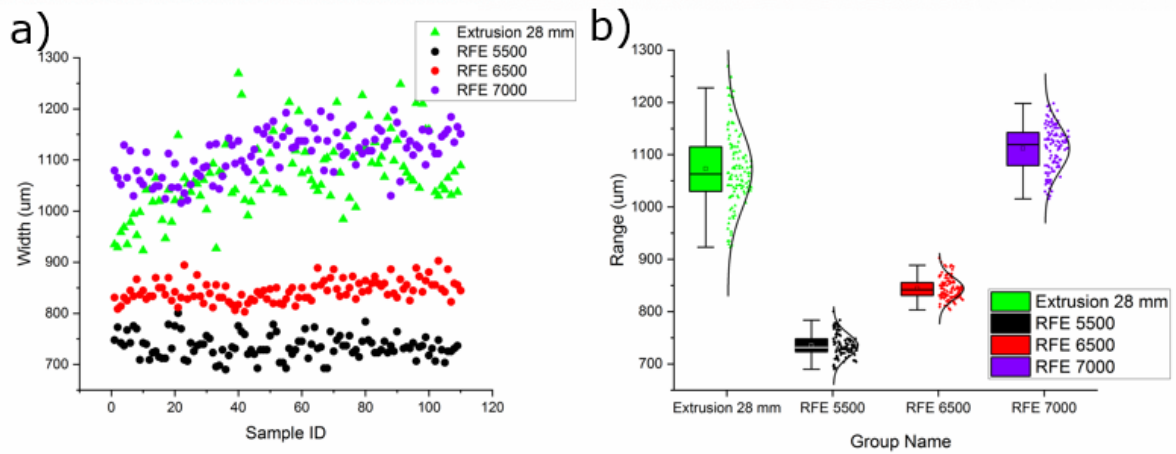


Figure 59 Information of the 7<sup>th</sup> model for the uncontrolled 28 mm group, and the typical model in controlled RFE 5500 group, RFE 6500, and RFE 7000 group: a) statistical width information for the whole model, and b) range and distribution of each model

Table 18 Statistical results of width information for the 7<sup>th</sup> model for the uncontrolled 28 mm group, and the typical model in controlled RFE 5500 group, RFE 6500, and RFE 7000 group.

	Extrusion 28 mm	RFE 5500	RFE 6500	RFE 7000
Mean (um)	1072.79688	735.1566667	844.1836364	1119.03611
Standard Error (um)	7.112759374	2.196787492	1.977800417	4.050423
Standard Deviation (um)	74.59924966	22.8296853	20.74334578	42.4811948
Sample Variance (um <sup>2</sup> )	5565.04805	521.1945308	430.286394	1804.65191
Sample Size	110	110	110	110

Table 18 shows the statistical results of width information for the 7<sup>th</sup> model of the uncontrolled 28 mm group and typical models in the controlled RFE 5500, RFE 6500, and RFE 7000 groups. The RFE 7000 group exhibits the worst consistency among all controlled groups, as the standard error, standard deviation, and sample variance are larger than those of other controlled groups. However, the print stability in the RFE 7000 groups is still better than that of the uncontrolled 28 mm group for standard error (4.05 vs. 7.11, respectively), standard deviation (42.48 vs. 74.60), and sample variance (1804.65 vs. 5565.04). This observation suggests that the width in the typical models in the controlled groups has better consistency and stability than the 7<sup>th</sup> model in the uncontrolled 28 mm group. Based on Figure 48, the 7<sup>th</sup> model in the 28 mm group has the best apparent quality in the uncontrolled group, whereas the typical models represent the average quality of the controlled group. Thus, adding closed-loop control resulted in better consistency and stability in printing quality.

### **6.9.5 Concluding Remarks**

In this study, a method to integrate closed-loop, real-time processing control based on machine learning was created and verified. A novel process flow that utilizes an ANN model as the control logic was implemented. This control loop was successfully created to predict the processing parameter based on the given real-time status of the robocasting printer and the desired target. The sensor reading history showed that by adopting ANN-governed closed-loop control, the process pressure exhibited a more stable trend than that of an open-loop process. The distribution in the printed width of the controlled group showed better consistency than that of the uncontrolled groups, which indicates the potential to control the width distribution by integrating machine learning enabled closed-loop control into the current robocasting process.

## 7 Summary

### 7.1 Conclusion and Impact

This dissertation mainly focuses on improving ceramic additive manufacturing by machine learning-enabled closed-loop control. The critical parameters for ceramic robocasting were prescribed in this research to achieve this goal. The relationships among the functional requirements, design parameters, and process variables were analyzed.

The mathematical models and the axiomatic design approach were applied to analyze the current ceramic robocasting process. FR-DP and DP-PV matrices and decompositions were demonstrated, and the relationships among FR-DP-PV were analyzed. To the best of the author's knowledge, this work is the first research to demonstrate and explain FR-DP-PV interactions. Possible solutions for optimizing and redesigning the current ceramic robocasting manufacturing process were discussed. This research also proved that the current robocasting process is a heavily coupled system that contains a complex physical model.

In conventional control theory, a clear objective function is the key to successfully achieving control. However, a complex physical model commonly represents that the transfer function will be difficult to create. The work in this study demonstrated a method to integrate machine learning and closed-loop control into the current open-loop control robocasting system. A data-driven method that integrates closed-loop real-time processing parameter control based on machine learning was demonstrated and verified. A database of the relationships among processing pressure, extrusion, and the printed part's quality was established. An artificial neural network model was constructed and trained based on the established database. The novel process flow utilized the pre-trained ANN model as the control logic to successfully predict the processing parameter based on the given real-time status of the robocasting printer and desired target. The sensor reading showed that by adopting the ANN-governed closed-loop control, the process pressure exhibited a more stable trend than that of the open-loop process. An improvement in printing quality has been observed by comparing the controlled printing results with the uncontrolled printing results. Closed-loop control resulted in better consistency and stability in printing quality compared with that of the uncontrolled process. This project suggests that machine learning, which enabled closed-loop control, is a promising approach to improve the printing quality of the ceramic, selective deposition additive manufacturing process.

## 7.2 Recommendations for Future Works

In this research, the robocasting process was analyzed based on the Cartesian coordinate system; however, it can also be examined based on function. These two different clues may produce different decompositions for the same manufacturing system. These differences can be compared and analyzed to determine different causes.

The ceramic slurry employed in this work was pre-defined. The behavior of the slurry with different rheological properties can be investigated in future studies. The rheological properties can be integrated into the ANN model as input.

The work in this study expressed a method for integrating machine learning and closed-loop control into the current open-loop control robocasting system. In this study, the “pressure-extrusion-width of print” was chosen as an example to demonstrate this method. However, it should not only be limited to pressure-extrusion control. The control loop's core control logic, the ANN, is a data-driven machine learning method in which the realization of control requires sufficient data sets and approximate physical relations. This property introduces the potential to extend the ANN governed by the closed-loop method into a broader application in the ceramic AM field, especially when a complete physical model is hard to construct.

In this study, the variance in the printed width was successfully stabilized. However, a mathematical model between the process variables and the printed width was not created in this work. The intelligent process of materials directly utilizes material properties as a feedback signal to control the process variables. Kushner et al.'s intelligent processing of materials (IPM) was first demonstrated in 1986 as a systemic tool to design and control the synthesis and process of materials [92]. The conventional closed-loop control strategy commonly concentrates on comparing the measured signal and the pre-set signal. Simultaneously, intelligent processing characterizes the material properties and controls the material variables [93]. As shown in Figure 60, in the conventional closed-loop control strategy, disturbances produced during the manufacturing process can be compensated by the feedback loop, which has no influence on the input of the whole process. [69]. In the IPM control strategy, material properties are integrated into the loop and govern the whole control strategy by online adjustment of the process inputs. An accurate physics relationship between the material properties and the performance is needed to ensure the success of IPM. By combining the IPM theory and machine learning, it is possible to generate a more comprehensive prediction model.

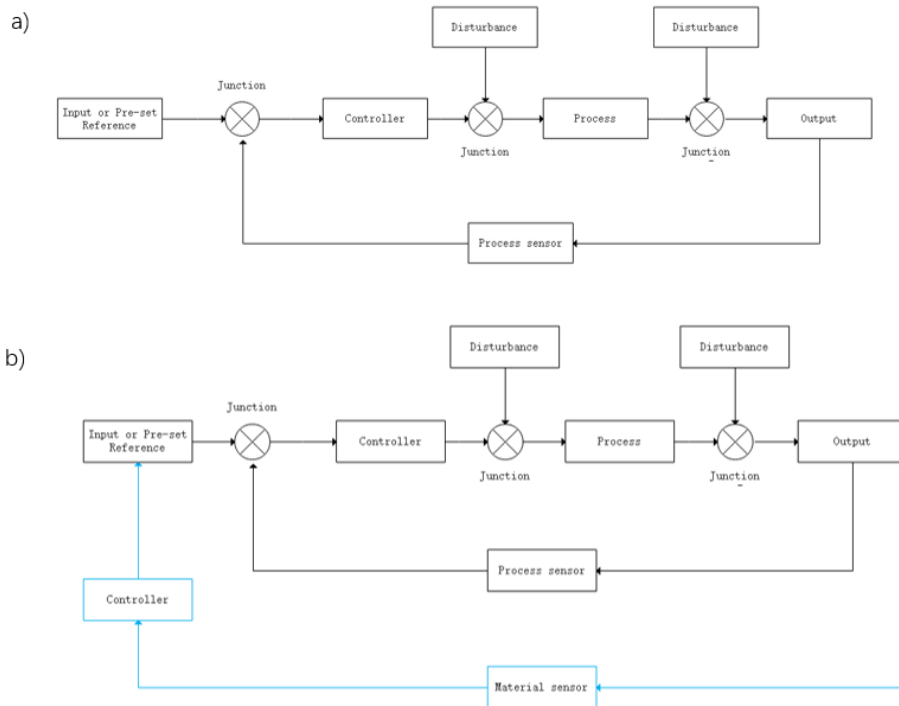


Figure 60 Block diagrams of closed-loop control systems: a) conventional closed-loop control and b) intelligent process of material [69]

This study comprises the initial feasibility research that proves that the print width quality can be improved by integrating machine learning-enabled closed-loop control into the current robocasting system. In-depth research of the mathematical relationship between the pressure and printed width was not conducted but can be carried out as a future study.

## 8 Publication and Presentations

### 8.1 Accepted Journal Publications

1. Bo Xin, Zhaolong Zhang, Jie Zhang, Yiming Rong (2016). Dynamic Property Regulation of Axially Functional Graded Beams for Airfoil Structure. *ASME-IDETC 2016*. (EI: 20170103212622)
2. Jin, X., Li, L., Ju, W., Zhang, Z., & Yang, X. (2016). Multibody modeling of varying complexity for dynamic analysis of large-scale wind turbines. *Renewable Energy*, 90, 336–351.
3. Jin, X., Ju, W., Zhang, Z., Guo, L., & Yang, X. (2016). System safety analysis of large wind turbines. *Renewable and Sustainable Energy Reviews*, 56, 1293–1307.
4. Jin, X., Zhang, Z., Shi, X., & Ju, W. (2014). A review on wind power industry and corresponding insurance market in China: Current status and challenges. *Renewable and Sustainable Energy Reviews*, 38, 1069–1082.
5. Kudzal, A., Zhang, Z., & Lagassey, J. (2014). Axiomatic design of an improved egg carton manufacturing process. In Proceedings of the 8th international conference on axiomatic design. Campus de Caparica, Portugal (p. 187–194).

### 8.2 Conferences

#### Material Science and Technology

1. Zhaolong Zhang, Richard D. Sisson, Christopher Brown, and Jianyu Liang. In-Process Quality Control and Optimization for Ceramic 3D Printing. Virtual, Oct. 2020.

#### International Design Engineering Technical Conferences & Computers and Information in Engineering Conference

2. Bo Xin, Zhaolong Zhang. Dynamic Property Regulation of Axially Functional Graded Beams for Airfoil Structure. Charlotte, North Carolina, 2016.



## 9 References

1. Scott, J., Gupta, N., Wember, C., Newsom, S., Wohlers, T., Caffrey, T, *Additive Manufacturing: Status and Opportunities*. 2012.
2. Zocca, A., et al., *Additive Manufacturing of Ceramics: Issues, Potentialities, and Opportunities*. Journal of the American Ceramic Society, 2015. **98**(7): p. 1983-2001.
3. Deckers, J., J. Vleugels, and J.-P. Kruth, *Additive manufacturing of ceramics: a review*. Journal of Ceramic Science and Technology, 2014. **5**(4): p. 245-260.
4. Schlordtil, T. and P. Greil, *Robocasting of alumina lattice truss structures*. J. Ceram. Sci. Technol, 2012. **3**(2): p. 81-8.
5. Regenfuss, P., et al., *Material depending mechanisms in laser micro sintering*. 2007: p. 403-418.
6. Sher, D., *Market report: the 3.1 billion usd market for ceramics additive manufacturing.*, in Smartech Markets Publishing. 2018.
7. Nagrath, I., *Control systems engineering*. 2006: New Age International.
8. Janney, M.A., et al., *Gelcast tooling: net shape casting and green machining*. Material and manufacturing process, 1998. **13**(3): p. 389-403.
9. Exner, H., et al., *Laser micro sintering: A new method to generate metal and ceramic parts of high resolution with sub-micrometer powder*. Virtual and physical prototyping, 2008. **3**(1): p. 3-11.
10. Maruo S, Ikuta K. *Submicron stereolithography for the production of freely movable mechanisms by using single-photon polymerization*. Sensors and Actuators A: Physical. 2002 Aug 15;100(1):70-6.
11. Hong, Y et al. *Fabricating ceramics with embedded microchannels using an integrated additive manufacturing and laser machining method*. Journal of the American Ceramic Society 2019. **102**.3: 1071-1082.
12. Deckers, J., et al., *Additive manufacturing of ceramics: a review*. 2014. **5**(4): p. 245-260.
13. Filser, F., P. Kocher, and L.J.A.a. Gauckler, *Net-shaping of ceramic components by direct ceramic machining*. 2003. **23**(4): p. 382-390.
14. Kramer, T.R., et al., *The NIST RS274NGC Interpreter: Version 3*. 2000, US Department of Commerce, National Institute of Standards and Technology.
15. Willis, M.J. and M.T. Tham, *Advanced process control*. Department of Chemical and Process Engineering, University of Newcastle Upon Tyne, UK, 1994.

16. Hoskins, J. and D. Himmelblau, *Process control via artificial neural networks and reinforcement learning*. Computers & chemical engineering, 1992. **16**(4): p. 241-251.
17. Mathewson, B. B., et al. *Automated Fabrication of Ceramic Components from Tape-Cast Ceramic*. 1995 International Solid Freeform Fabrication Symposium. 1995..
18. Liu, Z., et al. *Metal and ceramic components made via CAM-LEM technology*. Proceedings of the Solid Freeform Fabrication Symposium, Austin/TX, USA, S. 1996.
19. Feygin, M., B. Hsieh, and M.A. Melkanoff, *Laminated Object Manufacturing (Lom) - A New Tool In The Cim World*. Human Aspects in Computer Integrated Manufacturing, 1992. 3: p. 457-464.
20. Feygin, M. and S.S. Pak, *Laminated object manufacturing apparatus and method*. 1999, Google Patents.
21. Jacobs, P.F. and J. Richter. *Advances in stereolithography accuracy*. 1991 International Solid Freeform Fabrication Symposium. 1991.
22. Leyden, R.N., et al., *Stereolithography method and apparatus*. 1992, Google Patents.
23. Beaman, J., J. Darrah, and C. Deckard, *Patent No. US 5155324 A*. 1986, United States.
24. Lakshminarayan, U. and H. Marcus. *An Experimental Study of the Relationship between Microstructure and Mechanical Properties of a Ceramic Composite Fabricated by Selective Laser Sintering*. 1992 International Solid Freeform Fabrication Symposium. 1992.
25. Subramanian, K., G. Zong, and H. Marcus. *Selective laser sintering and reaction sintering of ceramic composites*. 1992 International Solid Freeform Fabrication Symposium. 1992.
26. Exner, Hv, et al. *Laser micro sintering: A new method to generate metal and ceramic parts of high resolution with sub-micrometer powder*. Virtual and physical prototyping 3.1 (2008): 3-11..
27. Regenfuss, P., et al., *Principles of laser micro sintering*. **Rapid Prototyping Journal** .2007. 13(4): p. 204-212.
28. Sp, H.E., et al., *Laser Micro Sintering of Ceramic Materials*.
29. Streek, A., et al. *Processing of silicon carbide by laser micro sintering*. The Proceedings of the 17th Annual SFF Symposium. 2006.
30. Forderhase, P.F., et al., *Apparatus and method for producing parts with multi-directional powder delivery*. 1993, Google Patents.
31. Cawley, J.D.J.C.O.i.S.S. and M. Science, *Solid freeform fabrication of ceramics*. 1999. **4**(5): p. 483-489.

32. Seitz, H., et al., *Three - dimensional printing of porous ceramic scaffolds for bone tissue engineering*. Journal of Biomedical Materials Research Part B: Applied Biomaterials: An Official Journal of The Society for Biomaterials, The Japanese Society for Biomaterials, and The Australian Society for Biomaterials and the Korean Society for Biomaterials. 2005. **74**(2): p. 782-788.
33. Lu, K. and W.T.J.P.t. Reynolds, *3DP process for fine mesh structure printing*. Powder technology. 2008. **187**(1): p. 11-18.
34. Vorndran, E., et al., *3D printing of  $\beta$ -tricalcium phosphate ceramics*. Dental Materials. 2009. **25**(5): p. e18-e19.
35. Tang, H.H., *Building ultra-thin layers by ceramic laser sintering*. Materials Transactions, 2006. **47**(3): p. 889-897.
36. MultiJet Plastic Printers. 2017.
37. Vaezi, M., H. Seitz, and S.F. Yang, *A review on 3D micro-additive manufacturing technologies*. International Journal of Advanced Manufacturing Technology, 2013. **67**(5-8): p. 1721-1754.
38. Travitzky, N., et al., *Additive Manufacturing of Ceramic-Based Materials*. Advanced Engineering Materials, 2014. **16**(6): p. 729-754.
39. Cesarano, J. *A review of robocasting technology*. Symposium on Solid Freeform and Additive Fabrication. 1998. Boston, Ma: Materials Research Society.
40. Huang, T., et al., *Freeze-form extrusion fabrication of ceramic parts*. Virtual and Physical Prototyping. 2006. **1**(2): p. 93-100.
41. Scheithauer, U., et al., *Thermoplastic 3D printing—an additive manufacturing method for producing dense ceramics*. International journal of applied ceramic technology. 2015. **12**(1): p. 26-31.
42. Cesarano, J. *A review of robocasting technology*. Symposium on Solid Freeform and Additive Fabrication. 1998. Boston, Ma: Materials Research Society. 1998. **542**.
43. He, G., D.A. Hirschfeld, and J. CESARANO III, *Processing and mechanical properties of silicon nitride formed by robocasting aqueous slurries*. 2000, Sandia National Labs., Albuquerque, NM (US); Sandia National Labs., Livermore, CA (US).
44. Tuttle, B.A., et al., *Robocast Pb (Zr<sub>0.95</sub>Ti<sub>0.05</sub>) O<sub>3</sub> ceramic monoliths and composites*. Journal of the American Ceramic Society 2001. **84**(4): p. 872-874.
45. San Marchi, C., et al., *Alumina–aluminum interpenetrating-phase composites with three-dimensional periodic architecture*. Scripta Materialia. 2003. **49**(9): p. 861-866.

46. Stuecker, J.N., et al., *Advanced support structures for enhanced catalytic activity*. Industrial & engineering chemistry research. 2004. **43**(1): p. 51-55.
47. Nadkarni, S.S. and J.E.J.J.o.t.A.C.S. Smay, *Concentrated barium titanate colloidal gels prepared by bridging flocculation for use in solid freeform fabrication*. Journal of the American Ceramic Society. 2006. **89**(1): p. 96-103.
48. Duoss, E.B., M. Twardowski, and J.A.J.A.M. Lewis, *Sol - Gel inks for Direct - Write assembly of functional oxides*. Advanced Materials 2007. **19**(21): p. 3485-3489.
49. Şakar-Deliormanlı, A., et al., *Rheological behavior of PMN gels for solid freeform fabrication*. Colloids and Surfaces A: Physicochemical and Engineering Aspects. 2008. **324**(1-3): p. 159-166.
50. Lu, X., et al., *Fine lattice structures fabricated by extrusion freeforming: Process variables*. Journal of Materials Processing Technology. 2009. **209**(10): p. 4654-4661.
51. Mason, M.S., et al., *Aqueous-based extrusion of high solids loading ceramic pastes: Process modeling and control*. Journal of materials processing technology. 2009. **209**(6): p. 2946-2957.
52. Lu, X., et al., *Solvent-based paste extrusion solid freeforming*. Journal of the European Ceramic Societ. 2010. **30**(1): p. 1-10.
53. Huang, T., et al., *Porous and strong bioactive glass (13–93) scaffolds fabricated by freeze extrusion technique*. Materials Science and Engineering: C. 2011. **31**(7): p. 1482-1489.
54. Leu, M.C., et al. *Freeze-form extrusion fabrication of composite structures*. in *Proceedings of the Solid Freeform Fabrication Symposium*. Proceedings of the Solid Freeform Fabrication Symposium. Austin, TX. 2011.
55. Cai, K., et al., *Geometrically complex silicon carbide structures fabricated by robocasting*. Journal of the American Ceramic Society. 2012. **95**(8): p. 2660-2666.
56. Houmard, M., et al., *On the structural, mechanical, and biodegradation properties of HA/β - TCP robocast scaffolds*. Journal of Biomedical Materials Research Part B: Applied Biomaterials. 2013. **101**(7): p. 1233-1242.
57. Sun, K., et al., *3D printing of interdigitated Li - Ion microbattery architectures*. Advanced materials. 2013. **25**(33): p. 4539-4543.
58. Suh, N.P., A. Bell, and D. Gossard, *On an axiomatic approach to manufacturing and manufacturing systems*. 1978.
59. Farid, A. and N. Suh, *Axiomatic design in large systems*. Switzerland: Springer, 2016.
60. Brown, C.A. and E. Rauch. *Axiomatic Design for Creativity, Sustainability, and*

*Industry 4.0*. MATEC Web of Conferences. 2019. EDP Sciences.

61. Tomiyama, T., et al., *Design methodologies: Industrial and educational applications*. CIRP annals, 2009. **58**(2): p. 543-565.

62. Le Masson, P., B. Weil, and A. Hatchuel, *Design theory*. 2017: Springer.

63. Brown, C.A. *Axiomatic design of manufacturing processes considering coupling*. Proceedings of ICAD2014 the Eighth International Conference on Axiomatic Design. 2014.

64. Brown, C.A. *Kinds of coupling and approaches to deal with them*. Proceedings of 4th ICAD2006, The Fourth International Conference on Axiomatic Design, Firenze June. 2006.

65. Thompson, M.K. *A classification of procedural errors in the definition of functional requirements in Axiomatic Design theory*. 7th International Conference on Axiomatic Design (ICAD 2013). 2013. ICAD.

66. Suh, N.P., *Complexity: theory and applications*. 2005: Oxford University Press on Demand.

67. Suh, N.P., *The principles of design*. 1990: Oxford University Press on Demand.

68. Wiener, N., *Cybernetics or Control and Communication in the Animal and the Machine*. 1948: MIT press.

69. Nise, N.S., *Control Systems Engineering, (With Cd)*. 2007: John Wiley & Sons.

70. Cong, S. and Y. Liang, *PID-like neural network nonlinear adaptive control for uncertain multivariable motion control systems*. IEEE Transactions on Industrial Electronics, 2009. **56**(10): p. 3872-3879.

71. Bennett, S., *A history of control engineering, 1930-1955*. 1993: IET.

72. Bansal, H.O., R. Sharma, and P. Shreeraman, *PID controller tuning techniques: a review*. Journal of control engineering and technology, 2012. **2**(4): p. 168-176.

73. Nwankpa, C., et al., *Activation functions: Comparison of trends in practice and research for deep learning*. arXiv preprint arXiv:1811.03378, 2018.

74. Karlik, B. and A.V. Olgac, *Performance analysis of various activation functions in generalized MLP architectures of neural networks*. International Journal of Artificial Intelligence and Expert Systems, 2011. **1**(4): p. 111-122.

75. Sun, S., et al., *A survey of optimization methods from a machine learning perspective*. IEEE transactions on cybernetics, 2019.

76. 3dpotter. 3D PotterBot 7 Pro.

77. Walker, W.H., et al., *Principles of chemical engineering*. 1923: McGraw-Hill book Company, Incorporated.

78. Rangarajan, S., et al., *Powder processing, rheology, and mechanical properties of*

*feedstock for fused deposition of Si<sub>3</sub>N<sub>4</sub> ceramics*. Journal of the American Ceramic Society, 2000. **83**(7): p. 1663-1669.

79. Smay, J.E., J. Cesarano, and J.A. Lewis, *Colloidal inks for directed assembly of 3-D periodic structures*. Langmuir, 2002. **18**(14): p. 5429-5437.

80. Nadkarni, S.S. and J.E. Smay, *Concentrated barium titanate colloidal gels prepared by bridging flocculation for use in solid freeform fabrication*. Journal of the American Ceramic Society, 2006. **89**(1): p. 96-103.

81. Faes, M., et al., *Extrusion-based 3D printing of ceramic components*. Procedia Cirp, 2015. **28**: p. 76-81.

82. Xu, X., et al., *Effect of dispersant on the rheological properties and slip casting of concentrated sialon precursor suspensions*. Journal of the European Ceramic Society, 2003. **23**(9): p. 1525-1530.

83. Herschel, W.H. and R. Bulkley, *Konsistenzmessungen von gummi-benzollösungen*. Kolloid-Zeitschrift, 1926. **39**(4): p. 291-300.

84. Schlordt, T., et al., *Robocasting of alumina hollow filament lattice structures*. Journal of the European Ceramic Society, 2013. **33**(15-16): p. 3243-3248.

85. Scherer, G.W., *Bending of gel beams: method for characterizing elastic properties and permeability*. Journal of Non-Crystalline Solids, 1992. **142**: p. 18-35.

86. Mackay, M.E., *The importance of rheological behavior in the additive manufacturing technique material extrusion*. Journal of Rheology, 2018. **62**(6): p. 1549-1561.

87. Covas, J., et al., *Rheological fundamentals of polymer processing*. Vol. 302. 2013: Springer Science & Business Media.

88. Hoelzle, D.J., et al., *Iterative Learning Control for robotic deposition using machine vision*. 2008 American Control Conference. 2008. IEEE.

89. Mott, R.L. and J. Tang, *Machine elements in mechanical design*. Vol. 4. 2004: Pearson Prentice Hall Upper Saddle River.

90. Smoothieware. *G-codes*. Available from: <http://smoothieware.org/supported-g-codes>.

91. Oehlert, G.W., *A first course in design and analysis of experiments*. 2010.

92. Kushner, B. and P. Parrish, *The Intelligent Processing of Advanced Materials*. Intelligent Processing of Materials and Advanced Sensors, 1987: p. 173-184.

93. Pickering, S., *Intelligent processing of materials*. Journal of materials processing technology, 1993. **36**(4): p. 447-465.

## Appendix A

This appendix includes the Arduino script to collect data from the button loadcell at a sampling rate of 10 Hz by using an HX711 24-Bit Analog-to-Digital Converter (Avia, China).

```
//Lib HX711 is from
//https://github.com/bogde/HX711
#include "HX711.h"
#define FILTER_LEN 10
HX711 scale;
long offset;
long filter[FILTER_LEN];
long cali[100];
int pointer;
void setup()
{
  long sum = 0;
  Serial.begin(9600);
  pointer = 0;
  scale.begin(A1, A0, 128);
  for(int i=0;i<30;i++)
  {
    scale.read();
    Serial.println("data discard");
  }
  for(int i=0;i < FILTER_LEN;i++)
  {
    filter[i] = scale.read();
    sum += filter[i];
  }
  offset= sum/FILTER_LEN;
  Serial.println("====offset====");
  Serial.println(offset);
  Serial.println("====done====");
}
void loop() {
  long dataIn = scale.read();
  filter[pointer] = dataIn;
  long sum = 0;
  for(int i = 0; i < FILTER_LEN; i++)
  {
    sum += filter[i];
  }
  long force = (sum/FILTER_LEN-offset)/10;
  pointer = (pointer+1)%FILTER_LEN;
  Serial.println(force);
  Serial.println(dataIn);
}
```

## Appendix B

This appendix expresses data sets used to generate the machine learning model. The verification result, predicted extrusion length and error, are also included in the table.

Starting Loadcell Reading(g)	Target Loadcell Reading(g)	Extrusion length(mm)	Predicted Extrusion length(mm)	Extrusion Error(mm)
2049	2073	22	23.27002335	1.270023346
4024	4083	26	23.58701897	-2.41298103
6100	6113	32	33.17488098	1.174880981
4702	4788	38	25.94402885	-12.0559711
4415	4500	24	24.90459061	0.904590607
4851	4886	38	26.10897255	-11.8910275
4210	4263	26	23.9798336	-2.0201664
2167	2219	22	23.05657959	1.05657959
6235	6253	32	32.14198303	0.141983032
4632	4683	20	25.12681961	5.126819611
6130	6192	34	33.23952484	-0.76047516
6702	6734	28	29.03293419	1.032934189
2361	2401	22	22.64263535	0.642635345
3931	4139	24	25.25023079	1.250230789
6300	6589	28	33.29459381	5.294593811
2203	2511	22	24.66944695	2.669446945
5916	5958	32	33.82906342	1.829063416
8288	8426	36	35.67091751	-0.32908249
4295	4378	24	24.57638359	0.576383591
4963	4979	20	26.63206291	6.632062912
5966	5986	32	33.64603424	1.646034241
6611	6636	28	29.22262383	1.222623825
7723	7777	30	32.08359146	2.083591461
6638	6655	28	28.98116302	0.981163025
4981	5015	20	27.11949348	7.119493484
7781	7833	30	32.31374359	2.313743591
5104	5184	38	28.97378159	-9.02621841
6656	6684	28	29.05800438	1.058004379
5017	5052	20	27.42322731	7.42322731
6000	6058	32	34.22292709	2.222927094
7926	7981	30	32.99311829	2.993118286
4619	4622	24	24.37479401	0.374794006
6721	6776	28	29.21864319	1.218643188
2952	3016	22	22.45801163	0.458011627
5129	5159	20	28.21264076	8.212640762
4746	4766	26	25.12798691	-0.87201309
6838	6882	28	28.96041107	0.960411072



6223	6267	32	32.39624023	0.396240234
6018	6019	34	33.50810242	-0.49189758
5191	5205	20	28.39590836	8.395908356
6270	6293	32	31.89694405	-0.10305595
8330	8397	30	34.93333817	4.933338165
3285	3380	22	22.72269249	0.72269249
3117	3446	22	24.9818821	2.981882095
8049	8427	30	37.73562241	7.735622406
4345	4493	24	25.53043747	1.530437469
3456	3510	22	22.40877724	0.408777237
6219	6255	32	32.37861252	0.378612518
4673	4685	24	24.70987129	0.709871292
5316	5351	20	29.7874794	9.787479401
6100	6149	34	33.39602661	-0.60397339
7065	7103	28	28.96961403	0.969614029
3734	3807	22	23.03373146	1.033731461
8943	9010	30	33.73406601	3.73406601
5822	5834	38	33.2091217	-4.7908783
7204	7263	28	29.85651016	1.856510162
5836	5848	38	33.2410965	-4.7589035
6538	6596	32	30.00047684	-1.99952316
5231	5471	20	33.05573654	13.05573654
6908	7169	28	31.17545128	3.175451279
5406	5600	34	33.56867981	-0.43132019
5137	5189	26	28.6977253	2.697725296
5559	5588	38	31.61421394	-6.38578606
5750	5813	34	33.73369217	-0.26630783
5481	5491	20	30.62488365	10.62488365
5588	5620	38	31.90377808	-6.09622192
6598	6634	32	29.39261818	-2.60738182
4529	4614	24	25.21554184	1.21554184
5859	5876	34	33.36116409	-0.63883591
5486	5505	20	30.83816147	10.83816147
6710	6743	32	29.03136826	-2.96863174
4693	4752	22	25.49590683	3.49590683
5724	5754	38	32.95229721	-5.04770279
7365	7389	28	30.11251259	2.112512589
5565	5591	20	31.60440063	11.60440063
5508	5528	20	31.03326416	11.03326416
6665	6707	32	29.17449188	-2.82550812
5315	5354	26	29.85651207	3.85651207
5992	5995	32	33.47574997	1.475749969
4466	4504	20	24.43460655	4.434606552
6125	6171	32	33.18063354	1.180633545
6091	6096	32	33.19664764	1.196647644

7304	7334	28	29.92111588	1.921115875
4165	4302	24	24.9362278	0.936227798
4894	4940	38	26.66124725	-11.3387527
7586	7629	30	31.33554268	1.335542679
7377	7421	30	30.42552376	0.425523758
9005	9021	36	32.90516663	-3.09483337
4621	4651	26	24.76717567	-1.23282433
6192	6234	32	32.62818909	0.628189087
4356	4393	26	24.1443634	-1.8556366
4440	4777	26	28.72738647	2.727386475
9251	9306	30	32.873909	2.873908997
4798	4851	38	26.03358459	-11.9664154
5429	5443	20	30.28627968	10.28627968
8373	8444	36	35.08149338	-0.91850662
2880	2949	22	22.5182724	0.5182724
4879	4985	38	27.69308662	-10.3069134
6732	6753	28	28.89159966	0.891599655
4625	4646	24	24.6486454	0.648645401
6275	6328	34	32.0418396	-1.9581604
5638	5655	38	32.01457214	-5.98542786
8771	8837	30	34.11087799	4.110877991
8383	8424	36	34.65398026	-1.34601974
5804	5961	34	35.12688065	1.126880646
6099	6126	34	33.26875687	-0.73124313
4497	4521	26	24.33449364	-1.66550636
2138	2165	22	23.00166702	1.001667023
4309	4399	22	24.70086288	2.700862885
5264	5266	20	28.74282837	8.742828369
8690	8744	36	34.13275528	-1.86724472
2596	2700	22	22.87787819	0.877878189
4306	4352	26	24.13286018	-1.86713982
3968	4028	22	23.45847893	1.458478928
5270	5315	26	29.61478424	3.614784241
6053	6098	34	33.74174881	-0.25825119
7107	7552	36	34.44647217	-1.55352783
5765	5819	38	33.64635468	-4.35364532
7303	7358	30	30.24172783	0.241727829
6779	6836	28	29.15908051	1.159080505
6620	6668	28	29.29300499	1.29300499
5635	5683	38	32.58755875	-5.41244125
4760	4870	38	26.82533455	-11.1746655
8277	8308	36	34.23123932	-1.76876068
5208	5215	20	28.39605713	8.396057129
5566	5629	38	32.32489777	-5.67510223
4997	5095	38	28.47316742	-9.52683258

5409	5423	20	30.12642479	10.12642479
4469	4526	24	24.68418312	0.684183121
4712	4743	26	25.15392876	-0.84607124
5805	5929	34	34.68335724	0.683357239
5202	5230	26	28.75130844	2.751308441
3104	3184	22	22.542696	0.542695999
6308	6355	32	31.74498749	-0.25501251
6062	6098	34	33.61555862	-0.38444138
4686	4712	26	24.97278214	-1.02721786
4506	4607	24	25.36135292	1.361352921
2319	2354	22	22.68478394	0.684783936
4396	4432	26	24.23254013	-1.76745987
6362	6402	32	31.27654648	-0.72345352
8508	8547	36	34.34333801	-1.65666199
5394	5452	38	30.85383224	-7.14616776
5424	5424	20	29.9767189	9.976718903
5532	5552	20	31.22509384	11.22509384
5094	5124	20	27.93598557	7.935985565
4924	4981	26	27.10997009	1.109970093
6685	6720	28	29.08332825	1.083328247
8872	8958	36	34.15156555	-1.84843445
4159	4222	22	23.97853851	1.978538513
8434	8506	36	34.95656967	-1.04343033
8959	8995	36	33.27943802	-2.72056198
5156	5391	34	32.35998535	-1.64001465
5848	5980	34	34.88962936	0.889629364
4165	4291	24	24.79611778	0.796117783
4647	4651	24	24.48376656	0.483766556
5553	5560	20	31.14260674	11.14260674
8085	8162	36	33.98134232	-2.01865768
6586	6885	28	31.64099884	3.64099884
4575	4625	20	24.87896729	4.878967285
5158	5197	26	28.61444092	2.614440918
4726	4765	20	25.33101082	5.331010818
7655	7698	30	31.64027405	1.640274048
4156	4283	24	24.78614998	0.786149979
8548	8568	36	33.99618149	-2.00381851
2072	2110	22	23.22439194	1.224391937
4886	5221	34	32.14028168	-1.85971832
6953	7017	28	28.98957825	0.989578247
6117	6163	32	33.24365997	1.243659973
7174	7215	28	29.49000168	1.490001678
4611	4698	38	25.58051109	-12.4194889
6912	6948	28	28.7875042	0.787504196
8226	8276	36	34.25302505	-1.74697495

8497	8589	30	35.08349228	5.083492279
4401	4460	24	24.53810692	0.538106918
5424	5426	20	30.01523209	10.01523209
7173	7219	30	29.55058861	-0.44941139
6085	6097	34	33.28691864	-0.71308136
6188	6212	32	32.54913712	0.549137115
5661	5679	38	32.21766663	-5.78233337
8997	9009	36	32.86935043	-3.13064957
4443	4491	26	24.50395584	-1.49604416
5989	6050	34	34.25244141	0.252441406
4083	4146	26	23.78680992	-2.21319008
8856	8930	30	34.02594757	4.025947571
6435	6487	28	30.77511597	2.775115967
4631	4698	24	25.36250496	1.362504959
4944	4971	38	26.69280243	-11.3071976
4264	4301	26	23.91226959	-2.08773041
6407	6434	28	30.84214783	2.842147827
4067	4326	24	26.24292374	2.242923737
2517	2591	22	22.69162941	0.69162941
5281	5315	20	29.49080467	9.490804672
5049	5097	38	27.92543983	-10.0745602
4227	4305	22	24.34115028	2.341150284
2409	2458	22	22.62007904	0.620079041
6469	6525	32	30.53181839	-1.46818161
7292	7305	28	29.64710426	1.647104263
4509	4568	20	24.81056786	4.810567856
5003	5047	38	27.48513794	-10.5148621
5353	5389	26	30.10247421	4.102474213
6223	6271	34	32.42081451	-1.57918549
7650	7718	30	31.94321632	1.943216324
5969	6059	34	34.59854507	0.598545074
3664	3734	22	22.8283596	0.828359604
7216	7240	28	29.45447159	1.454471588
7242	7595	30	33.84659576	3.846595764
5213	5250	26	29.01083374	3.01083374
5461	5510	38	31.21604538	-6.78395462
5353	5378	20	29.8906498	9.890649796
8314	8356	36	34.53765488	-1.46234512
6770	6827	32	29.17116928	-2.82883072
8698	8766	30	34.30351639	4.303516388
7247	7615	36	34.063694	-1.936306
5861	5893	34	33.56837082	-0.43162918
6930	6981	28	28.90108299	0.901082993
4617	4668	24	25.06553459	1.065534592
8148	8255	36	34.64959717	-1.35040283

8132	8204	30	34.12390137	4.123901367
4688	4691	24	24.63627815	0.636278152
6065	6117	32	33.69020844	1.690208435
8335	8382	36	34.69540787	-1.30459213
4651	4686	26	24.96466827	-1.03533173
9118	9169	30	33.12104034	3.121040344
7279	7292	28	29.58969498	1.589694977
4038	4116	22	23.86434174	1.864341736
7648	7928	36	34.69057083	-1.30942917
4609	4690	22	25.4824295	3.482429504
5712	5759	38	33.18375015	-4.81624985
5250	5542	34	34.20896149	0.208961487
3879	3909	22	22.85183907	0.851839066
5055	5092	20	27.76194191	7.76194191
4787	4828	26	25.71610451	-0.28389549
5817	5860	34	33.61649704	-0.38350296
4623	4657	24	24.83529091	0.835290909
4872	4922	26	26.56336784	0.563367844
9030	9100	30	33.57712173	3.577121735
6594	6609	28	29.29513359	1.295133591
6881	6929	28	28.9393692	0.939369202
5505	5559	38	31.66401863	-6.33598137
6490	6557	28	30.43393707	2.433937073
4827	4870	26	26.07194138	0.071941376
6196	6226	34	32.52296448	-1.47703552
5290	5379	38	30.61953163	-7.38046837
3572	3660	22	22.86317253	0.863172531
5125	5157	26	28.2193737	2.219373703
4388	4461	24	24.6836319	0.683631897
8432	8494	30	34.82616425	4.826164246
5556	5628	38	32.41827774	-5.58172226
8618	8687	36	34.4985466	-1.5014534
5585	5793	34	35.2468605	1.246860504
8587	8587	36	33.63779831	-2.36220169
5008	5259	20	31.49390793	11.49390793
5249	5271	26	29.00776291	3.007762909
4819	4874	22	26.23862267	4.238622665
6561	6617	28	29.80698586	1.806985855
4770	4806	20	25.48527336	5.485273361
4544	4593	26	24.77149391	-1.22850609
9189	9229	30	32.81149292	2.81149292
4147	4206	26	23.8973217	-2.1026783
7108	7171	30	29.48454285	-0.51545715
4769	4796	26	25.3268528	-0.6731472
8425	8516	36	35.23337936	-0.76662064

4971	5000	38	26.94457436	-11.0554256
3513	3569	22	22.46473122	0.464731216
6140	6184	32	33.05016708	1.050167084
4754	4815	22	25.83782005	3.837820053
7335	7364	28	30.04502487	2.045024872
5467	5548	38	31.88022423	-6.11977577
8524	8611	36	34.95475388	-1.04524612
5022	5077	26	27.84624672	1.846246719
8357	8396	36	34.68598557	-1.31401443
4811	4845	20	25.77231789	5.772317886
8166	8222	36	34.06604767	-1.93395233
5463	5480	20	30.61581039	10.61581039
6234	6235	32	32.04543304	0.045433044
5660	5837	34	35.0682373	1.068237305
4689	4720	20	25.05996323	5.059963226
7845	7912	30	32.79140472	2.791404724
6667	6703	28	29.11669922	1.116699219
3809	3876	22	23.14651489	1.146514893
4594	4622	26	24.63082123	-1.36917877
4656	4927	20	29.08812141	9.088121414
7946	8081	36	34.12151337	-1.87848663
5516	5557	38	31.50160408	-6.49839592
4466	4466	20	23.95059776	3.950597763
7307	7337	28	29.93436623	1.934366226
4581	4619	24	24.72583961	0.725839615
4312	4394	24	24.60653305	0.606533051
4938	4962	20	26.58785629	6.587856293
4510	4576	24	24.90225029	0.90225029
6422	6509	32	31.09254265	-0.90745735
5387	5461	38	31.10599136	-6.89400864
5229	5560	34	34.79212952	0.792129517
7242	7278	28	29.72530746	1.725307465
4510	4544	26	24.49466324	-1.50533676
6745	6761	32	28.82820702	-3.17179298
6566	6598	32	29.62016487	-2.37983513
4660	4669	24	24.61180496	0.611804962
8448	8669	36	36.9354248	0.935424805
8399	8435	36	34.55020142	-1.44979858
3914	3964	22	23.19487762	1.194877625
5163	5187	20	28.36633682	8.366336823
7232	7290	30	29.96716499	-0.03283501
7967	8140	36	34.70829391	-1.29170609
3193	3274	22	22.54989433	0.549894333
7020	7063	28	28.835886	0.835886002
3021	3095	22	22.51829147	0.518291473

4823	5128	26	31.06573486	5.065734863
6059	6137	32	33.89719391	1.897193909
6262	6300	32	32.05211639	0.052116394
4704	4733	24	25.09127426	1.091274261
5622	5639	38	31.88669014	-6.11330986
7723	7729	30	31.45955086	1.459550858
5937	6031	34	34.57950592	0.57950592
5760	5776	38	32.97045135	-5.02954865
6412	6459	32	30.9256134	-1.0743866
2267	2313	22	22.83460236	0.834602356
4979	5019	26	27.21873665	1.218736649
5419	5421	26	29.97527122	3.975271225
8685	8860	36	35.7768898	-0.2231102
5389	5420	26	30.29393578	4.293935776
5813	5908	32	34.30984879	2.309848785
4405	4509	22	25.12137222	3.121372223
7507	7559	30	31.10366249	1.103662491
6177	6216	32	32.72794342	0.72794342
2704	2788	22	22.68773842	0.687738419
8309	8314	36	34.03453827	-1.96546173
2791	2875	22	22.66313553	0.663135529
2223	2265	22	22.89633751	0.896337509
5357	5642	34	34.92940521	0.929405212
2109	2139	22	23.09533501	1.095335007
8576	8584	36	33.77071381	-2.22928619
3836	4149	22	26.34796524	4.34796524
5684	5716	38	32.6710968	-5.3289032
6256	6264	32	31.91510391	-0.08489609
4802	4841	26	25.79679108	-0.20320892
5080	5124	26	28.09377861	2.09377861
7106	7154	28	29.28069687	1.280696869
5426	5456	26	30.57041359	4.570413589
8569	8590	36	33.96202087	-2.03797913
7436	7480	30	30.68608856	0.686088562
8005	8095	30	33.79704285	3.797042847
7156	7201	28	29.46250916	1.462509155
4877	4924	22	26.54550743	4.545507431
4652	4667	24	24.66903877	0.669038773
5615	5745	34	34.00676346	0.006763458
5264	5280	20	29.01128006	9.01128006
5380	5408	20	30.16422844	10.16422844
4835	5127	34	30.91161919	-3.08838081
6890	6910	28	28.67011452	0.670114517
4533	4610	24	25.1119976	1.111997604
8262	8330	36	34.6460228	-1.3539772

5877	5877	34	33.17260742	-0.82739258
5191	5283	38	29.89156532	-8.10843468
4514	4604	22	25.22919083	3.229190826
7995	8272	36	36.18405151	0.184051514
5485	5504	38	30.83016968	-7.16983032
8600	8684	30	34.74180603	4.74180603
5489	5494	20	30.59254646	10.59254646
4467	4521	24	24.64092255	0.640922546
6511	6564	32	30.18248749	-1.81751251
6382	6406	28	31.02068138	3.020681381
4168	4499	26	27.44106865	1.441068649
8233	8293	30	34.41394424	4.413944244
7265	7307	28	29.90489197	1.904891968
5189	5213	26	28.57185173	2.57185173
6037	6083	34	33.87395096	-0.12604904
6637	6664	32	29.07434845	-2.92565155
4619	4621	24	24.36205673	0.362056732
5564	5789	34	35.40940094	1.40940094
7593	7946	36	35.39674377	-0.60325623
5638	5703	38	32.93889999	-5.06110001
3914	4146	24	25.51303673	1.513036728
4303	4405	24	24.83857155	0.838571548
7591	7960	36	35.59592056	-0.40407944
6165	6187	32	32.71805573	0.718055725



## Appendix C

This appendix contains the Matlab script to monitor in-process sensor information.

```
clear all
clc
s = serial('COM3'); %define port
set(s,'BaudRate',9600); %banudrate
fopen(s); %open ports
fid=fopen('serial_data.txt','w+'); % open/create a txt named'serial_data'
interval = 10000;
passo = 1;
t = 1;
x = 0;
while(t<interval)
    b = str2num(fgetl(s)); %use fget(s) Function read searil data from buffer
    fid2=fopen('sensor_data.txt','w+'); % open/create a txt named'sensor_data', this text will be overright
with change of time
    fprintf(fid,'%d ',b);
    fprintf(fid2,'%d ',b);
    fprintf(fid,'\n');
    fprintf('%d ',b);
    fprintf('\n');
    x = [x,b];
    plot(x);
    grid
    t = t+passo;
    drawnow;
    fclose(fid2); %close 'sensor_data' before time
end
fclose(fid); % close txt
fclose(s);
```

## Appendix D

This appendix contains the MATLAB script to enable communication between a 3D printer, loadcell sensor, artificial neural network (ANN) model, and computer through RS-232 standard serial port.

```
clear all
clc
%%%%%%%%%%%%%%%%%%%%%%%%%%%%%%%%%%%%%%%%%%%%%%%%%%%%%%%%%%%%%%%%%%%%%%%%%%%%%%initialize
Normalization%%%%%%%%%%%%%%%%%%%%%%%%%%%%%%%%%%%%%%%%%%%%%%%%%%%%%%%%%%%%%%%%%%%%%%%%
A=xlsread('zhaolongdata9.9.csv'); % this function is based on data sheet 'zhaolongdata9.9.csv')
Pressure1_mean=mean(A(:,1));
Pressure2_mean=mean(A(:,2));
Extrusion_mean=mean(A(:,3));
Pressure1_std=std(A(:,1));
Pressure2_std=std(A(:,2));
Extrusion_std=std(A(:,3));
%%%%%%%%%%%%%%%%%%%%%%%%%%%%%%%%%%%%%%%%%%%%%%%%%%%%%%%%%%%%%%%%%%%%%%%%Open port for control printer%%%%%%%%%%%%%%%%%%%%%%%%%%%%%%%%%%%%%%%%%%%%%%%%%%%%%%%%%%%%%%%%%%%%%%%%
arduino=serialport('COM4',250000); % create serial communication object on port COM4
configureTerminator(arduino,"CR/LF") %arduino.Terminator = {10, 13};
flush(arduino);
%%%%%%%%%%%%%%%%%%%%%%%%%%%%%%%%%%%%%%%%%%%%%%%%%%%%%%%%%%%%%%%%%%%%%%%%Load machine learning
Model%%%%%%%%%%%%%%%%%%%%%%%%%%%%%%%%%%%%%%%%%%%%%%%%%%%%%%%%%%%%%%%%%%%%%%%%
%This program is now running Rule Predict good set 1
%%%%%%%%%%%%%%%%%%%%%%%%%%%%%%%%%%%%%%%%%%%%%%%%%%%%%%%%%%%%%%%%%%%%%%%%
%%%%%%%%%%%%%%%%%%%%%%%%%%%%%%%%%%%%%%%%%%%%%%%%%%%%%%%%%%%%%%%%%%%%%%%%
%%%%%%%%%%%%%%%%%%%%%%%%%%%%%%%%%%%%%%%%%%%%%%%%%%%%%%%%%%%%%%%%%%%%%%%%
net = importKerasNetwork('model.h5'); % Load Pretrained machine learning model
out=4500; % This value should be overwrite by sensor
target_pressure=7000; % This value should be defined by width & Pressure relation
target_extrusion= 34; % This value doesnot matter in this research, but it can be used to predict
pressures
%%%%%%%%%%%%%%%%%%%%%%%%%%%%%%%%%%%%%%%%%%%%%%%%%%%%%%%%%%%%%%%%%%%%%%%%This part is doing perparing for storage data%%%%%%%%%%%%%%%%%%%%%%%%%%%%%%%%%%%%%%%%%%%%%%%%%%%%%%%%%%%%%%%%%%%%%%%%
frecord = fopen('testrecord.txt','w+');
fpn = fopen ('14test.txt', 'rt'); %open the file
X=[0,0]; %To store X
Y=[0,0]; %To store Y
E=[0,0]; %To store E

while feof(fpn) ~= 1 %find the value of pointer P, return 1 if it is the end of
the file, otherwise return 0
    file = fgetl(fpn); %get the first line of the file.
    skipmark=0; %skipmark for delay
    commentcounter=0;
    gohome=0;
    repidcounter=0; %Repid motion counter
    presuresensor=0; %Pressure signal simulation rest
    S=regexp(file,'\s+', 'split'); %split and save this line of code into a cell S;
    [A,B]=size(S); %Get the size of Cell:A*B
    str1=cell2mat(S(1,1)); %If it is repid motion
    str2='GO';
    str3='!';
```

```

str4='G28';
tf1 = strcmp(str1,str2);
tf2 = strcmp(str1,str3);
tf3 = strcmp(str1,str4);
if tf1==1
    repidcounter=1;           %then set a counter to 1
end
if tf2==1
    commentcounter=1;
end
if tf3==1
    gohome=1;
end
for i=1:B                    %Form first unit of the cell to the last unit of the cell
    if cell2mat(S(1,i))=='X' %Read X data;
        xnumber= cell2mat(S(1,i+1));
        X(1,2)= str2double(xnumber);
    elseif cell2mat(S(1,i))=='Y' %Read Y data;
        ynumber= cell2mat(S(1,i+1));
        Y(1,2)= str2double(ynumber);
    elseif cell2mat(S(1,i))=='E' %If the ith cell is "E"(to specify extrusion)
        skipmark=1;           %skipmark for delay
        munber= cell2mat(S(1,i+1)); %Then the number of the next cell(i+1) should be the
one which stores extruding rate
        munberr= str2double(munber); % convert this unite from string to double
%%%%%%%%%%%%%%%%%%%%%%%%%%%%%%%%%%%%%%%%%%%%%%%%%%%%%%%%%%%%%%%%%%%%%%%%
%%%%%%%%%%%%%%%%%%%%%%%%%%%%%%%%%%%%%%%%%%%%%%%%%%%%%%%%%%%%%%%%%%%%%%%%
%%%%%%%%%%%%%%%%%%%%%%%%%%%%%%%%%%%%%%%%%%%%%%%%%%%%%%%%%%%%%%%%%%%%%%%%
        if munberr>5          %%% if Extrusion is not 0
            %%%Read Pressure from
            Text%%%%%%%%%%%%%%%%%%%%%%%%%%%%%%%%%%%%%%%%%%%%%%%%%%%%%%%%%%%%%%%%%%%%%%%%
            fileID = fopen('sensor_data.txt','r');
            formatSpec = '%f';
            out = fscanf(fileID,formatSpec);
            %%%Then use the sensordata do nomalization and
            prediction%%%%%%%%%%%%%%%%%%%%%%%%%%%%%%%%%%%%%%%%%%%%%%%%%%%%%%%%%%%%%%%%%%%%%%%%
            Predict=3; % Predict pressure1=1;Predict pressure2=2;Predict Extrusion=3; Else=0
            Pressure1=(out-Pressure1_mean)/Pressure1_std; % Normalize Pressure1
            Pressure2=(target_pressure-Pressure2_mean)/Pressure2_std; % Normalize Pressure2
            Extrusion=(target_extrusion-Extrusion_mean)/Extrusion_std; % Normalize Extrusion
            x_predic_pressure1 = [Pressure2,Extrusion]; % Inputs for Normalized Pressure1
prediction
            x_predic_pressure2 = [Pressure1,Extrusion]; % Inputs for Normalized Pressure2
prediction
            x_predic_extrusion = [Pressure1,Pressure2]; % Inputs for Normalized Extrusion
prediction
            %%%%%%%%%%%%%%%%%%%%%%%%%%%%%%%%%%%%%%%%%%%%%%%%%%%%%%%%%%%%%%%%%%%%%%%%%this part tells what to
            predict%%%%%%%%%%%%%%%%%%%%%%%%%%%%%%%%%%%%%%%%%%%%%%%%%%%%%%%%%%%%%%%%%%%%%%%%
            if Predict==1
                x=x_predic_pressure1;
            elseif Predict==2
                x=x_predic_pressure2;

```

```

elseif Predict==3
    x=x_predic_extrusion;
else
    x=0;
end
prediction=net.predict(x);    %Actual Output for prediction
munberrr=prediction;          %%% This part is used for calculation!
S{1,i+1}= num2str(munberrr);    %%% Convert the extrsion rate back string and save
to the cell
%%%%%%%%%%%%%%%%%%%%%%%%%%%%%%%%%%%%%%%%%%%%%%%%%%%%%%%%%%%%%%%%%%%%%%%%
%%%%%%%%%%%%%%%%%%%%%%%%%%%%%%%%%%%%%%%%%%%%%%%%%%%%%%%%%%%%%%%%%%%%%%%%
%%%%%%%%%%%%%%%%%%%%%%%%%%%%%%%%%%%%%%%%%%%%%%%%%%%%%%%%%%%%%%%%%%%%%%%%
end
end
ADC=strjoin(S);
if commentcounter==0
if gohome==1
fprintf('%s ',ADC);                %print the string S into new file
fprintf(frecord,'%s',ADC);
writeline(arduino,ADC);           %print the string S into gcode interpreter
fprintf('\n');
fprintf(frecord,'\n');
n = read_ok(arduino, false);
elseif repidcounter==1
    fprintf(frecord,'%s ',ADC);        %Write the string S into new file
    fprintf(frecord,'\n');
    fprintf('%s ',ADC);                %print the string S into new file
    writeline(arduino,ADC);           %print the string S into new file
    fprintf('\n');
    n = read_ok(arduino, true);
    fileID = fopen('sensor_data.txt','r');
    formatSpec = '%f';
    out = fscanf(fileID,formatSpec);
while out<target_pressure*0.9      %pressure calculation
    Resete='G92 E0.0000';             %Reset Extrusion back to 0
    fprintf(frecord,'%s ',Resete);    %Write the string S into new file
    fprintf(frecord,'\n');
    fprintf('%s ',Resete);            %print the string S into new file
    writeline(arduino,Resete);        %print the string S into gcode interpreter
    fprintf('\n');
    n = read_ok(arduino, true);
    BDC='G1 E30 F1200';
    fprintf(frecord,'%s ',BDC);        %Write the string S into new file
    fprintf(frecord,'\n');
    fprintf('%s ',BDC);                %print the string S into new file
    writeline(arduino,BDC);           %print the string S into gcode interpreter
    fprintf('\n');
    n = read_ok(arduino, true);
    fileID = fopen('sensor_data.txt','r');
    formatSpec = '%f';
    out = fscanf(fileID,formatSpec);
end
elseif skipmark==1

```

```

fprintf('X is %d ',X(:));           %print the string S into new file
fprintf('\n');
fprintf('Y is %d ',Y(:));           %print the string S into new file
fprintf('\n');
fprintf(frecord,'%s ',ADC);         %Write the string S into new file
fprintf(frecord,'\n');
fprintf('%s ',ADC);                 %print the string S into new file
writeline(arduino,ADC);             %print the string S into gcode interpreter
fprintf('\n');
n = read_ok(arduino, true);
fprintf(frecord,'X is %d ',X(:));   %print the string S into new file
fprintf(frecord,'\n');
fprintf(frecord,'Y is %d ',Y(:));   %print the string S into new file
fprintf(frecord,'\n');
X(1,1)=X(1,2);
Y(1,1)=Y(1,2);
else
fprintf(frecord,'%s ',ADC);         %Write the string S into new file
fprintf(frecord,'\n');
fprintf('%s ',ADC);                 %print the string S into new file
writeline(arduino,ADC);             %print the string S into gcode interpreter
fprintf('\n');
n = read_ok(arduino, true);

end
end
end
fclose(frecord);
clear arduino;

```

## Appendix E

This appendix is an example of the original executive G-code. In this example  $M_{Extrude} =$

### 1.3.

```
G90
M82
M106 S0
M140 S0
M104 S0 T0
G28
G92 E0.000
G1 Z-28 F3000
G1 E300 F1000
T0
G1 Z-32.5 F1800
G1 Y-80 F3900
G92 E0.0000
G1 Y-0 F3600
G0 X-150 Y-70 E 240 F 1800
G92 E0
G1 X -150 Y -20 F1200
G92 E0.0000
G1 X -130 Y -20 E 26
G92 E0.0000
G1 X -130 Y -18
G92 E0.0000
G1 X -150 Y -18 E 26
G92 E0.0000
G1 X -150 Y -16
G92 E0.0000
G1 X -130 Y -16 E 26
G92 E0.0000
G1 X -130 Y -14
G92 E0.0000
G1 X -150 Y -14 E 26
G92 E0.0000
G1 X -150 Y -12
G92 E0.0000
G1 X -130 Y -12 E 26
G92 E0.0000
G1 X -130 Y -10
G92 E0.0000
G1 X -150 Y -10 E 26
G92 E0.0000
G1 X -150 Y -8
G92 E0.0000
G1 X -130 Y -8 E 26
G92 E0.0000
G1 X -130 Y -6
G92 E0.0000
G1 X -150 Y -6 E 26
G92 E0.0000
G1 X -150 Y -4
```

```

G92 E0.0000
G1 X -130 Y -4 E 26
G92 E0.0000
G1 X -130 Y -2
G92 E0.0000
G1 X -150 Y -2 E 26
G92 E0.0000
G1 X -150 Y 0
G92 E0.0000
G1 X -130 Y 0 E 26
G92 E0.0000
G1 X -130 Y 2
G92 E0.0000
;factor 1.3
G92 E0.0000
G1 X -120 Y -20 F1200
G92 E0.0000
G1 X -100 Y -20 E 26
G92 E0.0000
G1 X -100 Y -18
G92 E0.0000
G1 X -120 Y -18 E 26
G92 E0.0000
G1 X -120 Y -16
G92 E0.0000
G1 X -100 Y -16 E 26
G92 E0.0000
G1 X -100 Y -14
G92 E0.0000
G1 X -120 Y -14 E 26
G92 E0.0000
G1 X -120 Y -12
G92 E0.0000
G1 X -100 Y -12 E 26
G92 E0.0000
G1 X -100 Y -10
G92 E0.0000
G1 X -120 Y -10 E 26
G92 E0.0000
G1 X -120 Y -8
G92 E0.0000
G1 X -100 Y -8 E 26
G92 E0.0000
G1 X -100 Y -6
G92 E0.0000
G1 X -120 Y -6 E 26
G92 E0.0000
G1 X -120 Y -4
G92 E0.0000
G1 X -100 Y -4 E 26
G92 E0.0000
G1 X -100 Y -2
G92 E0.0000
G1 X -120 Y -2 E 26

```

```

G92 E0.0000
G1 X -120 Y 0
G92 E0.0000
G1 X -100 Y 0 E 26
G92 E0.0000
G1 X -100 Y 2
G92 E0.0000
;factor 1.3
G92 E0.0000
G1 X -90 Y -20 F1200
G92 E0.0000
G1 X -70 Y -20 E 26
G92 E0.0000
G1 X -70 Y -18
G92 E0.0000
G1 X -90 Y -18 E 26
G92 E0.0000
G1 X -90 Y -16
G92 E0.0000
G1 X -70 Y -16 E 26
G92 E0.0000
G1 X -70 Y -14
G92 E0.0000
G1 X -90 Y -14 E 26
G92 E0.0000
G1 X -90 Y -12
G92 E0.0000
G1 X -70 Y -12 E 26
G92 E0.0000
G1 X -70 Y -10
G92 E0.0000
G1 X -90 Y -10 E 26
G92 E0.0000
G1 X -90 Y -8
G92 E0.0000
G1 X -70 Y -8 E 26
G92 E0.0000
G1 X -70 Y -6
G92 E0.0000
G1 X -90 Y -6 E 26
G92 E0.0000
G1 X -90 Y -4
G92 E0.0000
G1 X -70 Y -4 E 26
G92 E0.0000
G1 X -70 Y -2
G92 E0.0000
G1 X -90 Y -2 E 26
G92 E0.0000
G1 X -90 Y 0
G92 E0.0000
G1 X -70 Y 0 E 26
G92 E0.0000
G1 X -70 Y 2

```



```

G92 E0.0000
;factor 1.3
G92 E0.0000
G1 X -60 Y -20 F1200
G92 E0.0000
G1 X -40 Y -20 E 26
G92 E0.0000
G1 X -40 Y -18
G92 E0.0000
G1 X -60 Y -18 E 26
G92 E0.0000
G1 X -60 Y -16
G92 E0.0000
G1 X -40 Y -16 E 26
G92 E0.0000
G1 X -40 Y -14
G92 E0.0000
G1 X -60 Y -14 E 26
G92 E0.0000
G1 X -60 Y -12
G92 E0.0000
G1 X -40 Y -12 E 26
G92 E0.0000
G1 X -40 Y -10
G92 E0.0000
G1 X -60 Y -10 E 26
G92 E0.0000
G1 X -60 Y -8
G92 E0.0000
G1 X -40 Y -8 E 26
G92 E0.0000
G1 X -40 Y -6
G92 E0.0000
G1 X -60 Y -6 E 26
G92 E0.0000
G1 X -60 Y -4
G92 E0.0000
G1 X -40 Y -4 E 26
G92 E0.0000
G1 X -40 Y -2
G92 E0.0000
G1 X -60 Y -2 E 26
G92 E0.0000
G1 X -60 Y 0
G92 E0.0000
G1 X -40 Y 0 E 26
G92 E0.0000
G1 X -40 Y 2
G92 E0.0000
;factor 1.3
G92 E0.0000
G1 X -30 Y -20 F1200
G92 E0.0000
G1 X -10 Y -20 E 26

```

```

G92 E0.0000
G1 X -10 Y -18
G92 E0.0000
G1 X -30 Y -18 E 26
G92 E0.0000
G1 X -30 Y -16
G92 E0.0000
G1 X -10 Y -16 E 26
G92 E0.0000
G1 X -10 Y -14
G92 E0.0000
G1 X -30 Y -14 E 26
G92 E0.0000
G1 X -30 Y -12
G92 E0.0000
G1 X -10 Y -12 E 26
G92 E0.0000
G1 X -10 Y -10
G92 E0.0000
G1 X -30 Y -10 E 26
G92 E0.0000
G1 X -30 Y -8
G92 E0.0000
G1 X -10 Y -8 E 26
G92 E0.0000
G1 X -10 Y -6
G92 E0.0000
G1 X -30 Y -6 E 26
G92 E0.0000
G1 X -30 Y -4
G92 E0.0000
G1 X -10 Y -4 E 26
G92 E0.0000
G1 X -10 Y -2
G92 E0.0000
G1 X -30 Y -2 E 26
G92 E0.0000
G1 X -30 Y 0
G92 E0.0000
G1 X -10 Y 0 E 26
G92 E0.0000
G1 X -10 Y 2
G92 E0.0000
;factor 1.3
G92 E0.0000
G1 X 0 Y -20 F1200
G92 E0.0000
G1 X 20 Y -20 E 26
G92 E0.0000
G1 X 20 Y -18
G92 E0.0000
G1 X 0 Y -18 E 26
G92 E0.0000
G1 X 0 Y -16

```

```

G92 E0.0000
G1 X 20 Y -16 E 26
G92 E0.0000
G1 X 20 Y -14
G92 E0.0000
G1 X 0 Y -14 E 26
G92 E0.0000
G1 X 0 Y -12
G92 E0.0000
G1 X 20 Y -12 E 26
G92 E0.0000
G1 X 20 Y -10
G92 E0.0000
G1 X 0 Y -10 E 26
G92 E0.0000
G1 X 0 Y -8
G92 E0.0000
G1 X 20 Y -8 E 26
G92 E0.0000
G1 X 20 Y -6
G92 E0.0000
G1 X 0 Y -6 E 26
G92 E0.0000
G1 X 0 Y -4
G92 E0.0000
G1 X 20 Y -4 E 26
G92 E0.0000
G1 X 20 Y -2
G92 E0.0000
G1 X 0 Y -2 E 26
G92 E0.0000
G1 X 0 Y 0
G92 E0.0000
G1 X 20 Y 0 E 26
G92 E0.0000
G1 X 20 Y 2
G92 E0.0000
;factor 1.3
G92 E0.0000
G1 X 30 Y -20 F1200
G92 E0.0000
G1 X 50 Y -20 E 26
G92 E0.0000
G1 X 50 Y -18
G92 E0.0000
G1 X 30 Y -18 E 26
G92 E0.0000
G1 X 30 Y -16
G92 E0.0000
G1 X 50 Y -16 E 26
G92 E0.0000
G1 X 50 Y -14
G92 E0.0000
G1 X 30 Y -14 E 26

```

```

G92 E0.0000
G1 X 30 Y -12
G92 E0.0000
G1 X 50 Y -12 E 26
G92 E0.0000
G1 X 50 Y -10
G92 E0.0000
G1 X 30 Y -10 E 26
G92 E0.0000
G1 X 30 Y -8
G92 E0.0000
G1 X 50 Y -8 E 26
G92 E0.0000
G1 X 50 Y -6
G92 E0.0000
G1 X 30 Y -6 E 26
G92 E0.0000
G1 X 30 Y -4
G92 E0.0000
G1 X 50 Y -4 E 26
G92 E0.0000
G1 X 50 Y -2
G92 E0.0000
G1 X 30 Y -2 E 26
G92 E0.0000
G1 X 30 Y 0
G92 E0.0000
G1 X 50 Y 0 E 26
G92 E0.0000
G1 X 50 Y 2
G92 E0.0000
;factor 1.3
G92 E0.0000
G1 X 60 Y -20 F1200
G92 E0.0000
G1 X 80 Y -20 E 26
G92 E0.0000
G1 X 80 Y -18
G92 E0.0000
G1 X 60 Y -18 E 26
G92 E0.0000
G1 X 60 Y -16
G92 E0.0000
G1 X 80 Y -16 E 26
G92 E0.0000
G1 X 80 Y -14
G92 E0.0000
G1 X 60 Y -14 E 26
G92 E0.0000
G1 X 60 Y -12
G92 E0.0000
G1 X 80 Y -12 E 26
G92 E0.0000
G1 X 80 Y -10

```

```

G92 E0.0000
G1 X 60 Y -10 E 26
G92 E0.0000
G1 X 60 Y -8
G92 E0.0000
G1 X 80 Y -8 E 26
G92 E0.0000
G1 X 80 Y -6
G92 E0.0000
G1 X 60 Y -6 E 26
G92 E0.0000
G1 X 60 Y -4
G92 E0.0000
G1 X 80 Y -4 E 26
G92 E0.0000
G1 X 80 Y -2
G92 E0.0000
G1 X 60 Y -2 E 26
G92 E0.0000
G1 X 60 Y 0
G92 E0.0000
G1 X 80 Y 0 E 26
G92 E0.0000
G1 X 80 Y 2
G92 E0.0000
;factor 1.3
G92 E0.0000
G1 X 90 Y -20 F1200
G92 E0.0000
G1 X 110 Y -20 E 26
G92 E0.0000
G1 X 110 Y -18
G92 E0.0000
G1 X 90 Y -18 E 26
G92 E0.0000
G1 X 90 Y -16
G92 E0.0000
G1 X 110 Y -16 E 26
G92 E0.0000
G1 X 110 Y -14
G92 E0.0000
G1 X 90 Y -14 E 26
G92 E0.0000
G1 X 90 Y -12
G92 E0.0000
G1 X 110 Y -12 E 26
G92 E0.0000
G1 X 110 Y -10
G92 E0.0000
G1 X 90 Y -10 E 26
G92 E0.0000
G1 X 90 Y -8
G92 E0.0000
G1 X 110 Y -8 E 26

```

```
G92 E0.0000
G1 X 110 Y -6
G92 E0.0000
G1 X 90 Y -6 E 26
G92 E0.0000
G1 X 90 Y -4
G92 E0.0000
G1 X 110 Y -4 E 26
G92 E0.0000
G1 X 110 Y -2
G92 E0.0000
G1 X 90 Y -2 E 26
G92 E0.0000
G1 X 90 Y 0
G92 E0.0000
G1 X 110 Y 0 E 26
G92 E0.0000
G1 X 110 Y 2
G92 E0.0000
; layer end
G28 F1000
G1 E-100 F3000
```